ABSTRACT

Title of dissertation: Efficient Surface Conversion for Neutral Atom Detection

Patrick Hughes
Doctor of Philosophy, 2007

Dissertation directed by: Professor Michael Coplan
Department of Chemical Physics

Neutral atom detection is a useful way of studying astrophysical plasma structures such as the heliosphere and planetary magnetospheres. When plasma ions undergo charge exchange with the neutral background gas, energetic neutral atoms (ENAs) are generated. These neutral atoms travel in straight lines from the point of charge exchange because they are not subject to deflection by the electric and magnetic fields in space. As a result ENAs can be used to image the plasma structures from which they originate. ENAs in the energy range from a few eV to a few keV are particularly worth studying and are best detected by conversion to negative ions at a surface, a method that has been successfully used by ENA imagers on the Imager for Magnetosphere-to-Aurora Global Exploration (IMAGE) spacecraft. The function and construction of the imager is dependent upon the efficiency of the conversion surface used. A surface with a high conversion efficiency would allow the imager to be smaller and still collect a measurable signal compared to an imager using a surface with low conversion efficiency. The previously used conversion surface had an efficiency of about 1%.

In order to find a more efficient conversion surface, detailed as well as comparative measurements of conversion efficiencies were taken at two facilities. The surfaces studied are polished tungsten, highly ordered pyrolytic graphite, diamond-like carbon, a secondary electron emitting leaded glass, gold, silver and platinum. The work function and smoothness of some of the sample surfaces were measured. These measurements have been compared with measured conversion efficiencies to identify those surface properties that are critical for conversion efficiency. For many surfaces, adsorbates and roughness appear to play an important role in conversion efficiency.

Efficient Surface Conversion for Neutral Atom Detection

by

Patrick Phillip Hughes

Dissertation submitted to the Faculty of the Graduate School of the
University of Maryland, College Park in partial fulfillment
of the requirements for the degree of
Doctor of Philosophy
2007

Advisory Committee:
Professor Ellen Williams, Chair
Professor Michael Coplan, Advisor
Professor Michael Fuhrer
Dr. Keith Ogilvie
Professor Min Ouyang
Professor Janice Reutt-Robey

Dedication

To my mom and dad, and to my brothers.

Acknowledgments

I owe many thanks to everyone who helped make this thesis possible. It is the result of a lot of hard work put in by many different people throughout my graduate school years.

First, I would like to thank my advisor, Professor Michael Coplan, for allowing me to work on this project and always having good advice for every problem that arose. I cannot express my gratitude for being able to work with someone who displays such a tireless commitment and enthusiasm for his work. A tremendous amount of help was given to me from all of our colleagues at NASA Goddard Space Flight Center. Dr. Dennis Chornay, Dr. Michael Collier, Dr. John Keller, Dr. Keith Ogilvie and Dr. Mark Shappirio graciously shared their knowledge and expertise and helped this project along on every level.

I would like to acknowledge the members of my thesis committee, Professor Ellen Williams, Professor Michael Fuhrer, Professor Min Ouyang and Professor Janice Reutt-Robey for agreeing to review this thesis and sit through my defense.

The work done at the University of Denver would not have been possible without the assistance provided by Dr. Jeffery DeFazio for testing the surfaces and collecting the data for the detailed measurements. Closer to home, I wish to thank Edd Cole for the effort and precision in the machine shop that went into changing my design drawings into the real thing. I also would like to thank the various summer interns and other lab mates of mine, Evan Ulrich, Sanjeev Chauhan, Bill Zinacola, Ken Rossato, Matt Dantas-McCutcheon, Kaylan Orben and Jason Knebel.

I owe special thanks to my friends, Nick, Dan, Beth, Chad, Manolis, other Chad, Willie, Mike and everyone else. They made coming here for graduate school a unique experience that I will never forget, mostly around lunch and tea time.

Finally, I wish to thank my family for their unwavering love and support not only throughout graduate school, but my entire life.

The work done in this thesis was supported by NASA grant NNGO5GQ37G, the GAANN fellowship and the MRSEC group at UMCP.

Table of Contents

List of Tables

List of Figures

Chapter 1

Background

Energetic neutral atom (ENA) detection has recently emerged as a method for studying space plasmas. Energetic plasma structures in the presence of an ambient neutral particle background in space produce energetic neutral atoms through charge exchange interactions. After a plasma ion exchanges charge with a neutral background atom and becomes an energetic neutral atom, it is no longer affected by the magnetic and electric fields of the plasma. In space, ENAs can travel long distances without interaction with other particles, making them ideal for observing the interaction between plasma structures and the neutral background. ENAs are often grouped into three overlapping categories based on their kinetic energy, high (10 keV and above), medium (100 eV to 50 keV) and low (less than 500 eV), sometimes these groups are referred to as high, low and ultra low respectively [1].

1.1 Space Plasmas

1.1.1 Magnetospheres

The study of space plasmas is important for space exploration both near and far from Earth. Of current interest are the magnetospheres of planets and planetary satellites and the heliosphere. Planetary magnetospheres are the regions in space where charged particle motion is influenced by the magnetic field of the planet.

They are found around planets with strong magnetic fields, like the Earth, Jupiter and Saturn, but planets without a magnetic field, or one too weak to support a magnetosphere, can sometimes have magnetosphere-like features, such as the bow shock and magnetosheath around Venus [2].

Of the known magnetospheres, the one around Earth (Fig. 1.1) has been studied the most. Interactions between the magnetic field of the Earth and the solar wind shape the magnetosphere. Ionized particles from the atmosphere and from the solar wind populate the plasmas in the magnetosphere. The solar wind compresses the magnetic field of the Earth on the dayside of the planet, where it extends between 10 to 11 Earth Radii (R_E), and stretches it into the long magnetotail on the night side, more than 200 R_E in length from the center of the Earth. The magnetosphere deflects most of the incoming solar wind ions, shielding the atmosphere from direct bombardment. A bow shock is formed on the sunward side of the magnetosphere where the solar wind ions are slowed and deflected. This region of slowed solar wind is known as the magnetosheath. Inside the magnetosheath is the magnetopause, the boundary that most solar wind ions are unable to cross. There are two polar cusps, holes in the magnetopause that allow solar wind ions to penetrate deep into the atmosphere. Solar wind ions that leak through the magnetopause tend to first pool in the plasma sheet in the middle of the magnetotail. The plasma sheet has a weak magnetic field that allows the particles in it to leak out and populate the rest of the magnetosphere. The Plasmasphere is contained in the closed magnetic field lines that circle around the Earth and ends at a about 4.7 R_E from the center of the Earth. The radiation belts inside the plasmasphere are a result of energetic

particles that travel between the poles of the planet along the closed magnetic field lines. The charged particles slow down and can reverse direction as they move closer to the poles of the planet. It is possible for a single particle to make several trips between the poles as a part of the radiation belts. The ring current comes from the circulation of the radiation belts around the planet and can weaken the magnetic field measured at the surface of the Earth.

Interactions between the solar wind and the magnetosphere can have serious effects on wireless communications, spacecraft orbits and terrestrial power grids. Study of these plasma systems with ENAs is an effective way of imaging the plasma structures and observing their time evolution.

1.1.2 The Heliosphere

The heliosphere is the region in space filled with the expanding solar wind and permeated by the sun's magnetic field (Fig. 1.2). The exact size of the heliosphere is unknown, but it extends far beyond the solar system with the termination shock at about 100 astronomical units (AU) from the sun and the heliopause at about 150 AU. Inside the solar system, solar wind particles have directed speeds away from the sun between 300 and 600 km/s at Earth orbit, but they slow down as the distance from the sun increases until they reach the solar wind termination shock where the directed velocity of the particles becomes smaller than their random velocities. From the termination shock the solar wind continues to expand creating the heliosheath. The heliopause marks the outer edge of the heliosheath, where the solar wind meets

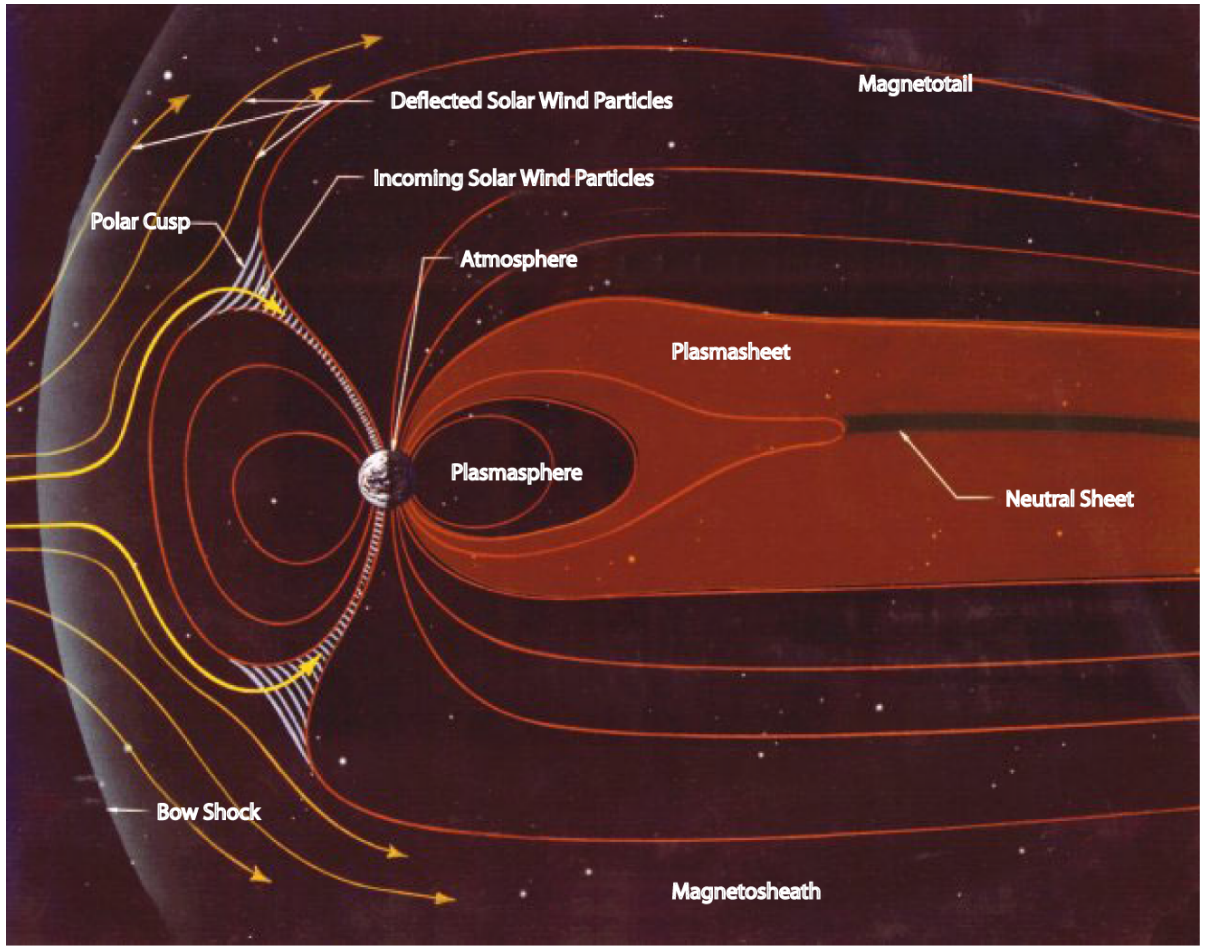

Figure 1.1: Diagram of the magnetosphere around the Earth. The basic shape of the magnetic field lines are shown and specific plasma structures are indicated [3].

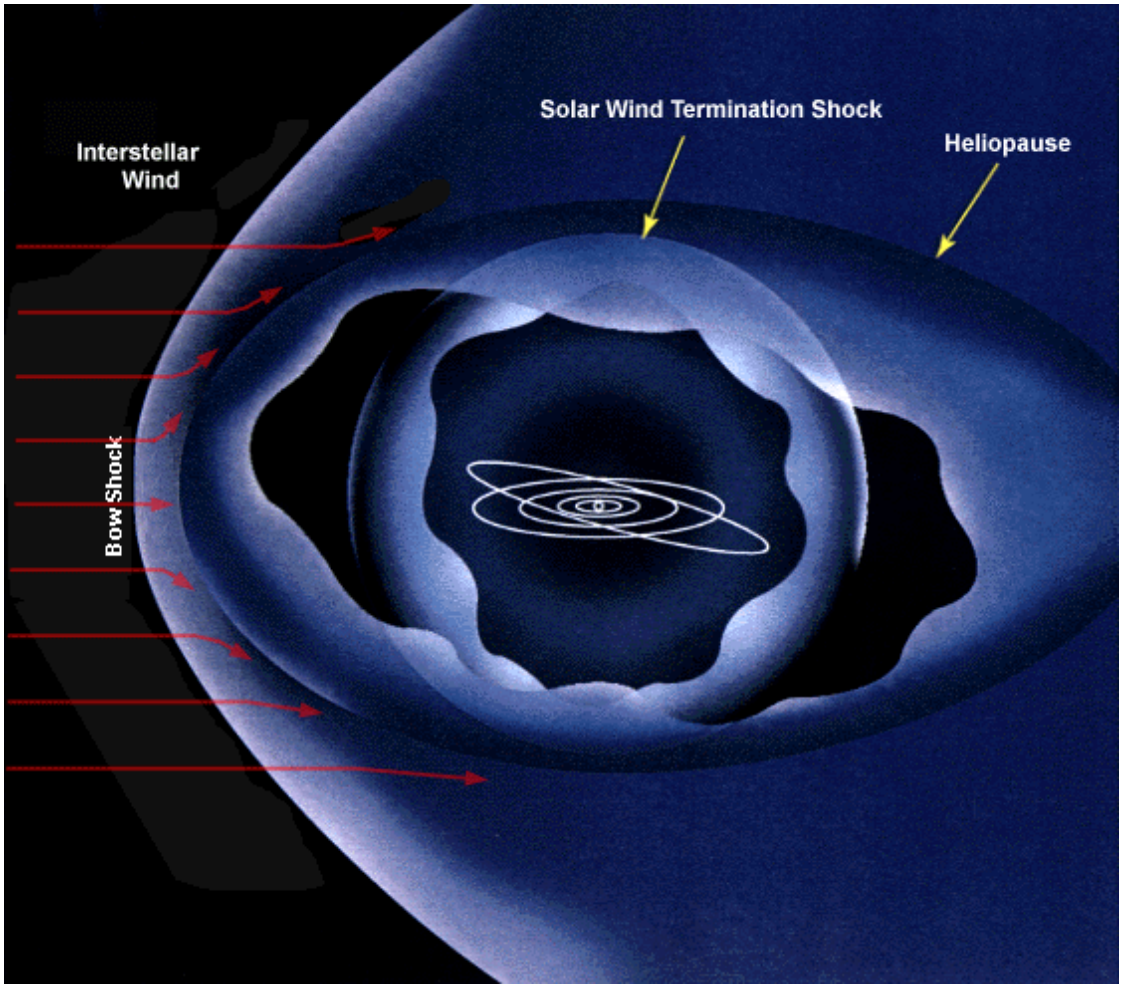

Figure 1.2: Diagram of the heliosphere around the solar system [4].

the interstellar medium. The heliosphere repels charged particles from interstellar space and is filled mostly with the solar wind produced by the sun. Charged particles in the heliosphere are mostly protons, helium ions, and electrons although heavier ions, up to iron, are also present in small amounts. Most charged particles in the interstellar medium do not cross the heliopause. Due to the motion of the solar system relative to the interstellar medium, the heliosphere may form a bow shock at the forward end that domes around the solar system and then forms a long tail on the other side.

1.2 Detecting Neutral Particles

ENA detection offers a method to study the processes that occur between plasmas and the neutral background atoms in space. Since the ENAs are not effected by the electric and magnetic fields that confine the plasma, ENA detectors do not have to be inside a specific plasma to observe these interactions. The measurements provide a global view of the plasma interactions in contrast to the local view gained by detecting plasma ions directly from within the plasma. Reconstructing the three-dimensional plasma object from two-dimensional ENA images is model dependent and is a valuable addition when made in parallel with other observations [5].

This work involves improving detection methods for low energy ENAs. Quantities of interest are atom species and energy. Methods for detecting high and medium energy ENAs can involve their first passing through thin films (50 to 150 nm thick) or ultra thin foils (2 to 20 nm thick) before reaching a solid state detector

where the ENA can be detected and its kinetic energy determined. The secondary electrons emitted from the foils are used as an initial "start" signal to mark the time when the ENA enters the detector and the "stop" signal comes from the solid state detector. This method can yield time of flight and hence energy information [6, 7]. This information, combined with the spatial distribution of detected ENAs can give a global view of a plasma object in space. Low energy ENAs cannot pass through thin films or ultra thin foils, or produce secondary electrons efficiently. One method for detecting low energy ENAs is conversion of the atom to a negative ion by scattering from a conversion surface [8]. Once converted to a negative ion, the ENA may be guided to a detector and counted with nearly 100% efficiency. The main advantage of negative ion conversion is a low threshold energy so the incident ENAs with very low energies can be converted and counted. Conversion to negative ions preserves information about the direction and energy of the ENA.

The sensitivity of a detector based on surface conversion is limited by the efficiency of the target surface in converting the ENA to a negative ion. Many experiments have tested the conversion properties of various surfaces, with extensive research done on metals covered by a layer of cesium or other alkali atoms [9, 10, 11]. Tungsten surfaces covered by a layer of cesium have been found to have some of the highest conversion efficiencies, however reactivity presents practical difficulties in using such surfaces in space instruments. To maintain an uncontaminated alkali layer in a space environment, equipment for cleaning the surface and reapplying the layer is needed. Elaborate equipment to maintain the surface in working condition is a limitation on a satellite or probe because of power, weight and size considerations.

This thesis describes tests of the conversion efficiency of surfaces that have not undergone any special treatment or cleaning. The goal is to find surfaces that have a good conversion efficiency and at the same time resist contamination, thus simplifying the design of a low energy neutral atom detector.

The Low Energy Neutral Atom (LENA) Imager on board the Imager for Magnetosphere-to-Aurora Global Exploration (IMAGE) satellite uses a polished tungsten plate as the conversion surface to produce negative ions. The surface was found to have a conversion efficiency of less than 1% and LENA has been successful in measuring neutral particle fluxes from the Earth's magnetosphere and the sun [12, 13]. The instrument is the first of its type to be flown and, even with its low conversion efficiency, has proved useful in observing the near Earth space environment. Future instrument designs would benefit greatly from an improved conversion surface.

Chapter 2 and 3 contain a brief discussion of the theory of surface conversion and an overview of previous experiments with various surfaces. Chapter 4 deals primarily with the experimental apparatus used for the measurements performed for this thesis and a description of these measurements. The goal is to evaluate the surfaces and compare their relative conversion efficiencies taking into account a number of limitations. The data are presented and discussed in Chapter 5.

Chapter 2

Theory

Theories about charge exchange between an atom and a surface depend on the surface material. Models for charge exchange assume an atomically clean and flat surface and are compared with experimental data obtained from surfaces that have undergone extensive cleaning. In a spacecraft application, it is not possible to maintain a clean surface without added equipment and procedures, which can complicate instrument design. Even if the surface is cleaned and protected during launch, once final orbit has been attained the surface must be exposed and adsorbates can collect from other spacecraft components as they out-gas. In all cases, contamination will alter the electronic structure of the surface. Because overall charge exchange efficiency is affected by the top most layers of the surface, it may depend more on the adsorbed surface material than the surface material itself.

To fit experimental data of negative ion fractions emitted from clean surfaces upon neutral atom collisions models have been used, but calculating the negative ion conversion efficiency of a laboratory surface is a much more involved task. Impurities and adsorbates on the surface can change the electronic processes and affect the reflection and ionization of incident neutral atoms. This experimental study used surfaces that were not extensively cleaned so the applicability of the current theories is limited but can serve as a guide for the organization of the experimental data.

Conversion of an atom or molecule to an ion through surface scattering is usually described by backscattering followed by charge exchange between the atom or molecule on the outward trajectory and the surface. Next is a brief description of the current theory of scattering between atoms and surfaces followed by models of charge exchange for both metal and dielectric surfaces.

2.1 Ion Stopping and Backscattering

Energetic atoms, referred to as projectiles, can penetrate a target material for some distance and scatter from the atoms in the bulk material on or below the surface. The projectile undergoes both elastic and inelastic collisions while inside the target surface. Depending on target thickness and atom penetration, it is possible for the projectile to backscatter from the same side of the target that it entered. Low energy ENAs are more likely to backscatter from the surface rather scatter through the target material to the other side.

Elastic scattering between the projectile and the surface atoms accounts for most of the trajectory deflections and a relatively small fraction of the energy loss for projectiles with low mass compared to the target atoms. Scattering calculations generally use the two particle approximation in which only the fraction of the total energy transferred to the target atom in a binary collision is considered. The fraction is given by

$$\frac{T}{E_0} = \frac{\left(\cos\theta + \sqrt{\frac{M_2}{M_1} - \sin^2\theta}\right)^2}{(1+\frac{M_2}{M_1})^2}, \tag{2.1}$$

where T is the energy absorbed by the target atom, E_0 is the initial energy of the

ion, M_1 and M_2 are the masses of the projectile and target atom respectively, and θ is the scattering angle of the projectile. The maximum energy transfer takes place during a head-on collision, $\theta = 180°$, and becomes smaller as the ratio of the mass of the projectile and the mass of the atom decreases. At high projectile energies, the scattering reduces to Rutherford two body scattering, where the interaction only depends on the charges and masses of the nuclei of the atom and projectile. At lower energies there is a screening effect due to the electrons around the two nuclei that modifies the potential between the atom and projectile. Detailed, accurate calculations of the interatomic potential that account for the states of the scattered particles can be made using Hartree-Fock approximations for the atoms. It can be used for all combinations of atoms but is computationally intensive and better used as a benchmark for comparison with simpler approaches. Potentials are often calculated using a simplified quantum mechanical approach where the projectile and atom are assumed to have spherically symmetrical charge distributions around a point charge at the center representing the nucleus with the shapes of the charge distributions remaining unchanged throughout the interaction [14, 15]. From the approximate charge distributions of the atom and projectile, the interatomic potential is calculated, and then used with the initial energy and the impact parameter of the collision to determine the scattering angle and transferred energy. The projectiles generally undergo multiple collisions in a specific target and the energy loss can be expressed as a continuous function. The nuclear stopping cross section, $S_n(\mathrm{E})$, gives

the average energy lost by the projectile per unit path length

$$N \times S_n(E) = \frac{dE}{dR}, \tag{2.2}$$

where N is the atomic number density of the target, E is the projectile energy and R is the path length inside the target. For a given incident ion energy, the stopping cross section can be used to give an average distance that the projectile travels in the target before it becomes embedded. This model is classical and provides a simple approximation for each atomic collision in the target material.

Ions in solids undergo inelastic energy loss largely due to kinetic energy transfered to the electrons in the target, also referred to as electronic stopping. Inelastic collisions account for most of the energy loss for energetic light ions in solids. An early classical description of this problem by Niels Bohr was extended by Bethe and Bloch using quantum mechanics and remains the basic method for calculating energy loss [16]. This approach is applicable to fully stripped ions moving much faster than the electrons in the target, and is usually assumed to be valid for energies above 1 MeV/amu. At lower energies, experimental data on hydrogen stopping cross sections can be scaled to heavier ions for the same target and velocity. For particles moving slower than the valence electrons in the solid, electronic stopping has also been addressed by Fermi and Teller [17]. Electronic stopping has very little effect on the direction of the ion as it moves through the solid. Stopping cross sections for the electronic interactions can be constructed to calculate the inelastic energy loss of the projectile and whether it becomes embedded in the target.

Estimation of the angular and energy distributions of backscattered negative

ions from a surface were performed with SRIM 2006 (The Stopping and Range of Ions in Matter) software. The software uses the Monte Carlo method to calculate ion ranges and was developed by J. F. Ziegler *et al.* [14]. A random number is seeded into the energy and direction calculation for each collision event, and the results are averaged over the path traveled between collisions. The SRIM code is based on screened Coulomb potentials between the projectile and target atoms and also includes effects from the overlap between the electron shells of the colliding particles. Comparison of SRIM stopping power calculations with experimental results varies for different ions and atoms but generally 80% of the measured and calculated values agree within 10% for projectile energies above 1keV/amu. In the present work, the applicability of SRIM simulations is inferred by its agreement with the measured angular distributions (see Chapter 4). SRIM simulations allow limited angular measurements to be extended beyond the range of the instruments.

2.2 Charge Exchange between Atoms and Surfaces

2.2.1 Metal Surfaces

Electron transfer between atoms and metal surfaces is often described as a resonant charge exchange between the conduction band of the metal surface and the valence level of the atom. The following is a discussion the resonant charge transfer (RCT) model (schematic shown in Fig 2.1, as described by Rasser, van Wunnik and Los [18]). Atomic units are used throughout unless otherwise specified.

The electron affinity level of an atom is the energy difference between a neutral

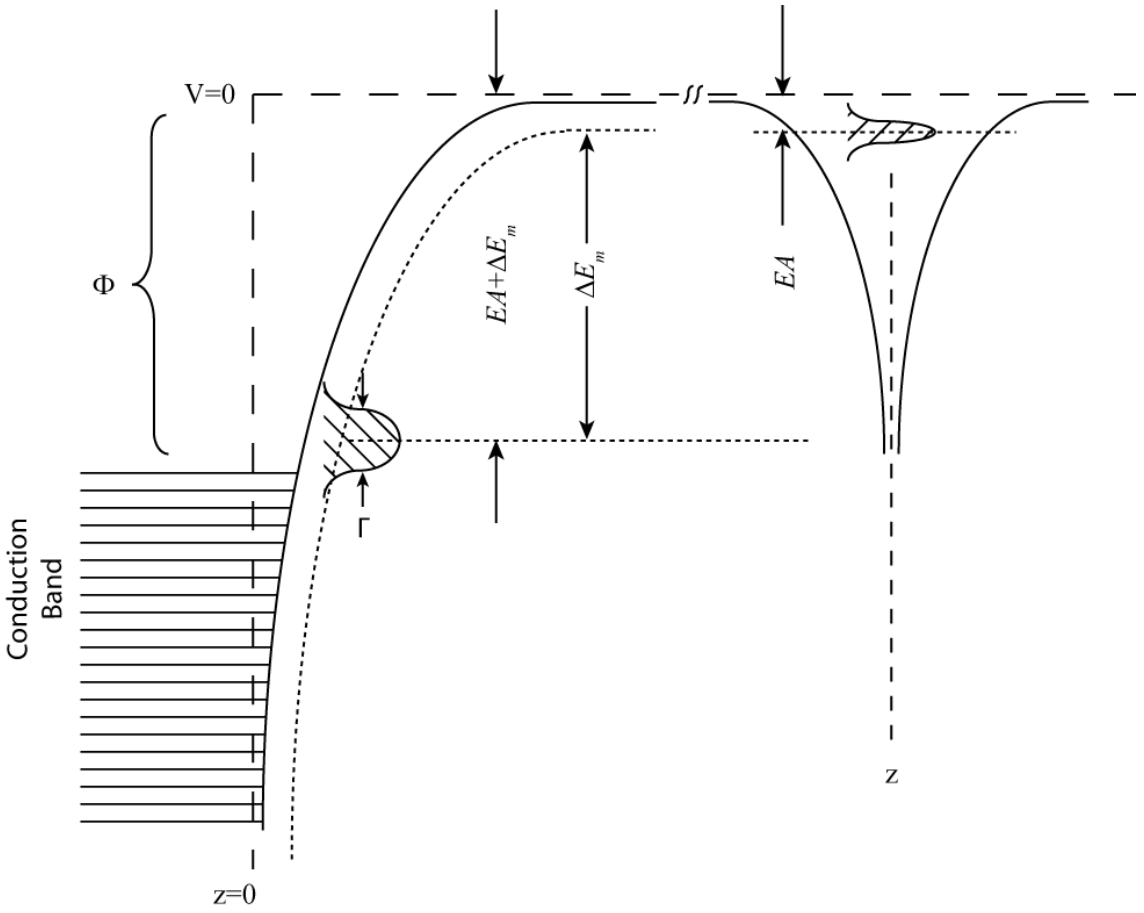

Figure 2.1: A schematic diagram of the resonant charge transfer model interaction between an atom and a metal surface placed at z=0 with a work function of Φ. At position z, the electron affinity (EA) of the atom lies above the conduction band of the metal. Upon approaching the surface, the affinity level is lowered by ΔE_m and broadened by Γ. Resonant transitions occur when the energy of the metal conduction band and the electron affinity of the atom are similar.

atom and its anion. The lower the electron affinity is, the more likely an atom is favored to gain an electron. As a hydrogen atom approaches a metal surface, the electron affinity level is lowered and broadened by the interaction between the atom and the induced image charge in the surface. The electron affinity level of the atom will shift below the conduction band of the metal at close distances allowing electrons to make transitions between the metal and the atom. The shift in the affinity level, ΔE_m, is given by the potential between the charge and its induced image charge in the metal

$$\Delta E_m = \frac{1}{4(z + z_0)}, \tag{2.3}$$

where z is the distance between the atom and the surface and z_0 is a displacement due to the screening length of the metal [19]. The potential given by a classical image charge is not explicitly valid for atom distances less than 10 a_0 to the surface because the induced charge on the surface is not perfectly planar and will include dipolar and higher multi-polar interactions [20]. However, the image potential has been shown to be a good approximation at distances as close as 4 a_0 [21]. The broadening of the affinity level is attributed to the interaction between the atom states and the metal states allowing an electron to resonate between them resulting in a finite lifetime of the atom state. The electron affinity level band will have a finite width because of the Heisenberg uncertainty principle [22]. The level broadening is given by $\Gamma = \hbar\omega$, where ω is the transition frequency obtained from Fermi's Golden Rule

$$\omega = 2\pi \sum_{i,f} |< i|H'|f >|^2 \rho(E), \tag{2.4}$$

where $\rho(E)$ is the density of states in the metal, $|i>$ and $|f>$ are respectively the initial state of the neutral atom and the metal, and the final state of the ion and metal. The sum is over the degenerate states of the metal and negative ion, that is, the states of the two systems that share the same energy value. The relevant terms in the total Hamiltonian only involve the coordinates of the transferred electron and the image potentials induced by the atom as it nears the surface, see Fig. 2.2 for the meanings of r_1, r_{12}, d_1, D_1 and $D_1^{'}$.

$$H_1 = -\frac{1}{2}\nabla_1^2 - \frac{1}{r_1} + \frac{1}{r_{12}} - \frac{1}{4d_1} + \frac{1}{D_1} + \frac{1}{D_1^{'}} \tag{2.5}$$

This Hamiltonian can be further split into soluble and perturbative parts, analogous to the situation between a metal surface and neutral atom [23, 24]. For a metal ion perturbed by a nearby neutral atom, the perturbed Hamiltonian takes the form

$$H' = -\frac{1}{r_1} + \frac{1}{r_{12}}, \tag{2.6}$$

and is substituted in Eq 2.4 to evaluate the transition frequency of the electron.

A stationary atom above a metal surface will be in a charge state that depends on the overlap between the widened electron affinity level and the metal conduction band. The equilibrium charge state of the atom, $n^-(z)$, can be expressed as

$$n^-(z) = \frac{1}{\pi}\int_{-V_0}^{-\Phi} \frac{\frac{\Gamma(z)}{2}}{(E + EA + \Delta E)^2 + \frac{\Gamma(z)^2}{4}} dE, \tag{2.7}$$

where $-V_0$ is the bottom of the conduction band, determined in the free electron model by the sum of the Fermi energy and work function of the metal [25]. The equilibrium charge state can be thought of as the negative ion fraction of a number of hydrogen atoms sitting above a metal surface at distance z.

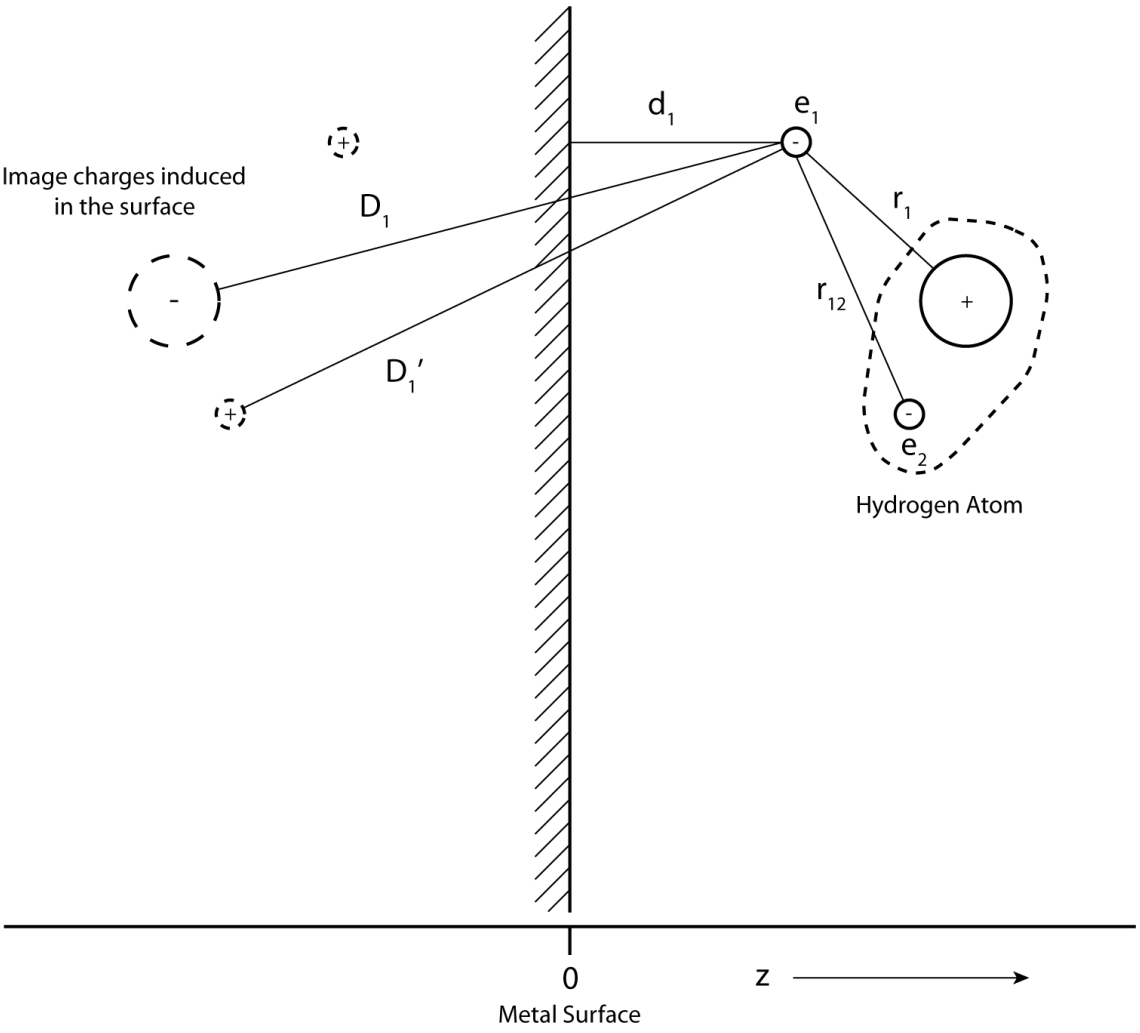

Figure 2.2: Image interaction model between a negative hydrogen ion and a metallic surface. The electron e_1 can move between the conduction band states of the metal and the negative ion state for z small.

Given a system where the initial charge state $P_i(0)$ is not equal to the equilibrium value, the time evolution of the system is given by the rate equation

$$\frac{d}{dt}P_i(t) = \omega(z)[n^-(z) - P_i(t)]. \tag{2.8}$$

The charge state will evolve with a time constant equal to $w^-(z)$ and will converge to the equilibrium charge state for $t \to \infty$. Using a straight line approximation for the outward trajectory and z_0 as the turning point or closest distance to the surface where a negative ion is possible, the rate equation can be expressed as a function of distance,

$$\frac{d}{dz}P_i(z) = \frac{\omega(z)}{v_\perp} \cdot \big[n^-(z) - P_i(z)\big]. \tag{2.9}$$

The final negative charge fraction of a system of atoms leaving the surface is then the rate equation integrated from the turning point to infinity,

$$P_i(\infty) = P_i(z_0) \cdot exp\left[-\int_{z_0}^{\infty} \frac{\omega(z)}{v_\perp} dz\right] + \int_{z_0}^{\infty} n^-(z) \cdot \frac{\omega(z)}{v_\perp} \cdot exp\left[-\int_{z_0}^{\infty} \frac{\omega(z')}{v_\perp} dz'\right] dz. \tag{2.10}$$

The first term describes the decay of the initial negative ions present at the turning point and the second term is the formation of negative ions along the outward trajectory. The initial negative charge fraction, $P_i(z_0)$, is approximated as the equilibrium charge state at the turning point of the atoms, $n^-(z_0)$.

The above equations only take into account the perpendicular velocity of the atom motion. The parallel velocity can affect the image charge screening between the metal surface and atom. Boyer showed that the screening is not affected by the parallel velocity so long as

$$\frac{\eta v_\parallel}{d} \ll 1, \tag{2.11}$$

where η is the resistivity of the metal, $v_{\parallel}$ is the parallel velocity component of the atom and d is the distance separating the atom and metal surface and are evaluated in CGS units, which gives a unitless result [26]. The parallel velocity component is introduced in this scheme as a velocity shift between the electrons in the target metal and the atom [27, 28]. Only electrons with a velocity approximately equal to the parallel velocity of the atom can make the transition from the surface. This does not affect the transition rate, but instead changes the equilibrium charge state of the system because it alters the overlap between filled electron states and states that are in resonance [29]. In most cases, $n^{-}(z)$ is lower than in the 0 $v_{\parallel}$ case. Measurements of the $v_{\parallel}$ dependence in the above literature are based on ion fractions collected by adjusting the incident energy and angle, and detection angle to achieve constant $v_{\perp}$. The energy range used in this experiment and the metal resistivities are low enough to not affect the metal screening, so the affinity level changes do not differ from the $v_{\parallel} = 0$ case.

The RCT model depends on many different surface and atom properties to predict negative ion formation. The width and shift in the projectile affinity level determine the distances between the atom and surface where charge exchange is possible. These changes are not fully understood at very close distances, where charge exchange is most probable, and errors introduced there can cause over- or under-estimation of charge exchange fractions by orders of magnitude. The main surface properties are work function and Fermi energy. These properties are used to calculate the equilibrium charge state the projectiles at some distance from the surface. Low work functions allow charge exchanges to occur at greater distances

from the surface and a high Fermi energy increases the interval of the integral in equation 2.7, which will increase the value of the equilibrium charge state of the projectile above the surface.

2.2.2 Dielectric Surfaces

Dielectric surfaces have not been studied to the same extent as metal surfaces for charge exchange characteristics, but measured negative ion fractions of hydrogen and oxygen from silicon at incident energies between 1 and 4 keV show efficiencies comparable to a clean aluminum surface [30, 31, 32]. A number of other studies exist on the formation of H^- and O^- ions on diamond surfaces [33, 34, 35]. Resonant tunneling, as described above, cannot occur due to the existence of a band gap. For silicon, negative ion formation is often attributed to the dangling bonds that are present on the surface layer of a bulk crystal and a non-resonant charge exchange with the electron affinity level of the atom [36]. This mechanism was also used to explain the appearance of O^- ions after dissociative scattering of NO^+ ions on a GaAs surface [37]. The angular dependence observed for O^- scattering from the surface was explained in terms of the interactions with the surface sites where dangling bonds exist. However, unless the surface is cleaned extensively, dangling bonds will form an oxide layer which will alter the electronic interaction between the surface and incident beam.

Surface sites are used to explain the negative ion fractions observed in scattering from ionic compounds, such as MgO and LiF. The surface is divided into

active and inactive sites. When scattering from an ionic crystal at grazing angles, the atom passes over the surface and can interact with an active site and gain an electron. In the case of ionic compounds, the active site is assumed to be located around the cations in the solid. The electronic band gap of the surface inhibits electron loss from the ion, increasing the survival of negative ions as they move away from the surface [36]. In the case of alkali-halide surfaces, the valence band electrons are localized around the halogen atoms [38]. Electron binding energies can be approximated by a free ion modified by the Madelung potential of the crystal [39]. Charge exchange can be viewed as a binary interaction between the atom and the active site with all other crystal ions acting as point charges. This model can also include oxide surfaces such as MgO, by taking into account the doubly charged ions in the crystal [40].

In the model of Borisov and Esaulov the transition efficiency depends on the energy difference ΔE_d, between the initial $(Surf^- + A^q)$ and final $(Surf^0 + A^{q-1})$ states of the atom passing over an active site [36].

$$\Delta E_d(\vec{R}) = E(Surf^0 + A^{q-1}) - E(Surf^- + A^q) \tag{2.12}$$

Here $Surf^-$ is the active site on the surface and A^q is the projectile atom at a distance R from the active site. Neglecting any polarizing effects and keeping $\vec{R}$ large enough to avoid any overlap between the projectile and the electron cloud of the active site and taking into account the interaction energy between the surrounding surface point charges the energy difference becomes

$$\Delta E_d(\vec{R}) = \varepsilon_{Surf} - \varepsilon_A + \sum_i \frac{q_i}{|\vec{r}_i|} - \sum_i \frac{q_i}{\left|\vec{R} - \vec{r}_i\right|} + \frac{q}{R}. \tag{2.13}$$

Here, ε_{Surf} and ε_A are the binding energies of the free surface site ion and projectile respectively, q_i is the charge of the non-active sites in the crystal surface located at $\vec{r}_i$ from the active site. The third term of Eq. 2.13 is the energy between the active site and all other sites in the crystal, the fourth term is the difference in energy between the point charges and projectile in the initial and final states. The last term is the interaction between the projectile and the active site.

As the projectile atom passes over the ionic crystal, it will undergo multiple interactions with sites along the surface. At distances close to an active site, ΔE_d can be considered constant and the Demkov-Nikitin near-resonant electron transfer model can be used to find the charge exchange probability [41]. The estimated charge transfer probability from the active site to the projectile becomes

$$P^{site} = \frac{1}{2} sech^2 \left(\frac{\pi}{2} \frac{\gamma \cdot \Delta E_d}{v} \right) \tag{2.14}$$

with

$$\gamma^{-1} = \frac{\left(\sqrt{2\varepsilon_{Surf}} + \sqrt{2\varepsilon_A} \right)}{2} \tag{2.15}$$

where v is the velocity of the projectile and γ characterizes the decay of the electron transfer interaction energy. Ignoring any destruction mechanisms, where the extra electron is transferred back to the surface, the final probability of forming a negative ion over the surface becomes

$$P^{total} = 1 - \left(1 - P^{site}\right)^N, \tag{2.16}$$

where N is the number of interactions between the projectile and active surface sites along its trajectory.

Destruction of the negative ions above the dielectric surface affects the total conversion efficiency. The projectile affinity level as a negative ion can be in the range of the conduction band level of the surface [42]. In this case, resonant charge exchange is possible from the projectile atom back to the surface as previously described in the RCT model. When the affinity level does not overlap with the conduction band, resonant charge exchange is still possible as a result of the velocity of the projectile [43]. The surface band structure, when viewed in the reference frame of the projectile, may allow resonant charge exchange that is not possible in the static case. The parallel velocity of the negative ion over an ionic crystal introduces an oscillating electric field from motion over the localized electronic structure of the surface. Resonant coherent excitation of the ion can cause electron transfer back to the surface for sufficiently high parallel velocities [44, 45]. These loss mechanisms are very specific to the target and projectile combinations.

2.3 Summary

Predicting negative ion formation on surfaces from theory is difficult for surfaces that are not ideal. Surface roughness, defects and adsorbates will affect the final charge states of scattered atoms. Even with ideal surfaces the models used are often simplified to make the calculations easier. The resonant charge exchange model has been applied to experimental results using fitting parameters. The screening length was used as a fitting parameter to evaluate the H^- fraction from a cesiated tungsten surface using the RCT model for an incident H^+ beam of 100 eV [9]. The

theoretical negative ion fraction was then calculated for 200 eV and 400 eV beams and showed reasonable agreement with experiment. However, the fitting parameter screening length was twice as large as the screening length calculated directly from the electron density of the surface. Nevertheless the model can be useful in approximating the behavior of charge exchange over energy and angular ranges but is ultimately limited in predicting absolute charge exchange fractions in the absence of experimental data to establish the values of the adjustable parameters.

Chapter 3

Review of Previous Experiments

Scattering particles from surfaces has a long experimental history beginning with the α-particle scattering experiments of Gieger and Mardsen in 1909 [46, 47]. Scattering experiments have expanded over time to include many different types of projectiles and targets and a wide variety of applications. Surface conversion to negative ions is a relatively recent approach as a detection method for neutral atoms in space, formulated in the 1990s [48]. Since then, a number of experiments have used grazing collisions with surfaces to investigate the charge states of backscattered particles.

Detecting low energy neutral atoms using surface conversion to negative ions was first put into practical use by the LENA imager aboard the IMAGE spacecraft, launched in 2000 by NASA [49]. Previous spacecraft instruments for detecting neutral atoms used different techniques to detect ENAs in the medium to high energy ranges. LENA used a polished polycrystalline tungsten surface to convert the incident low energy neutral atoms into negative ions and a strong electric field to guide the ions into a spherical electrostatic analyzer for detection. The tungsten surface was calibrated at the University of Denver and the University of Bern to determine the conversion efficiency. Conversion efficiency measurements were made using incident atoms of H and O on the bare tungsten surface as well as the surface

covered with a layer of cesium. The measured conversion efficiency using H atoms for the cesiated surface was about 2% and the bare surface conversion efficiency was about 1% over the energy range tested. The cesium covered surface was not used in the flight instrument due to the increase in surface maintenance equipment needed to keep the surface free of contamination.

In many of the references to conversion efficiency experiments, the reported measurement was the ratio of negative ions reflected from the surface to all ions and neutrals reflected from the surface, referred to here as the ion fraction. In the LENA work, the measurement of interest is of the ratio between the negative ion flux scattered from the surface to the total incoming neutral flux, referred to here as the conversion efficiency. In general, the ion fraction will be higher than the conversion efficiency due to implantation of part of the incident beam in the surface however, ion fractions can be used to infer the total conversion efficiency if enough is known about the fraction of incident beam particles that are captured by the surface after impact.

The following chapter reviews a number of surface experiments that measured the negative ion formation efficiency of different materials. The focus of the experiments was not always negative ion detection but they still provide data on surface negative ion formation.

3.1 Metal Surfaces

Tungsten surfaces have been studied for H^- formation using 1000 eV beams of H^+ and H_2^+ by Levine and Barry [50]. The ions were directed perpendicular to the surface plane and the negative ions produced were focused into a detector. The authors observed two peaks in the negative ion current, a high energy peak corresponding to the converted negative ions from the incident beam and a low energy peak which was determined to be due to secondary ion emission from adsorbed material on the surface. These low energy ions had energies below 25 eV, leaving a great difference between the energies of the secondary ions and the scattered ions which had maximum intensity at 150 eV or above. The low energy peak was completely removed by heating the surface to about 925℃ to remove the adsorbates. Secondary ion emission measurements performed on tungsten, by McCaughan, Sloane and Geddes, showed similar results [51]. In this experiment, the secondary ion intensity was measured to be about two orders of magnitude less than the intensity of the reflected incident 965 eV H_2^+ beam. The low energy peak intensity was around 10 eV compared to the high energy reflected component with maximum intensity at about 300 eV.

Overbosch, Rasser, Tenner and Los studied the temperature dependence of surface ionization using a neutral beam of sodium atoms, in the energy range of 30 to 500 eV, on a tungsten surface heated between 27℃ and 1725℃ [52]. These measurements were designed to look at the change in ion fraction as a function of surface temperature rather than the change in ion fraction as the adsorbates are

removed from a surface by heating. The particles from the surface are detected with an electron multiplier that had a grid maintained at a positive potential to remove ions so that only neutrals from the surface were detected. Both a decrease in the ion fraction and an increase in the neutral flux from the surface was observed as the temperature was increased. Over the range of temperatures, the ion yield showed a small decrease in relative ionization efficiency as the temperature increased. The measurement started at 225℃, at which temperature water layers are removed and adsorbates evaporated from the surface.

Cesiated tungsten has been considered a good conversion surface candidate because of its low work function. Van Wunnik *et al.* have studied charge exchange on a monocrystalline (110) tungsten surface covered with cesium using incident beams of H^+ between 100 and 2000 eV [27, 53]. Using a kelvin probe, the lowest point of the work function, 1.45 eV, was measured to correspond with a coverage of half a monolayer of cesium on the surface, and was used in the experiment. Measured angular distributions for H and H^- atoms show most reflection to be near-specular for the three incident angles of 5°, 10° and 15°, measured from the surface plane. The energy distributions show a double peak structure attributed to differences between reflection at the cesium or the tungsten layer. Total conversion efficiency was measured over a range of incident energies and angles. The highest efficiencies exceeded 30%, for a 200 eV beam incident between 5° and 12° from the surface plane.

The efficiency for a polycrystalline cesiated tungsten surface tested in the same apparatus as the monocrystalline sample was about 27% and compares well with

the results for the cesiated monocrystalline surface from above [27, 53]. Another polycrystalline tungsten surface covered with cesium was studied by van Bommel *et al.* in a different experiment and compared with the work above [54]. The work function of the surface was measured to be 1.68 eV for about half a monolayer of cesium coverage. The conversion efficiency only reached about 12% for this surface for a beam of 400 eV incident H^+ at 5° to the surface.

van Slooten *et al.* studied the conversion efficiency of silver covered with barium, another low work function surface [55, 56]. The tests were performed on a clean Ag(111) surface covered with about two monolayers of barium, which has a work function of about 2.6 eV. The surface was briefly transferred in air to the testing chamber after preparation. Observed H^- ion fractions were still comparable to the cesiated surfaces and are attributed to the barium surface having a higher density of electrons and a wider conduction band than cesium. The tests used an H^+ beam between 500 and 1000 eV at 10°, 30° and 50° to the surface. H^- ion fractions up to about 23% were measured depending on the incident and reflected angles.

Adsorbate covered surfaces are not discussed in the literature as extensively as clean surfaces. DeFazio and Peko studied adsorbate covered polished copper surfaces using beams of neutral H-atoms. They observed differences between the conversion efficiency of the surface when clean and adsorbate covered [57, 58]. The surface was cleaned in the vacuum chamber by heating it to between 600 and 800℃ for 20 to 30 minutes. The conversion efficiency for the surface was measured to be about 0.5% before heating, but dropped to undetectable levels after the surface was heated. The efficiency recovered after the surface was allowed to cool and re-adsorb

residual gases in the vacuum chamber.

3.2 Non-Metal Surfaces

Wieser, Wurz, Brüning and Heiland have measured negative ion formation from a polished magnesium oxide single crystal (100) surface [59]. The negative ion fraction measured from the surface was about 3% for a 300 eV incident H^+ beam at 5° from the surface. The efficiency was observed to increase with increasing beam energy and reached 7% for a 1500 eV beam. Measurements were also taken using incident beams of O^+. Conversion of oxygen atoms to negative ions was considerably more efficient than for hydrogen. The ion fraction was found to be about 12% for an incident beam of 90 eV and increased to 30% for a 3000 eV beam. No significant change in the ion fraction was observed while varying the crystal orientation with respect to the incident beam. Similar experiments were performed at the same facilities for a barium zirconate surface [60]. The surface consisted of a $BaZrO_3$ film about 20 nm thick deposited on a polished W(110) crystal. Ion fractions for H^- ions from the surface ranged from 3 to 5% for incident beam energies from 300 to 1500 eV. Oxygen negative ion fractions ranged from 22 to 35% over the energy range or 500 to 3000 eV. The negative ion fraction was found to increase with the incident beam energy.

The negative ion fractions from an aluminum nitride surface were measured for incident beams of H_2^+ and O_2^+ ions by Jans *et al.* [61]. The surface was tested at incident angles between 0° and 90° to the surface and energies ranging from 450 to

2000 eV. The incident angle and energy of the beam were varied to systematically investigate the change of conversion efficiency with parallel and perpendicular velocity to the surface. For a constant perpendicular velocity, the ion fraction decreased as the parallel velocity increased for both hydrogen and oxygen beams. Overall, the ion fraction was found to be about 1% for hydrogen and 15% for oxygen.

Diamond surfaces have been studied as candidates for surface conversion based neutral atom detectors. Diamond is chemically inert and stable, properties that are advantageous for long term space missions. Wurz, Schletti and Aellig have measured ion fractions from a polycrystalline diamond surface using incident H_2^+ and O_2^+ beams between 300 eV to 800 eV at an incident angle of 8° [33]. The ion fraction was measured by comparing the neutral component of the reflected beam with the total reflected beam. No positive ions were reported in the reflected beam. A peak negative ion fraction of 5.5% for an incident hydrogen beam at 400 eV was reported. For the O_2^+ beam, the ion fraction was about 29% at all tested energies. These results were shown to be stable for over two weeks, however the surface was heated to about 500℃ before each set of measurements was performed, effectively cleaning the surface of water. Scheer, Brüning, Fröhlich, Wurz and Heiland studied the ion fractions from a diamond surface with a beam of neutral O_2 molecules [34]. The energy range investigated was from 400 to 3000 eV. The measured ion fraction reached the 10% range for higher energies but was of the order of 1% for a beam energy of 1188 eV.

3.3 Summary

The experiments on the charge state of backscattered atoms have used many different surfaces. It was established that heating decreases the conversion efficiency of the surfaces and a greater fraction of incident oxygen atoms are converted to negative ions than incident hydrogen atoms for the same energy and surface. Negative ion fractions were observed to increase as the energy of the incident beam was increased. The surfaces of the experiments are tested under a variety of conditions. Many of the experiments recorded the percentage backscattered ions of the total number of backscattered particles as opposed to the incident beam flux. Chapter 4 gives the details of the apparatus used in this experiment to make negative ion conversion efficiency measurements as a percentage of the number of particles in the incident beam. This work tested many different surfaces under the same conditions so that comparisons of the conversion efficiencies could be made in order to identify the most useful materials for low energy negative ion detectors.

Chapter 4

Surface Conversion Efficiency Experiments

Conversion efficiency tests were performed using two different neutral beam systems. Detailed measurements on the angular and energy distributions of the reflected negative ions were performed at the University of Denver. The results of the detailed measurements were used to design and calibrate a negative ion lens for general measurements of different surfaces to compare the conversion efficiencies at the University of Maryland, College Park. The systems were contained in vacuum chambers that operated in the high vacuum region (10^{-3} to 10^{-9} torr). In both systems a beam of neutral particles is allowed to back scatter from the test surface at a grazing angle. Negative ions that backscatter from the surface are detected and compared to the intensity of the incident neutral particle beam. The following section describes the two systems used to perform conversion efficiency measurements on surfaces. The first section describes the system at the University of Denver, the second section describes the system at the University of Maryland, College Park (UMCP). The last section describes the different surfaces that have been tested in the two systems.

The systems make different but complimentary measurements of the converted negative ions from the surfaces. The Denver system was designed to make angular and energy resolved measurements of the backscattered negative ions. These

measurements are made by a detector pointed at the surface with a small field of view. The detector could be moved with respect to the surface but was limited to a range of angles in the plane perpendicular to the test surface. The Denver measurements provide detailed information about a certain backscattering angle from the surface, and when repeated at different angles can be used to quantify the energy and angular distributions of the backscattered negative ions from the surface. The UMCP facility is designed to collect backscattered negative ions integrated over a wide range of energies and angles. A single measurement collects a wide range of backscattered negative ions from a surface that would require a series of separate measurements with the Denver system. The Denver system was used to take detailed measurements on the backscattered negative ions from a surface to be used as a base surface. The UMCP system was used to collect general information on the overall conversion efficiency of many surfaces that can be compared to the base surface measurements from Denver to determine if the conversion efficiency is an improvement or not.

4.1 University of Denver

The first tests were done at the neutral beam facility at the University of Denver on tungsten and diamond like carbon (DLC) surfaces. The Denver apparatus consists of two differentially pumped vacuum chambers, one containing the beam source and the other containing the target and detector. In the first chamber a beam of 1000 eV hydrogen ions is formed by an ORTEC duoplasmatron source,

model 358 [62]. The beam ions pass through a 60° magnetic-sector mass analyzer, where H^- ions are separated from the other ions and then sent through a 2 mm diameter aperture. This H^- beam then passes through a series of focusing and energy changing electrodes maintained at the appropriate voltages to produce an ion beam at the test energy. The beam energies used were between 20 and 925 eV and the energy distributions of the ions in the beam were approximately Gaussian with a full width at half maximum of 3 eV independent of energy [57]. Finally the ion beam is deflected by 9° to remove neutral atoms that have formed previously by charge exchange with the neutral background gas, and is directed into the second chamber.

The components inside the second chamber are the photodetachment region, the sample and the detectors (shown in Fig. 4.1). In the photodetechment region, the negative ion beam is illuminated by an yttrium aluminum garnet (YAG) laser beam of wavelength 1060 nm, producing neutral hydrogen atoms by the reaction

$$H^- + h\nu \rightarrow H + e^-. \tag{4.1}$$

The photon energy is sufficient to remove the extra electron from the ions but not enough to excite the atoms above the ground state. 5% to 10% of the negative hydrogen ions are neutralized in this manner. The laser is chopped at 40 Hz, so that the beam consists of alternating regions of ions and ions mixed with neutrals. The beam travels through an ion repeller that removes the ions [62]. The ion repeller focuses the ion portion of the beam into a faraday cup that detects the ion current. The modulated neutral beam is the difference between the laser on and laser off

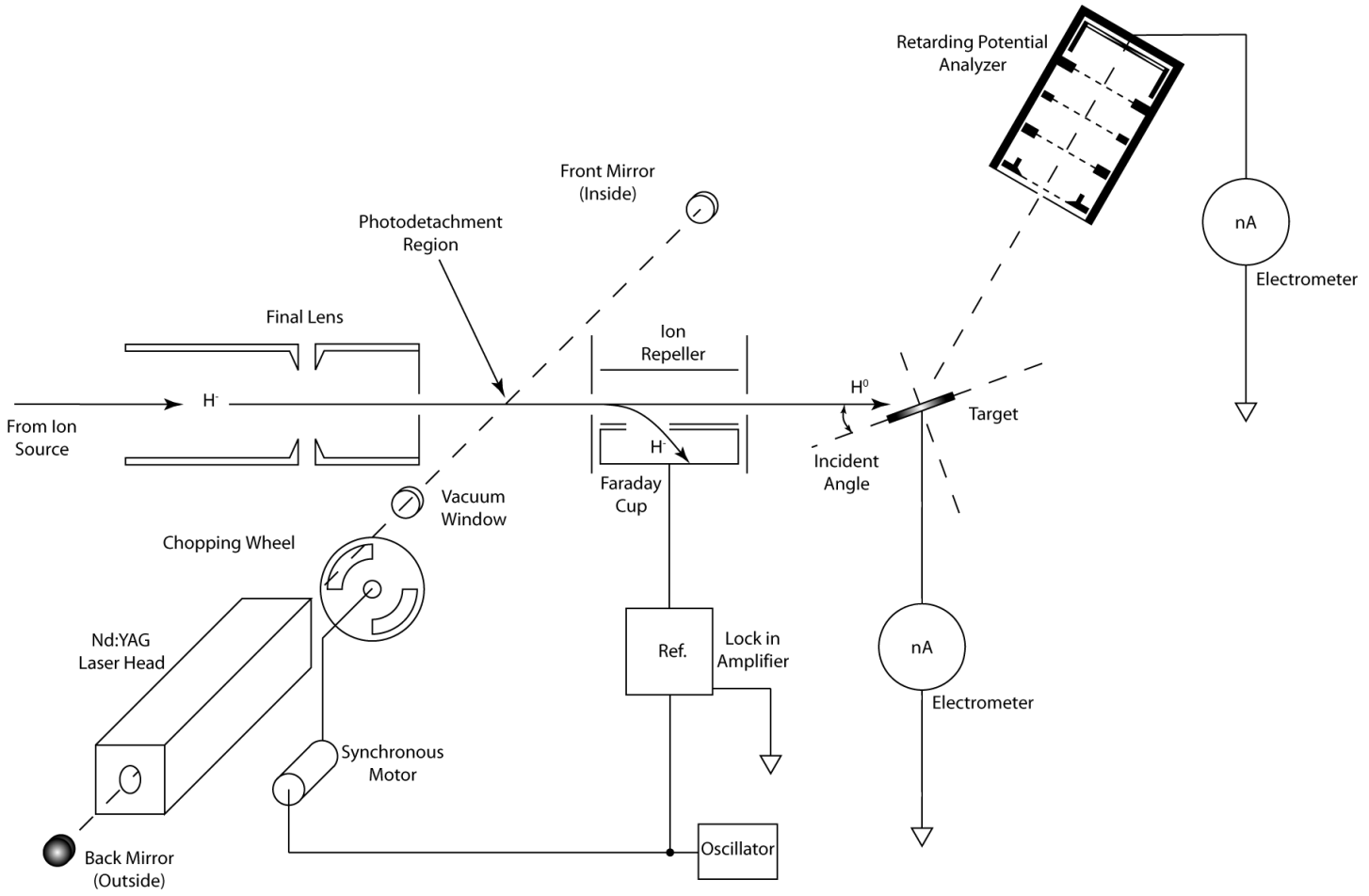

Figure 4.1: Schematic diagram of the essential components in the second vacuum chamber at the University of Denver Beam facility.

signal in this faraday cup. The neutral beam intensity was in the 10^{10}/s range. Neutral atoms produced in this manner essentially retain the energy and direction of their parent ions.

The neutral beam scatters from the target surface on a movable stage positioned after the ion repeller. The stage holds the target in the beam path and can be rotated to change the incident angle of the beam with respect to the surface. The incident beam angle can be set with an uncertainty of 2°. The stage can be heated by a heating coil mounted underneath the target surface. The temperature of the stage is monitored by a thermocouple. The stage can be heated to 300℃ while measurements are being taken. It can also be heated up to 800℃ by electron impact, but cannot be maintained at that elevated temperature without heating other components in the vacuum chamber to temperatures that affect measurement accuracy. Because the stage must be biased positive with respect to the electron impact heating source, the trajectories of the negative ions leaving the surface are distorted, affecting angular and energy distribution measurements. The precise temperature of the surface cannot be accurately measured, but it was observed that while heating to 800℃ the stage would glow red but the tungsten surface remained dark by comparison. Heating the stage from room temperature to 300° required about 40 minutes with the heating coil, 10 minutes were required to reach 800℃ using electron impact.

Negative hydrogen ions scattered from the surface passed into retarding potential analyzer (RPA) situated in the plane of the incoming neutral beam and perpendicular to the surface. The RPA consists of an opening aperture of 6.4 mm

at 63.5 mm from the target surface, a series of four grids and a faraday cup set behind the grids. The RPA has a 6° solid angle view of the surface. The transmission efficiency through the four grids was measured optically to be 58%. Only the grid closest to the faraday cup is biased during the measurements, the other grids are grounded.

The RPA measures the ion current leaving the surface and passing through the entrance aperture, grids and collected by the faraday cup. The RPA can be rotated within a limited angular range in the plane perpendicular to the surface in order to observe different scattering angles. Taking a measurement with all of the RPA grids grounded gives a current that includes all of the ions and secondary electrons from the surface. The secondary electron component is removed by an RPA grid potential that is 20% of the potential used to accelerate the incident beam. For example, secondary electrons produced by an incident beam of neutral H at an energy of 100 eV will be removed from the current measurement of the RPA by applying a -20V potential. Making the grid voltage more negative will remove negative ions from the measured RPA current and the difference in current between two voltages measures how many of the negative ions were removed between the energies removed by the change in grid potential. The plot of current measured by the RPA as a function of the RPA grid voltage is called an integrated energy distribution (Fig. 4.2 left). The RPA current (I_{fc}) measurement is normalized by the ion repeller measurement of the full beam current (I_0) to remove fluctuations in the integrated energy distribution due to changes in incident beam intensity.

Energy distributions (Fig 4.2 right) were obtained by numerically smoothing

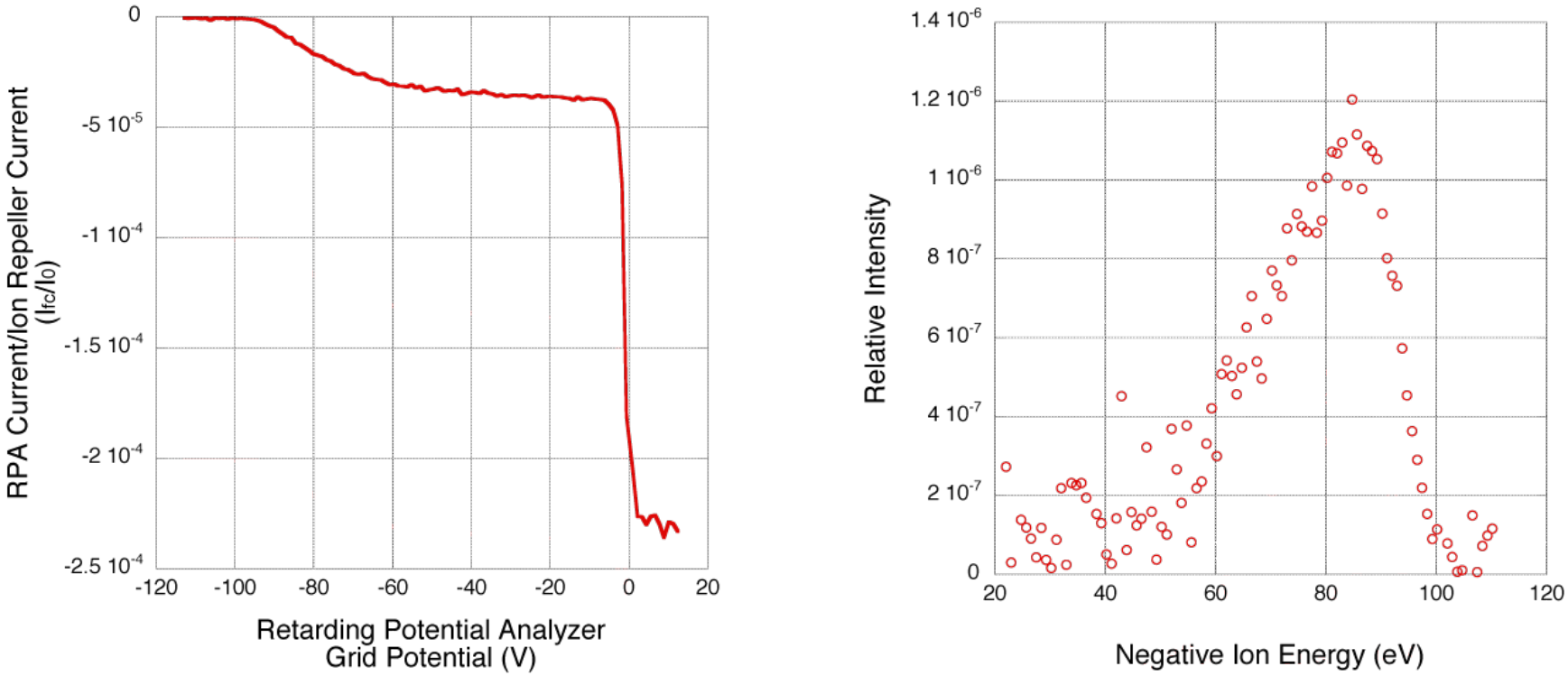

Figure 4.2: The integrated energy distribution (left) and energy distribution (right) for a 100 eV H^- ions undergoing specular reflection at 15° to the surface of the tungsten surface. The integrated energy distribution shows the presence of secondary electrons between 0 and -7 V RPA grid voltage. The H^- ion energy distribution begins at 20 eV. The peak of the energy distribution corresponds to the largest slope on the integrated energy distribution for negative ions. Numerical smoothing the integrated energy distribution introduces broadening of the resulting energy distribution so it appears that a portion to the reflected ions have greater energy than the incident beam neutrals.

the integrated distribution and numerically differentiating the smoothed data. The integrated energy distributions were smoothed using a built-in function of the KaleidaGraph software [63]. The smoothing introduces a broadening of the final energy distribution but reduces random fluctuations. The differentiated distributions were inverted along the x- and y-axis to give the energy distributions. This inversion is required because the negative RPA grid potential corresponds to the negative ion energy along the x-axis and to make the relative intensity of the negative ions positive along the y-axis.

Angular distributions are a series of measurements of the negative ion current collected by the RPA at different angles above the surface. The RPA measured the current at a specific angle for a grid potential at 20% and then at 110% of the incident beam acceleration potential. The difference between the two measurements is the negative ion current from the surface at the chosen angle minus the contribution of negative ions and electrons with energies below 20% of the incident neutral beam energy. Less than 10% of the total negative current was removed by this low energy cut off. The measurement is repeated at different RPA angles to give the full angular distribution of negative ions scattering from the surface.

The RPA energy resolution is limited at low energies by the divergence of the ions from the primary axis. The RPA grid only affects the perpendicular component of the ion velocity, so ions that do not move perpendicular to the grids have less velocity towards the faraday cup and will be stopped by the grid at a lower potential. This low energy broadening was approximately 0.5% of the measured value. At high energies the energy resolution is limited by the penetration of the electric field into

the spaces between the wire grids [57]. The potential in the open space in the grid is less than what was set on the grid wires by the power supply. Ions of a lower energy can move through the grid where the potential is not so high. The high energy broadening was measured to be about 4% of the measured value.

4.2 University of Maryland College Park

The Denver beam facility is designed to gather detailed information about the energy and angular distributions of backscattered negative ions; it requires multiple measurements with different RPA positions and voltages and can only cover negative ions reflected into a small solid angle above the surface. The experiment at UMCP is designed to collect negative ions over a larger solid angle above the surface in a single measurement. The vacuum system, shown in Fig. 4.3, used for the experiment consists of two sections, the source section and the target section. The source section contains the ion source used to produce the neutral beam; the target section has the incident neutral particle detector, conversion surface, the negative ion lens and negative ion detector. A gate valve separates the two sections so each can be pumped with separate turbo-molecular vacuum pumps. The source section is connected to a Pfeiffer TPU 180HM turbo pump and operates in the 10^{-5} torr pressure range. The target section is connected to a Pfeiffer TPU 450H and is capable of reaching pressures in the low 10^{-7} torr range after pumping for 18 to 24 hours and can reach the high 10^{-8} torr range after pumping for several days. Ion gauges connected to each section monitor the pressures separately.

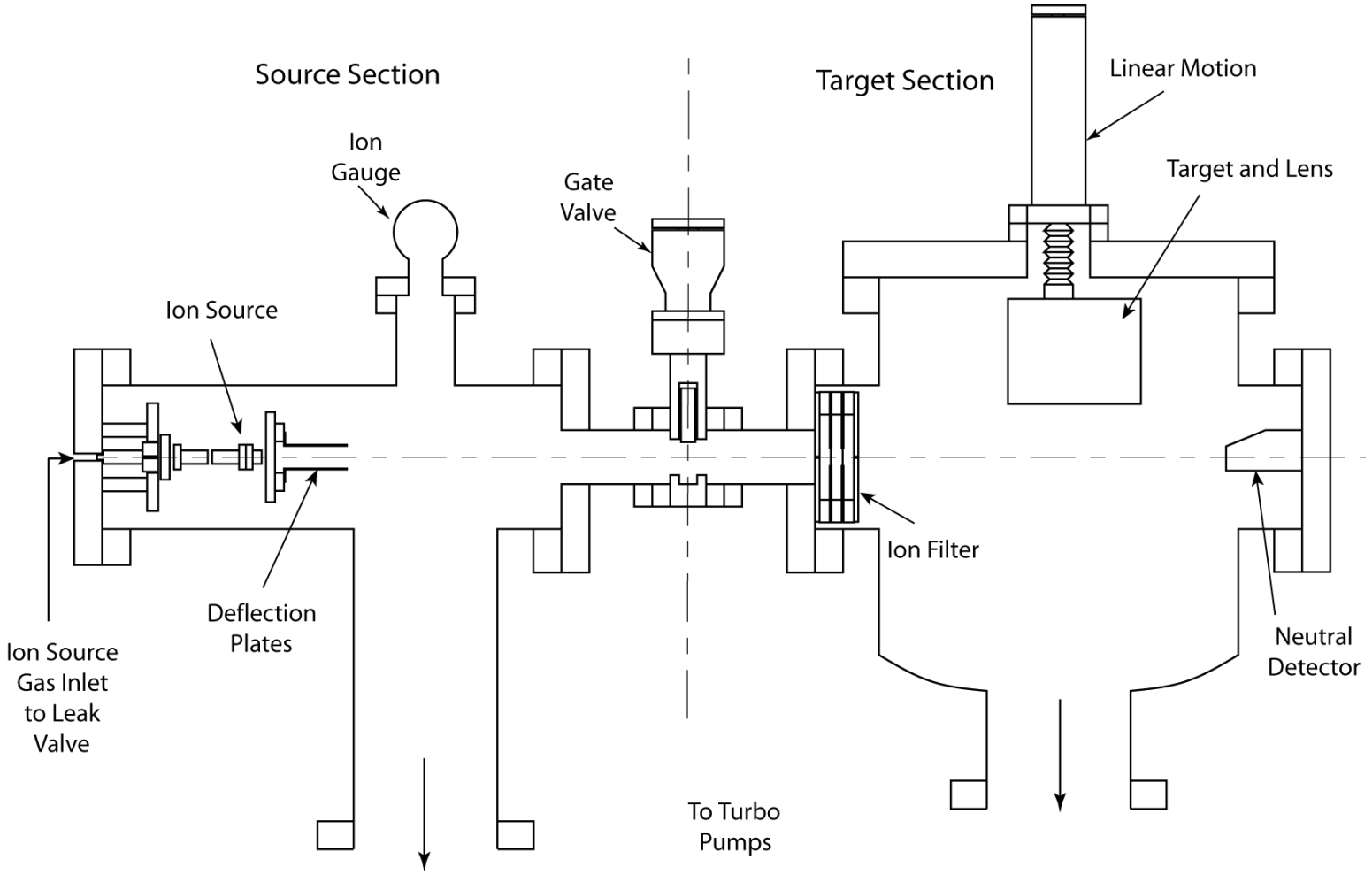

Figure 4.3: The essential components inside the vacuum chamber used for the University of Maryland measurements.

The ion source (Fig. 4.4) uses electron impact to create a beam of positive ions. Electrons are emitted from a hot tungsten filament located under the shield and next to openings in the collision chamber. The full voltage, V_{CC}, from the ion source power supply is placed on the collision chamber and the filament is biased 90V above V_{CC}. The voltages on the shield and filament accelerate the electrons into the collision chamber. Positive ions created in the chamber are accelerated through the extractor plate, which is set 1.4 mm in front of the collision chamber at a potential of one tenth of V_{CC}. Once accelerated through the extractor, the beam enters the lens. The lens is 1.8 mm away from the extractor and was set at ground. The lens is 10.2 cm long. The ion source is connected to the center of a 6 in. CF flange at the end of the T-shaped source section. The axis of the ion source is aligned with the axis of the tube. Gas enters the chamber through the a Granville-Phillips Co. Series 203 leak valve. The ion source gas also provides the neutral gas background in the chamber for charge exchange. A Sjuts Optotechnik model channel electron multiplier located opposite the ion source in the target section of the vacuum chamber measures the intensity of the beam from the source.

Neutral atoms and molecules are formed when ions in the beam undergo charge exchange collisions with the neutral background gas in the chamber. The high background pressure in the source section allows more charge exchange collisions to occur in the ion beam than low pressures, increasing the number of energetic neutrals. Charge exchange collisions occur with low momentum transfer so that the neutrals that are created continue to move in the same direction as the parent ion. The kinetic energy of the neutral atoms will depend on where the charge

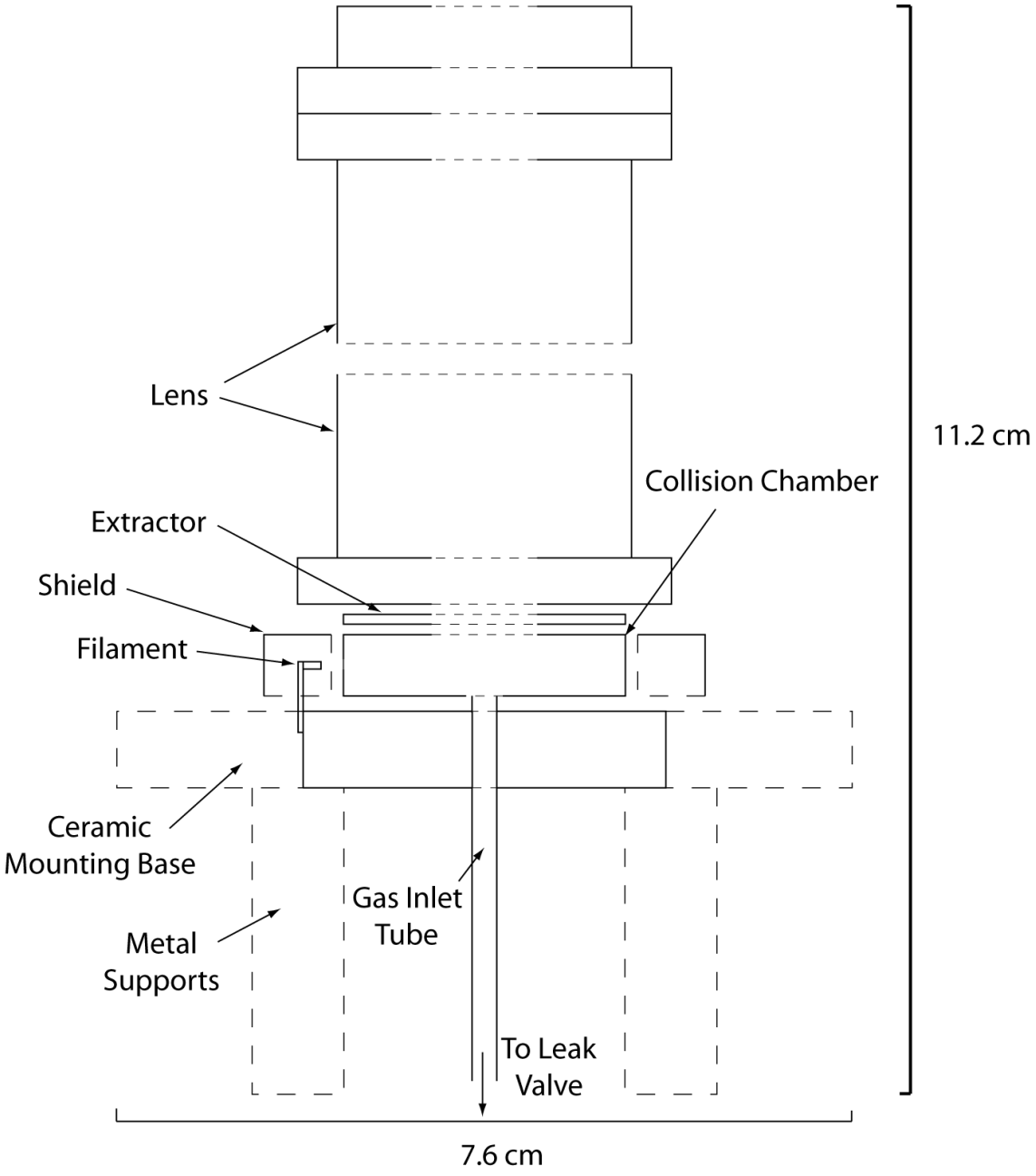

Figure 4.4: A schematic diagram of the ion source used in the vacuum chamber to produce the neutral beam.

exchange collisions take place in the ion source, this results in a spread of neutral atom energies. The maximum ion energy the source is capable of producing is set by V_{CC}. The cross section for charge exchange between H_2^+ and H_2 increases at ion energies below 500 eV, however the acceleration section of the ion source makes up a very small percentage of the total beam path [64]. The energy distribution of the neutral beam was estimated by assuming a high pressure in the collision chamber from the leak valve. The rest of the beam path is assumed to be at the chamber pressure, measured on the ion gauge. About 20% of the charge exchange collisions occur in the collision chamber after the neutral gas is first ionized. They have less than 15% of the final beam energy set by the ion source potential. Intermediate energy ions, from 15% to 85% of the maximum beam energy, are formed between the collision chamber and lens. These account for only about 4% of the neutral beam. The rest of the neutral beam, about 76%, is made up of particles with 85% to 99% of the maximum beam energy after being neutralized in the lens in front of the acceleration region.

The ion composition of the beam was evaluated using a Wien filter and pico-ammeter [65]. The Wien filter was connected to the front end of the ion source and the ion current measured as a function of the voltage on the electric field plates of the filter. There were four different peaks corresponding to H^+, H_2^+, H_3^+ and H_2O^+ for the range of voltages set on the filter. H_2^+ was the most abundant constituent of the ion beam at 86%. H_2O^+ makes up 8% of the beam and H^+ and H_3^+ each make up 3% of the ion composition.

Charge exchange between the background gas and 500 eV H_2^+ ions has a cross

section of 5×10^{-16} cm^2, and the cross section between H^+ and the background gas is 2×10^{-16} cm^2 at this energy [64]. The main component of the neutral beam, after the beam filters remove the ions, are then hydrogen molecules. The cross section for H_2 excitation in these collisions is 1.32×10^{-17} cm^2 for 500 eV ions, and decreases with decreasing ion energy [66]. A consideration of the charge exchange and excitation cross sections shows that at most 3% of the neutral hydrogen molecules in the beam will be excited and the remainder will be neutral hydrogen molecules in the ground state.

In this experiment we assume that hydrogen molecules dissociate at the test surfaces. Hydrogen molecules have a bond strength of 4.52 eV which is small compared to the beam energies used [67]. MgO surfaces have been tested for conversion efficiency using neutral hydrogen molecules in the incident beam instead of atoms [59]. Analysis of the reflected beam from the MgO surface showed no hydrogen molecules and there was no measured difference between the ion fractions resulting from the scattering of H_2^0, H_2^+ and H^+ beams. A total conversion efficiency measurement was done on a cesiated tungsten surface comparing H_2^+ and H^+ incident beams [54]. It was found that the total conversion efficiency per nucleon was the same within error, and it was concluded that the molecules dissociated at the surface and the incident particle state has no affect on the backscattered atoms. Assuming this, the angular and energy distributions of the atoms leaving the surface in the UMCP system should be comparable to those in the Denver system. Since the neutral beam is H_2 molecules and the converted ions are H^- atoms, the conversion efficiency in the UMCP system will appear to be twice as high because there are

twice the number of atoms scattering from the surface as molecules measured in the neutral beam. The beam energies are expressed using the total acceleration potential, so the equivalent energy of each atom is only half of the energy of the incident molecule.

The beam exiting the ion source is a mixture of ions and energetic neutral particles. There are two charged particle filters along the beam path to remove ions so only neutrals will reach the target surface or flange detector. The first filter is a set of electrostatic deflection plates located on the end of the ion source. The plates are arranged so that as the beam exits the ion source, the electric field produced by the voltage on the plates deflects the charged particles to the walls of the vacuum chamber. The deflection plate potentials were set to $\pm$ 25 V to deflect the ions. The deflection plates limit the charge exchange region to within the ion source.

The second filter consists of a set of three retarding potential grids covering the entrance to the target section of the chamber. The grids are made from a nickel mesh with a 90% transmission and cover the center hole in the three plates. The two outside grid plates are disk shaped and grounded to the vacuum chamber walls. The middle plate is cross shaped and electrically insulated from the mount and the other plates. The middle grid is biased with a positive voltage to repel positively charged particles that have not been removed by the deflection plates. The retarding grid fixture includes two plates with 0.3 mm holes that limit the size of the entrance to the target section, and reduce the beam diameter so it does not overfill the target surface. The first plate is positioned against the opening between the source chamber and target chamber and limits the gas exchange between the two

sections. The second plate is placed 3.3 cm away from the first plate. The maximum beam diameter is calculated using the size and distance between the apertures in the plates. The neutral beam diameter is about 4 mm at the target and 6 mm in diameter at the entrance of the flange detector.

A channel electron multiplier (CEM) is used to detect the neutral particles in the incident beam as well as the negative ions from the conversion surface. The detectors are Optotechnik Sjuts CEMs, model KBL 408. The front openings are 4 mm $\times$ 8 mm and the detector is 27 mm long. Single particle detection CEMs were chosen for the apparatus because of the predicted small ion fluxes from the target surface in the lens and ability to detect neutral particles in the beam. The neutral beam detector (referred to as the flange detector) is connected to the center of the 6 in. CF flange on the end of the target chamber facing the ion source. The flange detector measures the flux of neutral hydrogen molecules with energies less than 500 eV. CEMs lose detection efficiency as particle energy decreases [68]. The detection efficiency is measured between 4% and 50% for a beam of H_2^+ ions for energies between 100 eV and 500 eV. The CEM detector used for the converted negative ions (referred to as the lens detector) is connected to the ion lens explained below. The lens detector measures H^- ions that have been accelerated through the lens to at least 1 keV. CEM detection efficiencies for H^- ions at these energies have been measured to be around 90% and rise to about 94% for 3 keV and higher energy ions [69]. Both detectors are biased with the front end at ground and the back end at a positive voltage. The voltages across them ranged between 2 and 3 kV and were set so that the detectors gave similar pulse height distributions between surface

measurements, as measured on a multichannel analyzer.

The diagram of the circuit design used with the CEMs is shown in Fig. 4.5. The circuit is on a single glass-epoxy G10 board and connected by electrical feed-throughs to the electronics outside of the vacuum chamber. The output from the detector first goes to a Northern Scientific, Inc. model NS-314 pre-amplifier with a fixed gain of 6.5 V/C. The pre-amp output goes to an Ortec amplifier, model 451, with a gain set to 5.5. The output of the amplifier is sent to a Tennelec Single Channel Analyzer (SCA), model TC 450. To remove the low energy noise from the detector output the threshold of the SCA is set at 2V. The output of the SCA is a rectangular pulse 2 V high and 480 ns long that the Hewlett Packard 5326A timer-counter detects and counts.

The ion lens assembly guides negative ions from the target surface under test to the detector. The lens was designed using Scientific Instrument Services Inc. SIMION™ software. SIMION™ is an ion optics simulation program for modeling the trajectories of charged particles in electrostatic and magnetic potential arrays [70]. Fig. 4.6 is the top view of the ion lens as it is positioned in the vacuum chamber and shows the trajectory of 200 eV negative ions leaving the target surface at 5° with the lens elements at potentials that optimize collection by the detector. The surface is at a negative potential so that reflected negative ions are repelled into the lens. The lens consists of a series of plates with fins at different voltages that focus the negative ions into the detector. The voltages are derived from a voltage divider that uses a series of resistors connected between the lens plates and the high voltage source. The last two lens plates are without fins and grounded. The lens power supply was

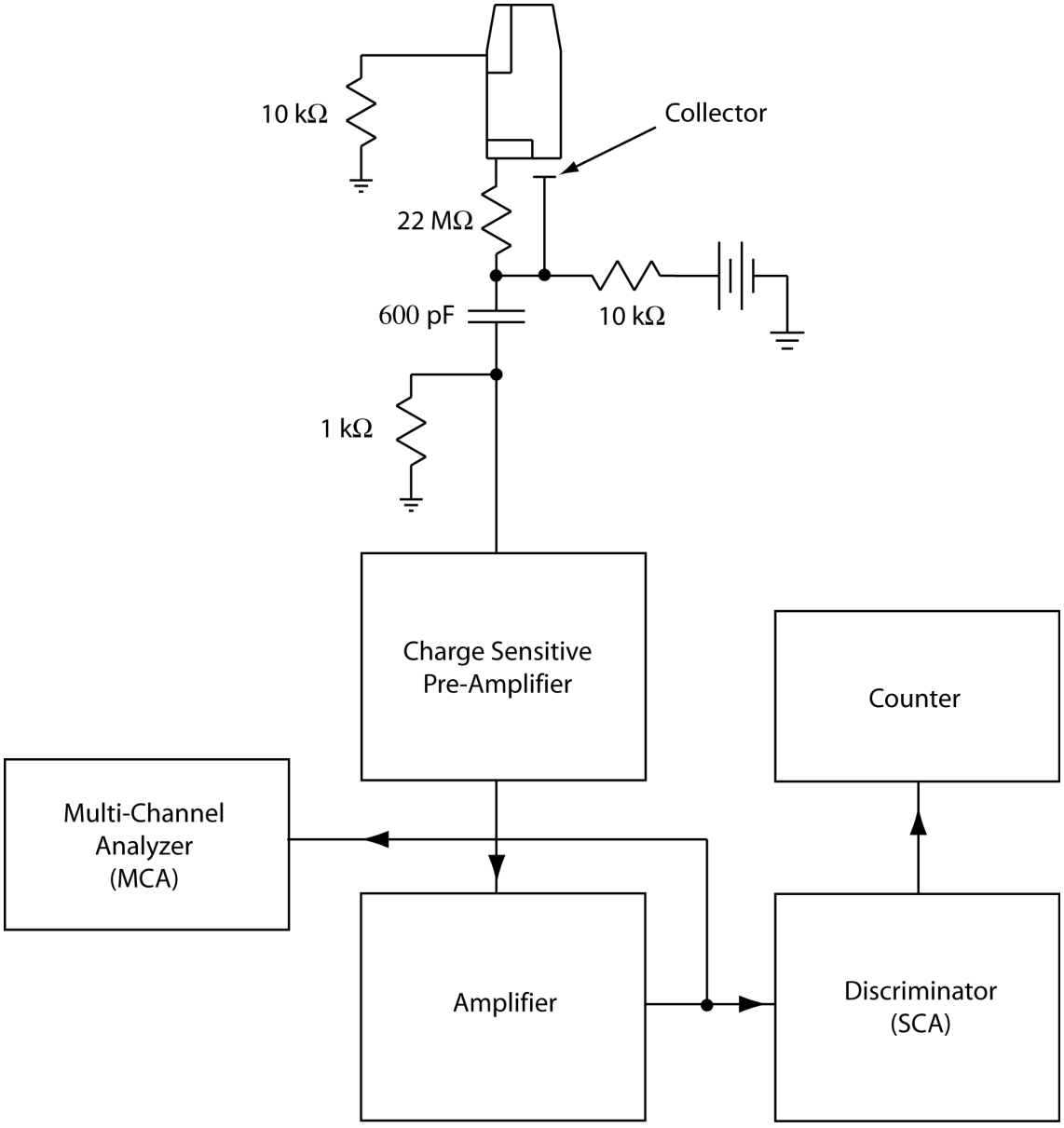

Figure 4.5: A schematic of the CEM circuitry and processing electronics used to count the number of neutral hydrogen molecules in the beam and the negative ions collected by the lens from the test surface.

set between -1 and -6 kV. The lens can also collect positive ions converted from the surface by changing the voltage polarity. The ion lens voltage used to properly focus the negative ions from the surface is dependent on the ion source acceleration voltage. The lens is held on the retractable arm of a linear feed-through on the top of the vacuum chamber. It can be raised and lowered to position the surface in the neutral beam path. When fully retracted the lens structure is completely out of the path of the neutral particle beam, exposing the flange detector to the neutral beam. The angle at which the neutral beam hits the target surface is controlled by the orientations of the 2.75 in. flange that the retractable arm is set on and the 12 in. flange that seals the top of the target chamber. The 2.75 in. flange can be rotated in approximately 60° increments and the 12 in. flange can be rotated in 11.25° increments. The flanges can be set so that the beam passes parallel to the target surface. The uncertainty in the incident beam angle is within 2°. Specifics of the ion lens components are discussed further in Appendix A, page 121.

The ranges of ion energies and exit angles that can be detected with the lens detector depends on the voltages on the lens elements. SIMION™ was used to determine ranges of angles and energies that an ion leaving the surface can have and reach the detector. These acceptance ranges were compared with SRIM calculations of the energies and angles of ions backscattered from a tungsten surface [14]. The estimated total fraction of all converted negative ions reaching the lens detector after leaving the surface is between 3% and 5% during a measurement. The total conversion efficiency, as measured by this system, is also dependent upon the detection efficiencies of the CEMs used to detect the incident beam flux compared to the

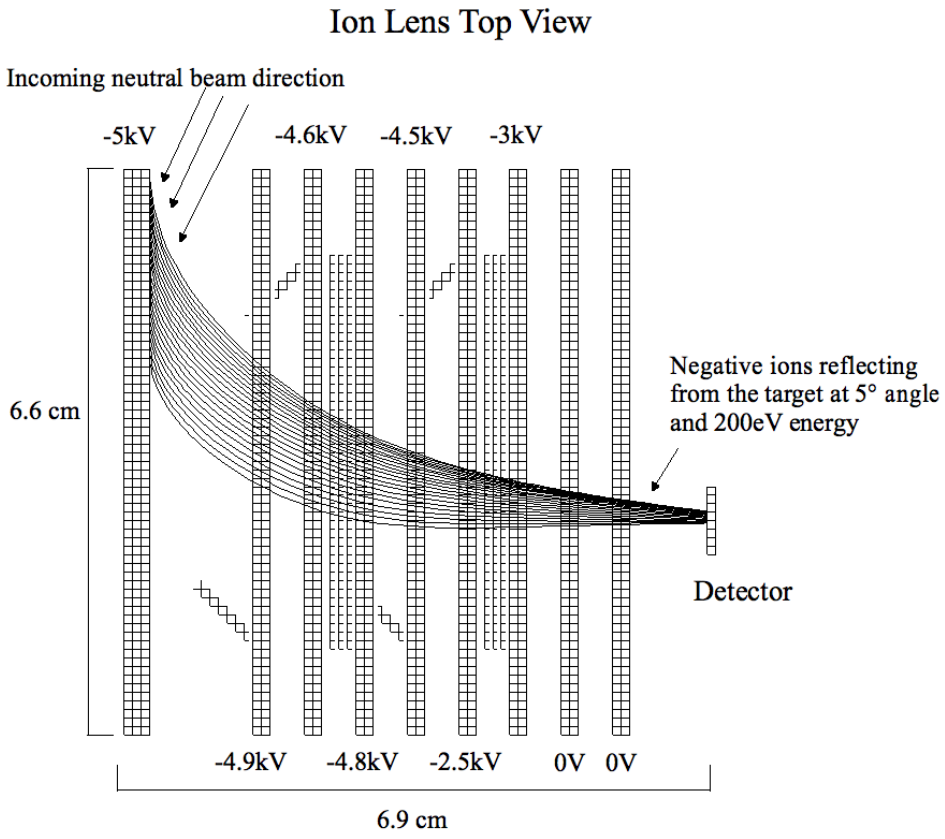

Figure 4.6: Schematic top view of the ion lens as displayed in SIMION™ showing some of the singly charged negative hydrogen ions leaving the target surface at an angle of 5° and an energy of 200 eV.

the one used to detect the negative ions from the surface.

Absolute measurements of conversion efficiency depends on a number of assumptions about the relative efficiencies of the two CEM detectors for different incident energies and charge states of the particles collected. Rather than attempt absolute measurements with experimental uncertainties associated with the fluxes and efficiencies, all measurements were made relative to the tungsten surface tested in the Denver apparatus. The detailed energy and angular distributions measured at Denver are used as guidelines for the distribution of backscattered atoms in the ion lens. It is assumed that the efficiencies of the various components of the system (ie. lens collection, efficiency of each CEM for the neutral beam and reflected negative ions) remain constant for similar operating parameters and the only difference will be due to the relative conversion efficiencies of the surfaces under the same conditions.

Equipment to heat the surface was also added to the lens system after initial data were taken. A tungsten heating coil (Kurt J. Lesker Co. part number EVSME14040W) was installed behind the target surface. The heater is set in a machinable ceramic glass mica holder facing the target and is not in direct contact with the target holder plates. A direct currents of up to 17A is put through the coil and surface temperatures have been observed to rise to above 138℃ as measured by temperature labels purchased from TIP Industries Inc. Heating the surface removes water and other adsorbates. The heating system is further discussed in Appendix A with the rest of the lens.

4.2.1 Operation

After introduction of the sample target surface, the target section of the vacuum chamber was allowed to pump down for over twelve hours before measurements were taken. The typical pressure in the target section, after that period is between 1.0 and 3.0×10^{-7} torr. Measurements begin by the application of the operating voltages to the ion source and beam filters and then opening the gate valve between the two chambers. H_2 gas is then introduced into the collision chamber of the ion source through the leak valve; this raises the overall pressure in the source section. By varying the ion source filament current and gas pressure the intensity of the neutral beam could be changed. During standard operation, the pressure in the source section of the chamber reaches into the 10^{-4} torr range while the target section remained below 1×10^{-6} torr.

The ion source is operated between 100 and 500 V. At voltages lower than 100 V the neutral flux is very low, at voltages above 500 V the lens plates must be set at voltages that cause discharges between them and flood the CEM detector with electrons. The voltages on the deflection plates and retarding grids were varied while the number of detected particles coming from the ion source was measured using the flange detector. In the initial tests of the ion filters, air was used as the gas fed into the ion source set at 1 kV and the initial beam intensity was adjusted to 8×10^4 counts per second. The retarding grid caused a sharp decline in the counts per second at about 1025 V. The count rate fell from 8×10^4 to 280 counts per second. The effect of the deflection plates on the beam can be seen when a ±1 V

potential is used. For the deflection plates, the count rate levels off after about ±5 V are applied. The pressure around the ion source was varied by changing the gas flow into the source section of the chamber through the leak valve while observing the count rate as a function of the deflection plate voltage (Fig. 4.7). The results show that the number of neutrals can be increased by allowing more gas in to the vacuum chamber. More gas increases the pressure in the collision chamber which will produce more ions from the ion source. The added gas also increases the number of neutral background particles along the beam path, increasing the probability of charge exchanges.

During surface tests with the hydrogen beam, the nominal neutral beam count rate was approximately 2000 counts per second at the flange detector. Conversion efficiency measurements were taken using incident neutral beam intensities between 1000 and 3000 counts per second to examine the effect of incident flux on the conversion efficiency. No effect on the conversion efficiency measurement was found over this range of incident neutral beam intensities. The pulse height distribution of the flange detector after the neutral beam is turned on is recorded with a multi-channel analyzer (MCA). The MCA is a Tennelec PCA3 multichannel card controlled by Oxford WIN-MCA software. Pulse height distributions are measured before and during the experiment and the results are compared to a base set of measured distributions for the lens and flange detectors (Fig. 4.8). The response of a CEM can change with age and use resulting in a shift of the peak of the pulse height distribution and change the number of counts at the output of the SCA. The voltage on the CEM is adjusted until the measured pulse height distribution is comparable to

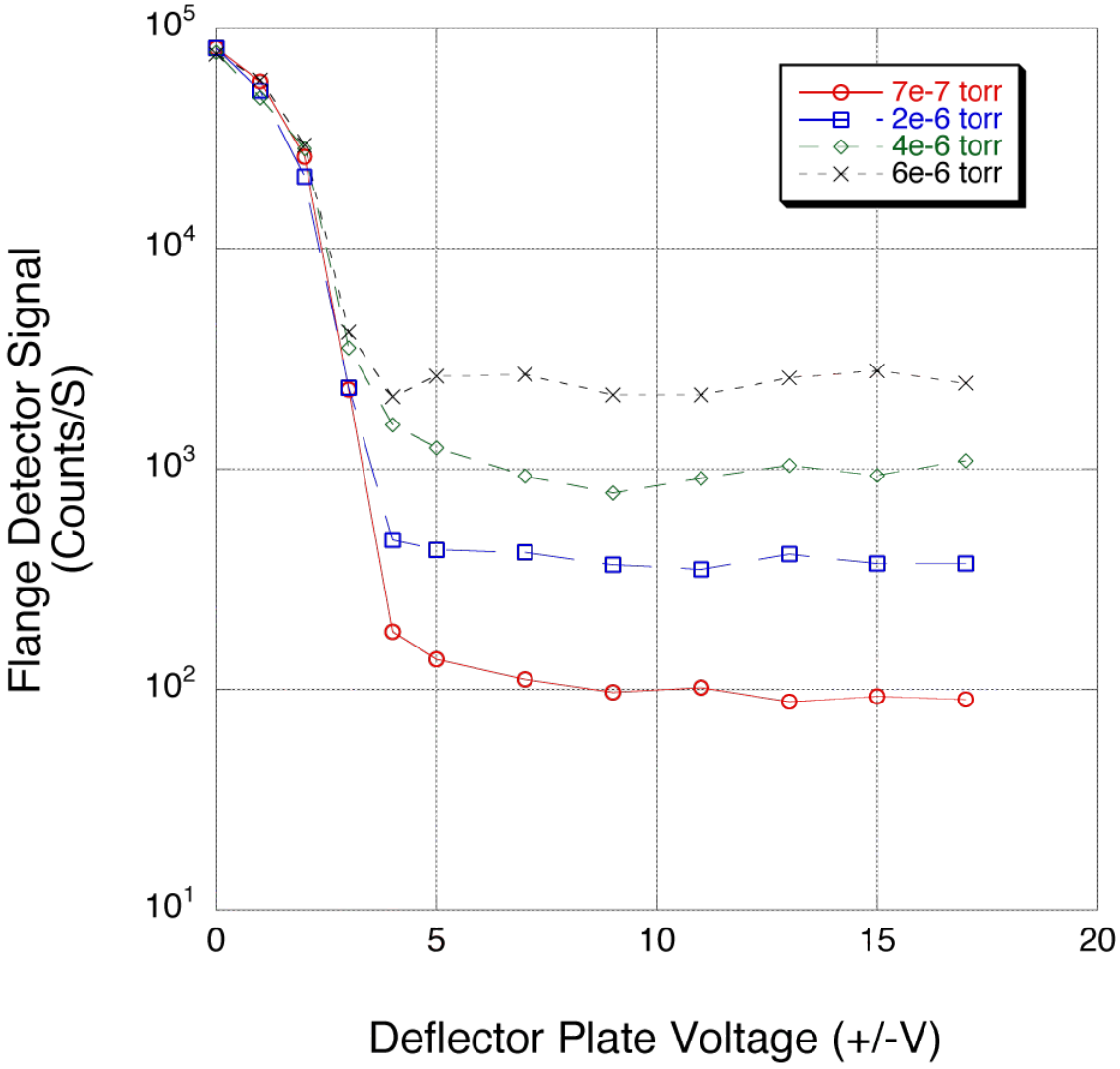

Figure 4.7: Flange detector count rate as a function of deflection plate voltage for different pressures in the source section of the vacuum chamber. The ion source produces 1 keV ions. The pressure in the ions source collision chamber is varied with the leak valve. Ions are removed from the particle beam above 5 V on the deflection plates and the count rate is no longer affected. The counts at deflection voltages above 5 V are energetic neutral particles. The raised pressure causes more charge exchange collisions, increasing the neutral signal to the detector.

the reference distribution. The pulse height distributions for the neutral and lens detector usually change only after the detectors have been subjected to atmospheric pressure for a few days.

When the lens is first placed in the beam path it is necessary to determine the voltages to use on the target and lens plates. The count rate recorded by the detector is observed while the lens voltages are changed until a maximum is found in the counts. The number of counts from the lens detector is also measured with no incident beam to ensure no discharges are occurring and contributing to the background count rate. Counts from the lens detector are recorded for 10 seconds. The number of counts is measured with the lens voltage off and the neutral beam incident on the surface to determine the number of particles reaching the detector from backscattered particles reflected from the lens elements rather than charge exchange. Typical values of this background signal vary with the neutral beam intensity and are usually between 1 and 4 counts per 10 seconds for a 2000 count per second incident neutral beam. The pulse height distribution for the lens detector is measured during the surface measurement. The typically low particle flux to the lens detector requires longer observation times than for the flange detector. The background count rates are recorded to be later removed from the measured data.

The count rate is recorded with the lens voltage set after the background counts have been measured and the neutral beam is directed to the conversion surface. Ten 10 second readings are successively taken from the lens detector and averaged. The lens is then raised from the beam path and the full flux of the neutral beam is measured with the flange detector. Ten 1 second successive readings are taken for

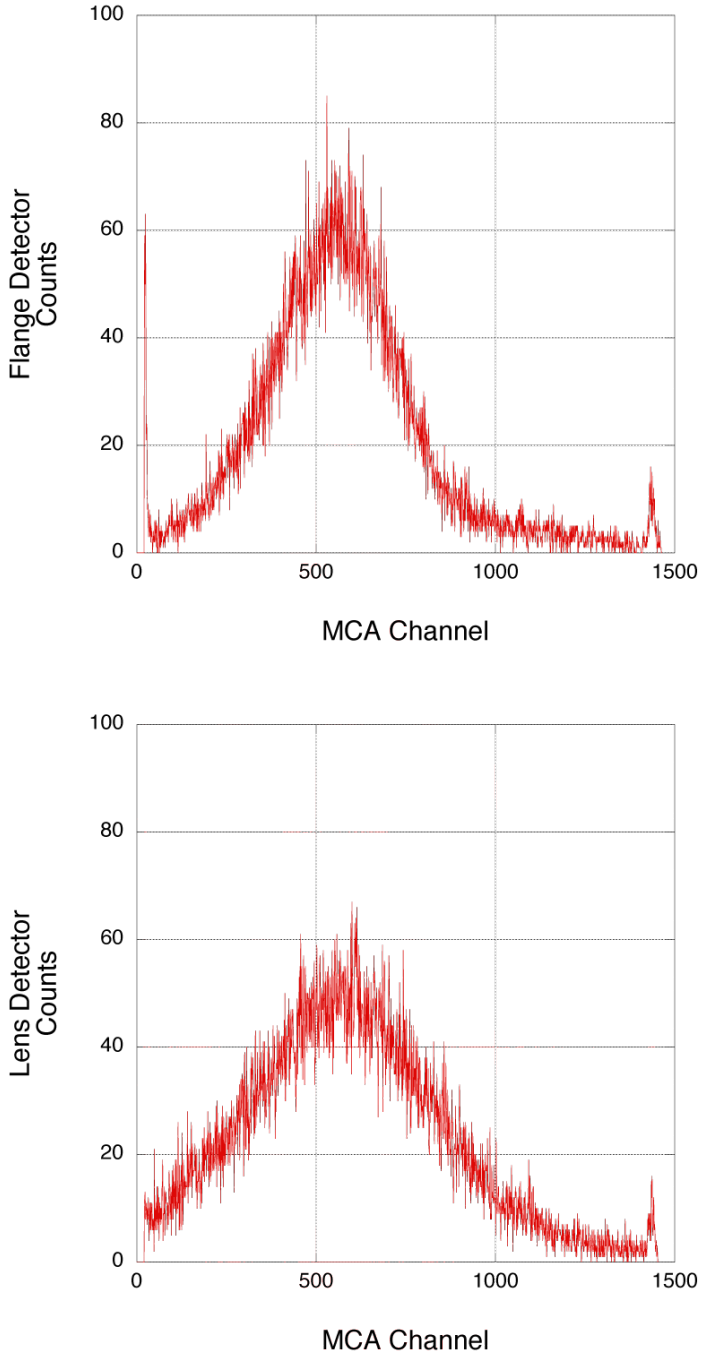

Figure 4.8: Reference pulse height distributions used to set the voltage on the CEMs for the flange detector set to 2.7 kV (top) and lens detector set to 2.45 kV (bottom). The pulse height distributions were independent of incident beam energy. Low channel noise occurs on the flange detector pulse height distribution below channel 26. High channel noise starts above channel 1425 for both detectors.

the neutral beam flux and averaged. The measurement cycle is repeated three times at each neutral beam energy to take into account changes in neutral beam intensity. Sudden changes in the neutral beam intensity are rare and data for the lens or flange detector count rates that fluctuate by more than 30% are repeated.

Once data have been collected at a given incident energy, the ion source acceleration voltage is changed and the lens voltage is reset again for the new measurement. For the surfaces tested, the positive ion counts were much lower than the negative ion counts. A positive to negative ion ratio of about 1:8 was the largest observed for the surfaces tested. Because of the low count rates, the conversion efficiency for positive ions was not investigated for the surfaces beyond the initial test.

Measurements for heated surfaces are made after the room temperature measurements. A direct current is sent through the heater coil for at least an hour to allow the surface to attain temperature equilibrium. At heater currents above 17 A, the lens detector begins to record a large background count rate when the lens voltage is applied. Accurate data cannot be taken under these conditions so the heater current is not set above 17 A. For lens voltages above 3 kV, background counts increase when the sample is heated. The voltage required to collect backscattered negative ions from 400 eV and 500 eV incident beam energies causes background counts larger than the signal and meaningful data could not be collected. Only incident beam energies equal to or below 200 eV were measured for heated samples. The measurement procedure for the heated surface is the same as for the room temperature ones.

4.3 Conversion Surfaces

As discussed in Chapter 2, work function is one of the properties that determines the conversion efficiency of a surface. Low work function surfaces are more efficient for surface conversion but are also relatively reactive and difficult to keep uncontaminated. The surfaces tested in this work have relatively high work functions compared to cesiated tungsten. The work functions of seven of the tested surfaces were measured to test the relationship between relative conversion efficiency and work function. Work function data were collected on these surfaces at two different facilities with two different pieces of equipment, an X-ray photoelectron spectrometer (XPS) at the X-ray Photoelectron Spectroscopy facility at UMCP and a Kelvin Probe in the Materials Engineering Branch at NASA Goddard Space Flight Center.

The XPS facility uses a Kratos AXIS 165 spectrometer equipped with a 165 mm radius spherical analyzer and an eight channeltron detection system to measure photoelectron energy. X-ray photons are generated from either an Al or dual Al/Mg anodes. The temperature of the sample stage can be varied between -120℃ and 475℃ and includes a charge neutralization system for insulating surfaces. The unique binding energies of the elements and the limited depth into the surface from which photoelectrons are emitted allow the system to identify the composition of adsorbates on the top layer of the surface. The intensity of photoelectrons as a function of binding energy is recorded to produce a surface photoelectron spectrum.

The Kelvin Probe model KP7000 made by McAllister Technical Service is contained in a small vacuum chamber. The probe tip is made from stainless steel

and the samples are mounted on a removable copper stage. The samples were tested at pressures from 5.6×10^{-7} to 5.6×10^{-10} torr. The Kelvin probe is a non-invasive technique that measures the contact potential difference (CPD) between two conductors. The sample and probe tip are set close together to form a capacitor. The probe works by connecting the probe tip and sample by a backing voltage and measuring the current between the two. When the current is zero, the backing voltage is the same as the CPD between the tip and sample. Vibrating the tip above the sample surface is used to reduce noise and increase accuracy of the measurement. The work function of the material being probed can be found by subtracting the CPD from the work function of the probe tip.

4.3.1 Surfaces

4.3.1.1 Tungsten

Amorphous tungsten surfaces were studied in the experiment. The surface and its preparation were similar to the one used in the IMAGE mission. These surfaces were polished at NASA Goddard Space Flight Center and the surface smoothness was measured with an atomic force microscope. The after polishing, the surface consisted of smooth areas and pits (Fig. 4.9). The RMS roughness of the surface was measured to be 2.5 nm. The measured work function of the surface from the XPS data was 4.5 eV. The work function of the tungsten sample measured by the Kelvin probe was 4.26 eV. The conversion efficiency of this surface was tested at Denver and at UMCP and served as a transfer standard.

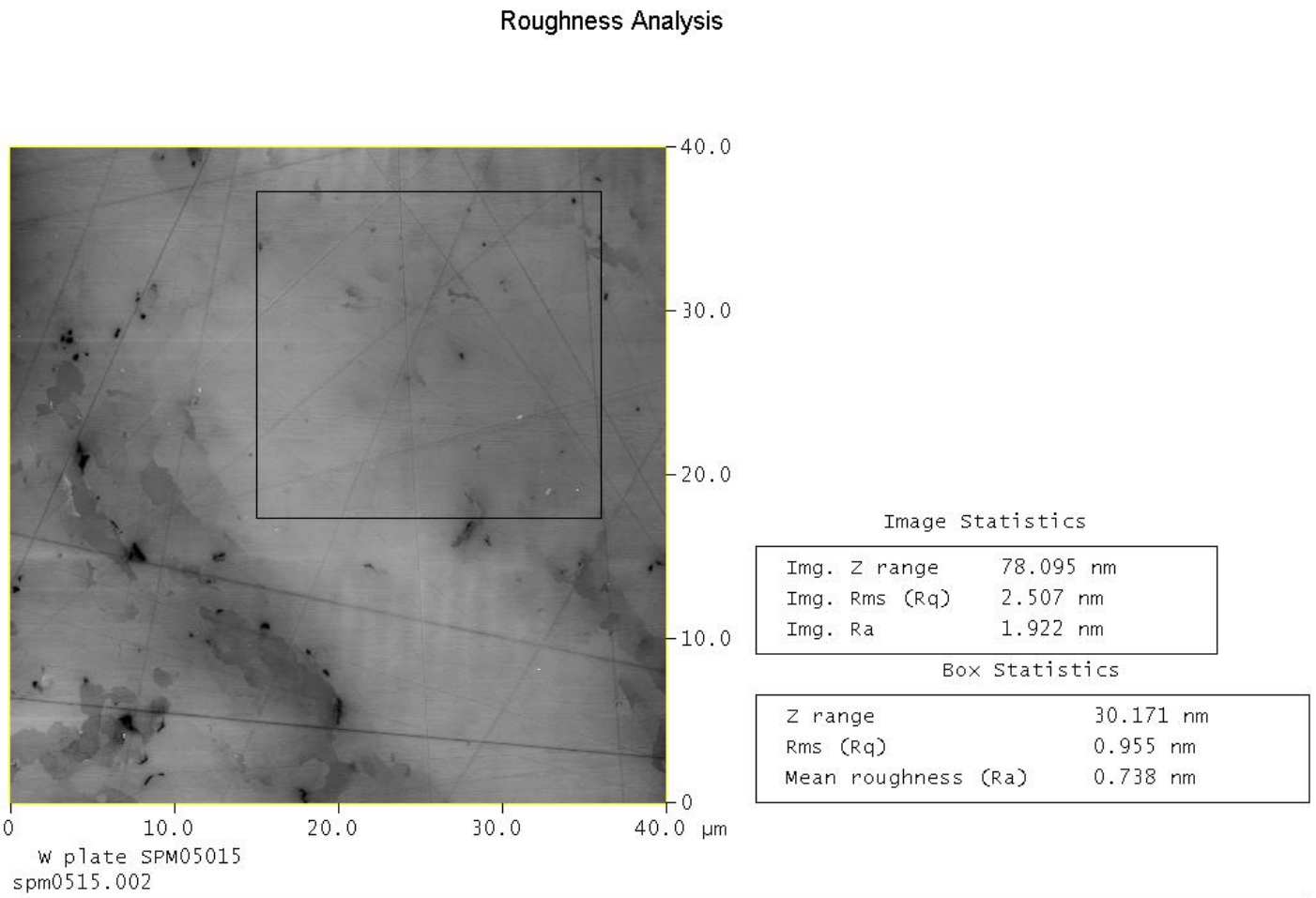

Figure 4.9: An atomic force microscope image of the polished tungsten surface. The surface contains a smooth area covered with pits.

4.3.1.2 Diamond Like Carbon

A diamond-like carbon (DLC) surface was received from NASA for testing. The surface is a polished silicon substrate covered with tetrahedral amorphous carbon using chemical vapor deposition. The silicon substrate has an RMS roughness of about 0.06 nm and the DLC surface had an RMS roughness around 0.8 nm after deposition [71]. The work function measured from XPS data was 4.6 eV. The sample was a candidate for the LENA detector in the IBEX mission. This surface was also tested at the University of Denver but less extensively than the tungsten surface.

4.3.1.3 Silicon

The 2 cm silicon disk surface (Si n-type) used in the experiment were purchased from Virginia Semiconductor, Inc. The crystal orientation to the surface is 110 $\pm 0.5^{\circ}$ from the surface, and it was doped with phosphorus (n-type). The piece was polished on both sides and has an electrical conductivity of <1 S/cm. A second silicon sample (Si p-type), cut into squares, was used to deposit gold and silver films, was also tested. The surface orientation was also 110 and it had an unspecified p-type dopant, most likely boron. The silicon samples were not measured for roughness but both were polished by the manufacturer to a mirror finish.

4.3.1.4 Graphite

Highly ordered pyrolytic graphite (HOPG) was tested in the system. The materials were purchased from Structure Probe, Inc. (SPI) and was labeled as SPI-1 and SPI-2. The surface was not polished but, due to the layered structure, is easily cleaved leaving a clean and close to atomically flat surface. The SPI-1 grade provides the smoother surface after cleaving and is higher purity than the SPI-2 grade. The SPI-1 sample has a measured work function of 4.9 eV using XPS data. Due to the layered structure, it is possible to achieve close to atomically flat surfaces and this grade has a reported mosaic spread as low as $0.4^\circ \pm 0.1^\circ$ from x-ray diffraction measurements made by the manufacturer. Mosaic spread is the FWHM in the x-ray rocking curve and a perfect crystalline structure would have a mosaic spread of 0° [72]. During the experiment, it was observed that the two grades gave similar results so only the SPI-1 sample was tested in detail. The samples were cleaved in air before being tested in the system because preliminary data showed a slight improvement in efficiency for the cleaved surface.

4.3.1.5 Gold

A gold surface was made using evaporation techniques on a 1 cm^2 silicon wafer in the FabLab of the Maryland Nanocenter at UMCP. The metal was deposited over a 20 nm layer of chromium on the silicon to avoid flaking. The metal layer thickness was between 200 and 300 nm. XPS spectra for the surface at room temperature showed that 10 to 20% of the surface composition was a combination of oxygen and

carbon adsorbates. Heating the surface to 110℃ for 5 minutes effectively removed the carbon and oxygen. The Kelvin Probe measurement of the gold surface gave a work function value of 4.08 eV at room temperature and 4.19 eV when heated to 70℃.

4.3.1.6 Silver

The silver surface was also made in the FabLab on a 1 cm^2 silicon wafer. The metal was evaporated directly on the substrate to a thickness between 200 and 300 nm. The XPS scan of the surface composition at room temperature also showed oxygen and carbon contamination between 10 and 20%. After heating to 130℃ for 5 minutes, contamination was no longer detected. The work function of the surface was 4.2 eV at room temperature and 4.1 eV while heated at 70℃ in the XPS. The Kelvin Probe measured a work function of 4.13 eV for the surface at room temperature.

4.3.1.7 Platinum

The platinum surface was made in the FabLab. The metal was evaporated to a silicon wafer over 20 nm of chromium to ensure adhesion and avoid flaking. The platinum thickness was 200 to 300 nm.

4.3.1.8 CEM Lead Glass

The Optotechnik Sjuts surface consisted of a lead glass with high secondary electron emitting properties deposited over a ceramic disk 1.8 cm in diameter. This is the same material inside the Sjuts CEM detectors used in the experiment. The work function measured for the sample in the XPS facility was 5.2 eV.

4.3.1.9 Carbon NanoTubes

A carbon nanotube (CNT) surface was provided by NASA for testing. It was made of CNTs grown on a treated surface. The nanotubes were made by chemical vapor deposition using ethylene gas over a 10 nm underlayer of aluminum and a 10 nm catalyst layer of iron. An SEM scan of the surface is shown in Fig. 4.10. The nanotubes grow in a tangled structure that resembles steel wool when magnified. Some nanotubes stick up above the tangled mesh, resulting in small points that give rise to a high local electric field when a potential is set on the surface [73, 74]. A negatively charged CNT surface produces field emission from these points and a positively charged surface can strip atoms of their electrons around the points [75]. It was anticipated that the high electric fields produced at the points would provide electrons for neutral atoms to become negative ions.

4.3.1.10 Carbon Nanosheet

The carbon nanosheet (CNS) surface was grown on a silicon substrate by the Department of Applied Science at the College of Mary and William. The nanosheet

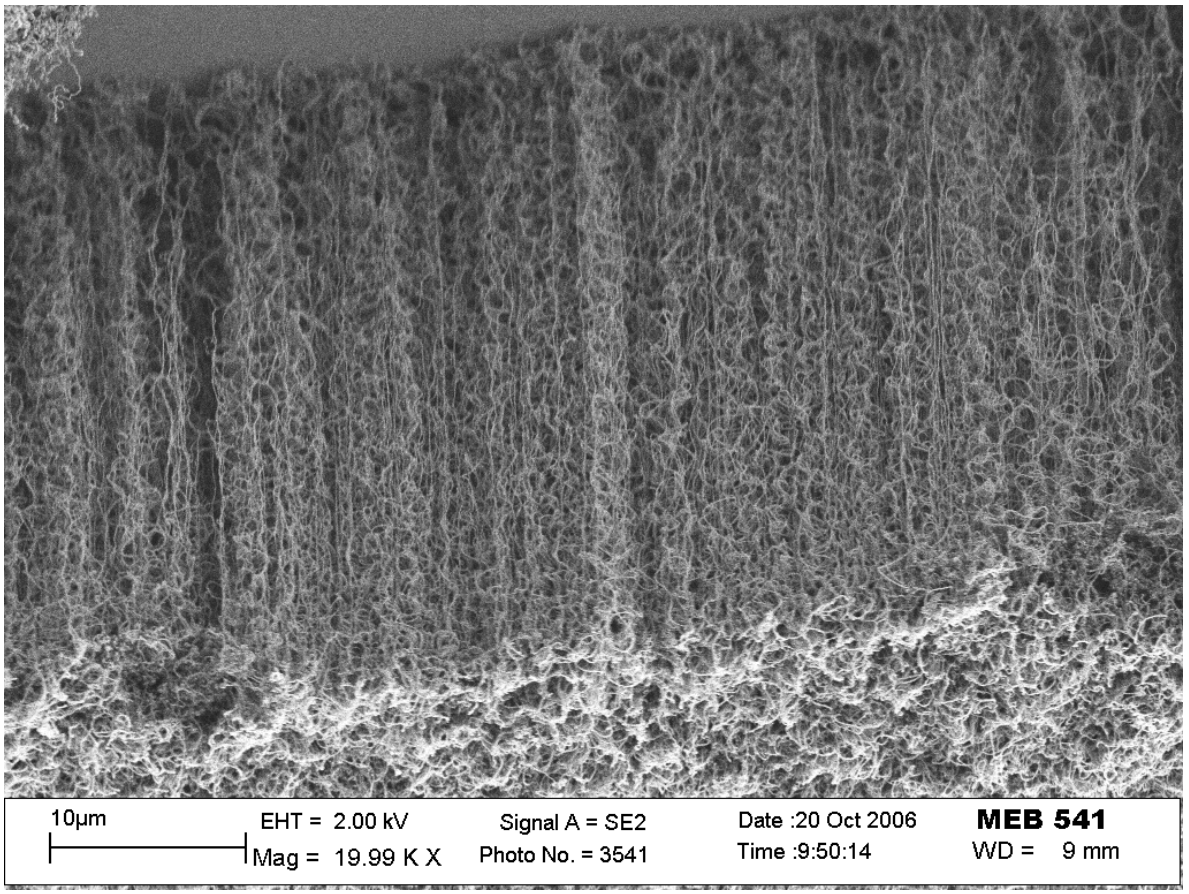

Figure 4.10: SEM image of the edge of the CNT surface. The substrate upon which the nanotubes are grown is at the top of the figure. The surface that the neutral beam is incident on appears at the bottom of the figure. This exposed surface is a nonuniform mesh of nanotubes.

is an ultrathin two dimensional graphene structure and is fabricated using inductively coupled radio-frequency plasma enhanced chemical vapor deposition [76]. The growth method uses methane as the carbon source in an H_2 atmosphere and does not require any special pretreatment of the substrate or a catalyst [77]. The nanosheet layers are oriented approximately vertical on the substrate surface and are about 1 nm thick. A 10 μm $\times$10 μm atomic force microscope (AFM) image of the carbon nanosheet surface is shown in Fig. 4.11. The sheets rise about 2 μm above the substrate and are thin but wrinkled. The wrinkles give an apparent thickness in the AFM image of about 1 μm.

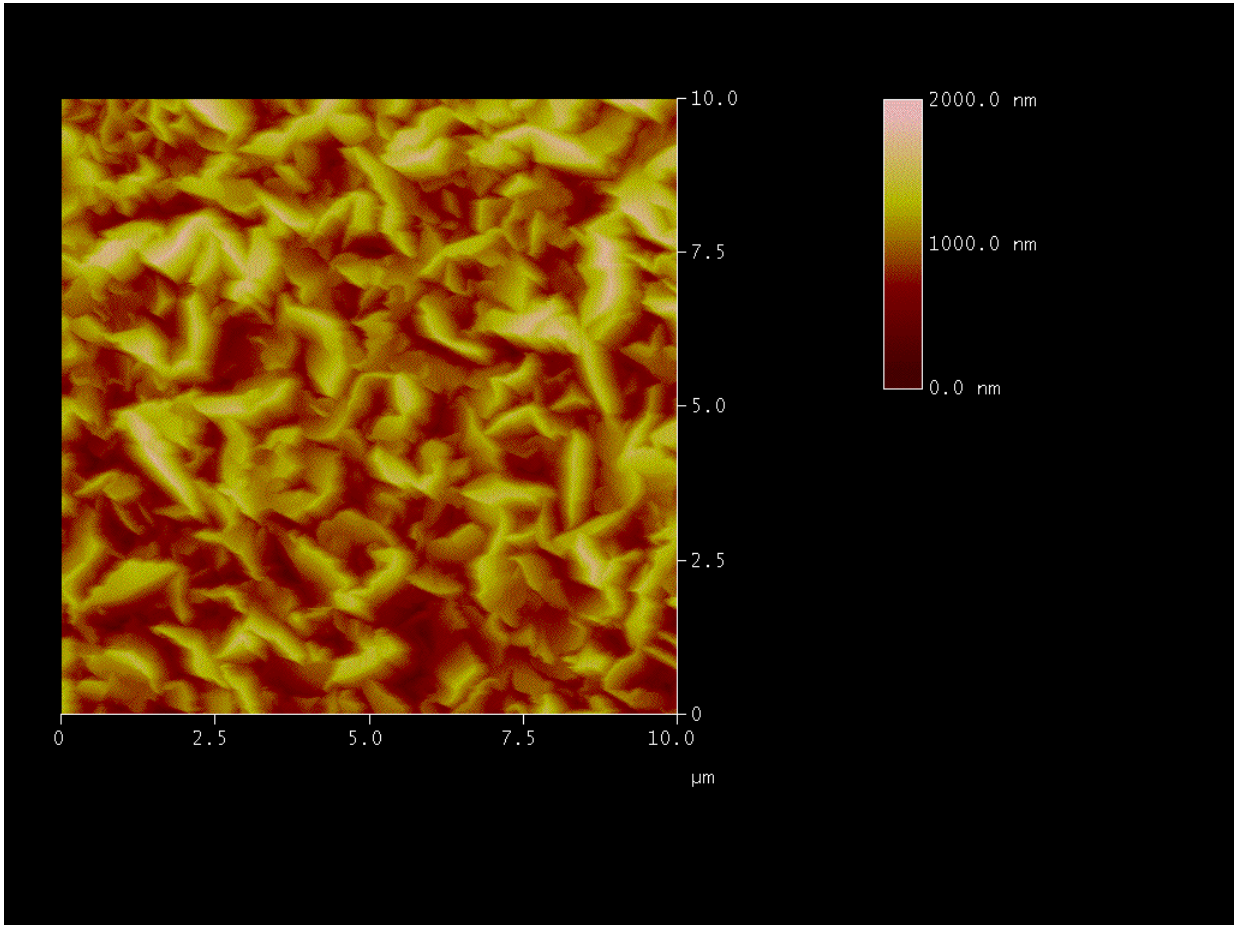

Figure 4.11: AFM image of the carbon nanosheet surface.

	Work Function (eV)		
Surface	**XPS**	**KP**	**Lit.**[78]
Tungsten	4.5	4.26	4.55
DLC	4.6	-	-
HOPG SPI 1	4.9	4.5[a]	5[b]
Si n-type	4.8	-	-
Gold	-	4.1	5.1
Silver	4.2	4.13	4.26
Platinum	-	-	5.64
Sjuts Lead Glass	5.2	-	-

Table 4.1: Work function data for the test surfaces. Differences in the work function measurements for the same surface are due to adsorbates and differences in measurement technique. The work functions only cover a range of about 1 eV.

[a] Graphite

[b] Carbon

Chapter 5

Data and Discussion

Data from both the Denver experiment and University of Maryland experiment are presented in this section. Unless otherwise noted, the samples were tested at room temperature, nominally 21℃. The angle of the incident beam with respect to a surface is defined differently depending on the application. All angle measurements are taken in the plane perpendicular to the surface containing the beam direction. The angle is measured from the surface plane to the incident beam so grazing angles have small values and a 90° incident angle refers to a beam perpendicular to the surface being tested. Reflection angles are measured from the scattered direction to the scattering plane. For example, specular reflection for a beam coming in at 10° with respect to the surface, both the incident and reflected angles are labeled as 10°.

5.1 Detailed Measurements

Two polished tungsten surfaces, labeled A and B, and the DLC surface were tested in the University of Denver neutral beam facility. The tungsten surfaces were cut from the same sheet and polished to the same smoothness. Tungsten surface A was tested using more incident beam angles and energies than surface B. For the same incident beam energies and angles the data are similar for the two samples so the data are combined without distinction. The Denver facility generates a beam

of mono-energetic neutral hydrogen atoms in the ground state. The surfaces were exposed to H-atoms at beam energies from 20 to 925 eV at incident beam angles of 6°, 10°, 15° and 20°. The data are collected by the RPA and ion repeller and are discussed on page 38. The raw data were current from the surface measured by the RPA as a function of RPA grid potential. The current passing through the RPA faraday cup (I_{fc}) is normalized to the neutral beam current (I_0) to account for fluctuations in the incident beam. From these data energy distributions of H^- ions at different reflection angles from the surface and angular distributions of H^- ions reflected in the plane perpendicular to the surface were derived.

Integrated energy distributions (Fig. 5.1) are directly measured with the RPA by taking current measurements for a series of different voltage settings on the RPA grid at one observation angle. The energy distributions were measured at angles about the specular reflection angle. As the voltage on the RPA grid was increased low energy negative ions and low energy secondary electrons were removed from the current measured in the RPA (Fig. 5.14). Energy distributions are obtained by numerically smoothing the measured integral distributions and then numerically differentiating. Smoothing generally caused a broadening of the data along the voltage axis, but attenuated spikes in the data due to small fluctuations in the raw integral energy distributions. Differentiating the raw data results in a distribution peaked around the most abundant reflected energy of the H^- ions.

Angular distributions are made by measuring the negative ion current from the surface at two different RPA grid potentials. The first grid potential was set to remove negative particles with less than 20% of the incident beam energy to

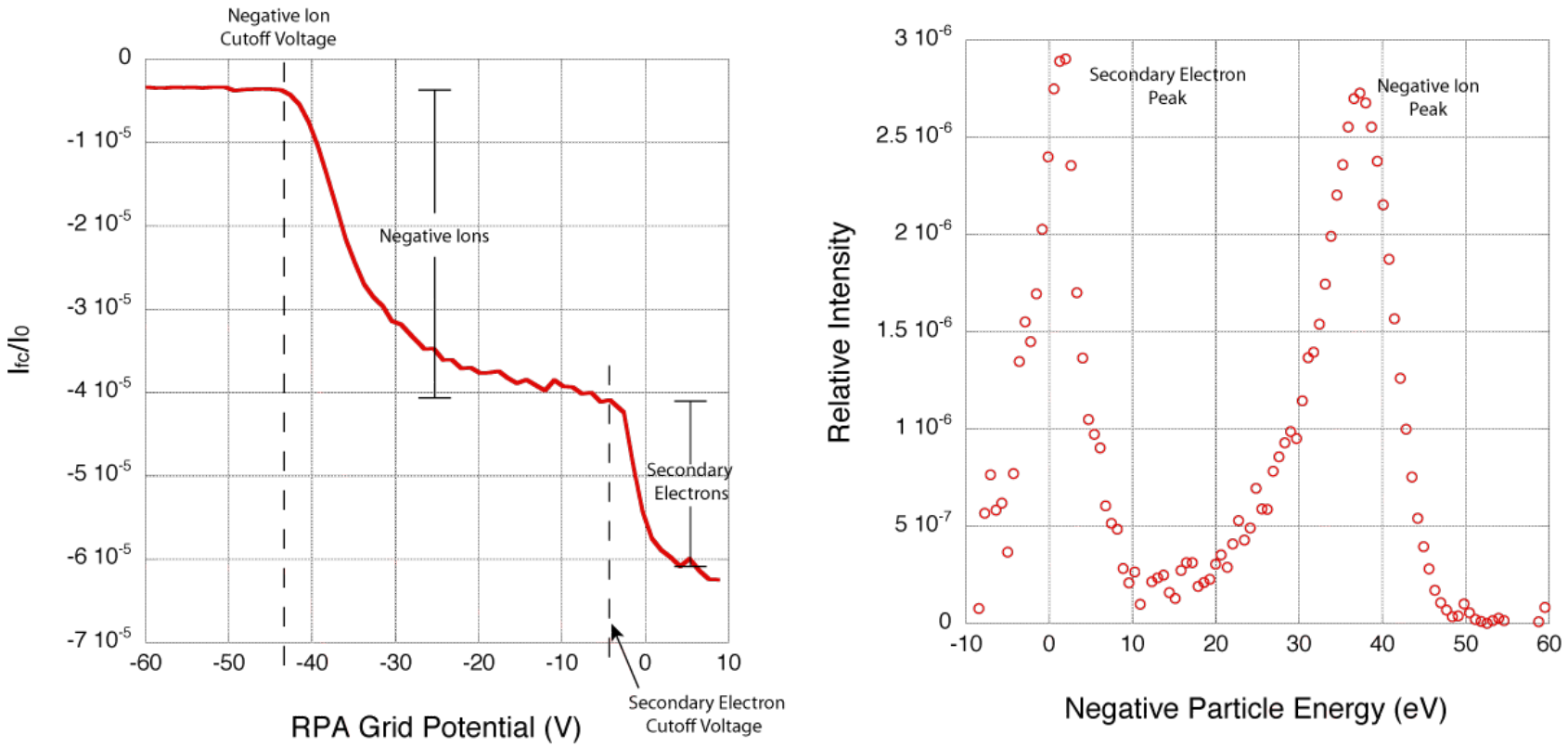

Figure 5.1: Integral energy distribution (left) and energy distribution (right) for a 50 eV and 10° incident neutral H atom beam reflected at 10° from a tungsten surface. The integral energy distribution shows the RPA grid voltages where the secondary electrons current (Secondary Electron Cutoff Voltage) and H^- ions current (Negative Ion Cutoff Voltage) are removed from the measured current by the grid potential. The energy distribution shows the amplitude and energy width of the secondary secondary electron and negative ions.

eliminate secondary electrons and the second potential was set to remove negative particles with less than 110% of the incident beam so that the difference between the RPA current is the only total H^- ion current reflected from the surface minus the low energy contribution that cannot be discerned from the secondary electrons. These measurements are taken over a large number of angles around the specular reflection angle of the incident beam. The angular distributions show the intensity of negative ions as a function of the RPA angle to the surface.

5.1.1 Tungsten Surfaces

Energy distributions for the tungsten surfaces are shown on pages 74 to 85. At incident H beam energies above 20 eV there is a characteristic low energy negative particle peak on the energy distributions attributed to secondary electron emission from the surface. The secondary electrons represented no more than 20% of the incident beam energy and are clearly distinguished from the higher energy H^- ions (see Fig. 5.1). This energy range is not shown for the energy distributions. The energy distributions are asymmetric, with a steeper rise on the high energy side than on the low energy side. At angles greater than specular the low energy tails are more pronounced than the low energy tails at angles less than specular.

The relative heights of the reflected negative ion energy peaks vary with reflection angle. As the reflection angle increases above specular reflection, the energy distribution peak becomes lower. The negative ion energy is lowered by collisions in the surface. The energy distributions show that negative ions that undergo fewer

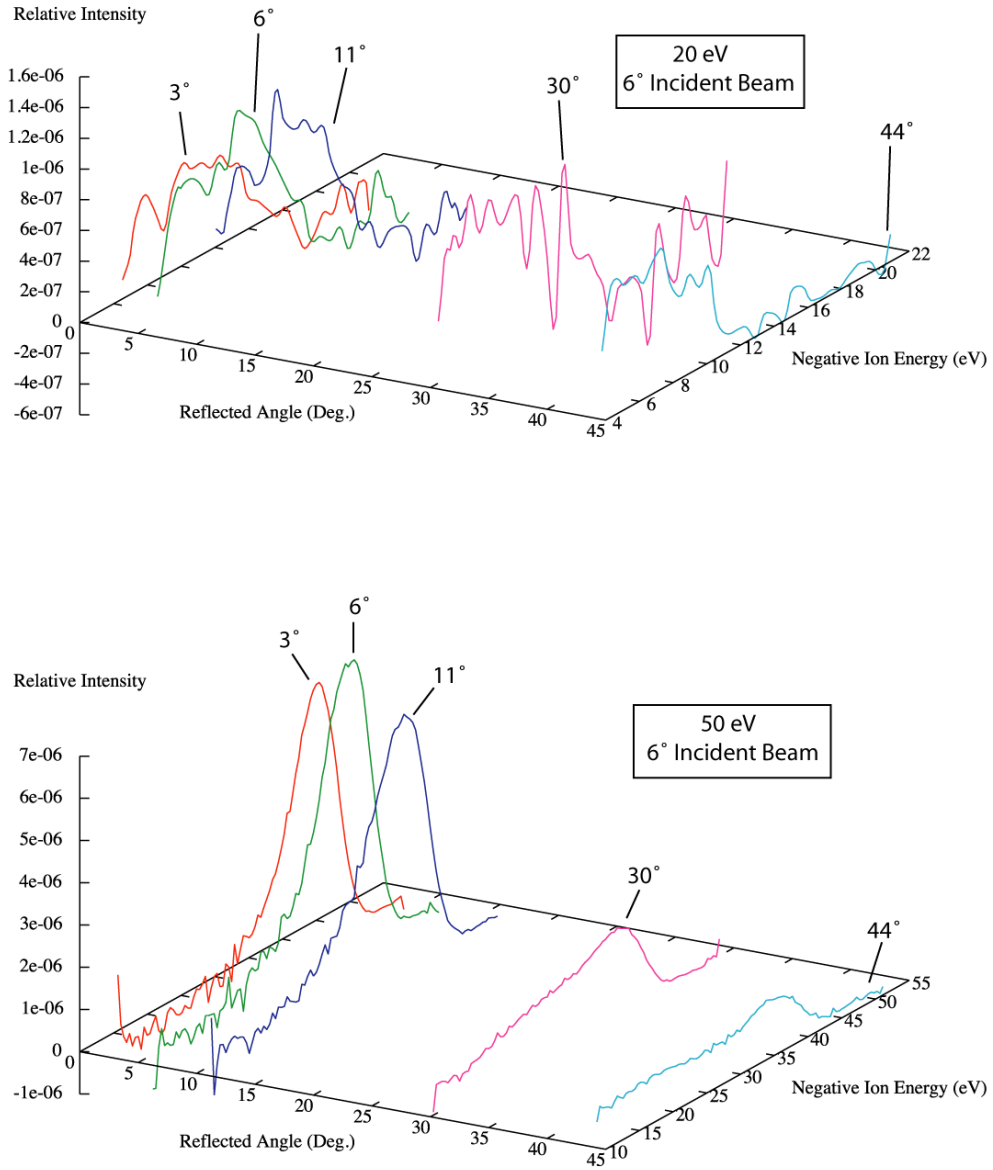

Figure 5.2: Energy distribution for 20 and 50 eV incident beams at 6° to the surface.

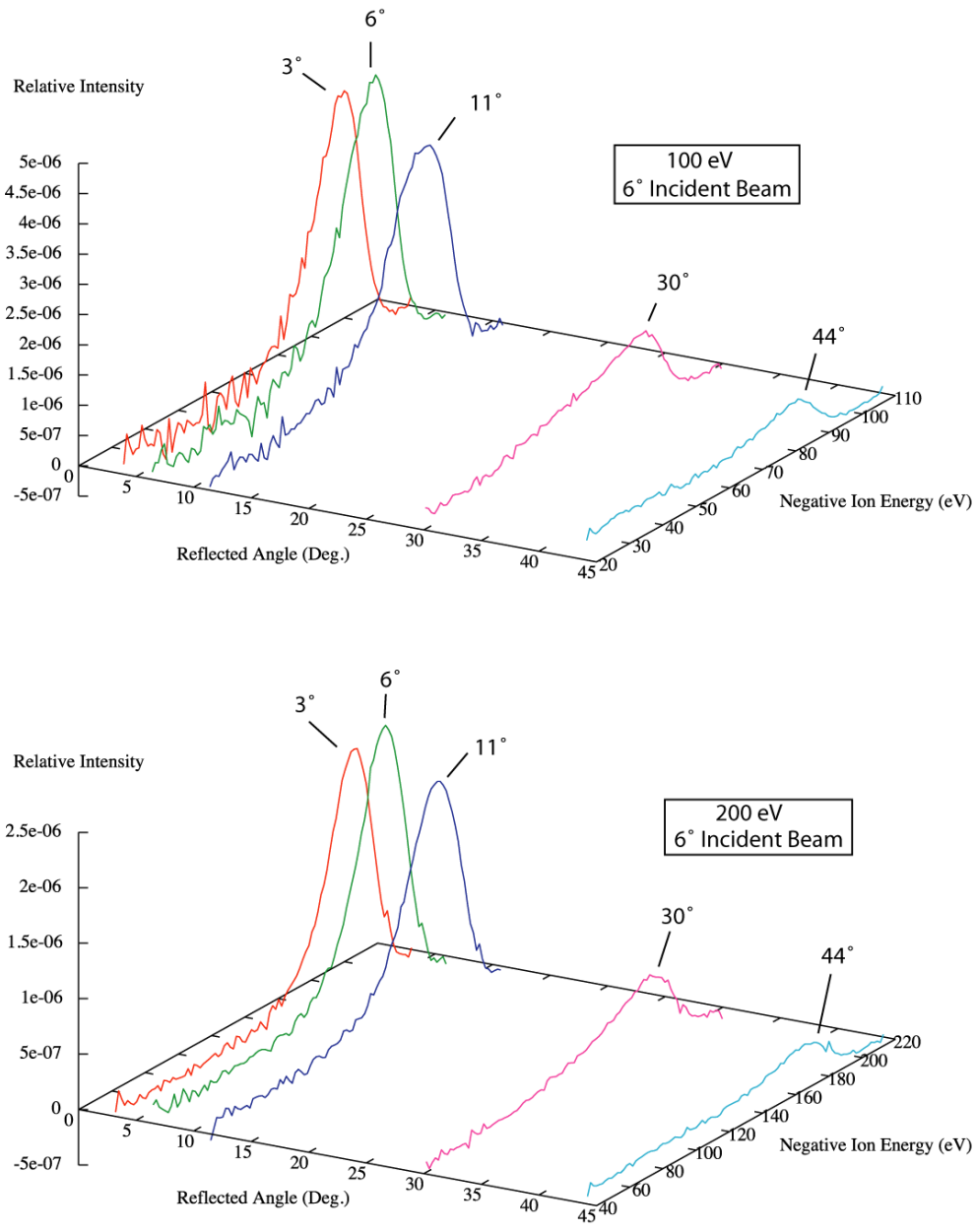

Figure 5.3: Energy distribution for 100 and 200 eV incident beams at 6° to the surface.

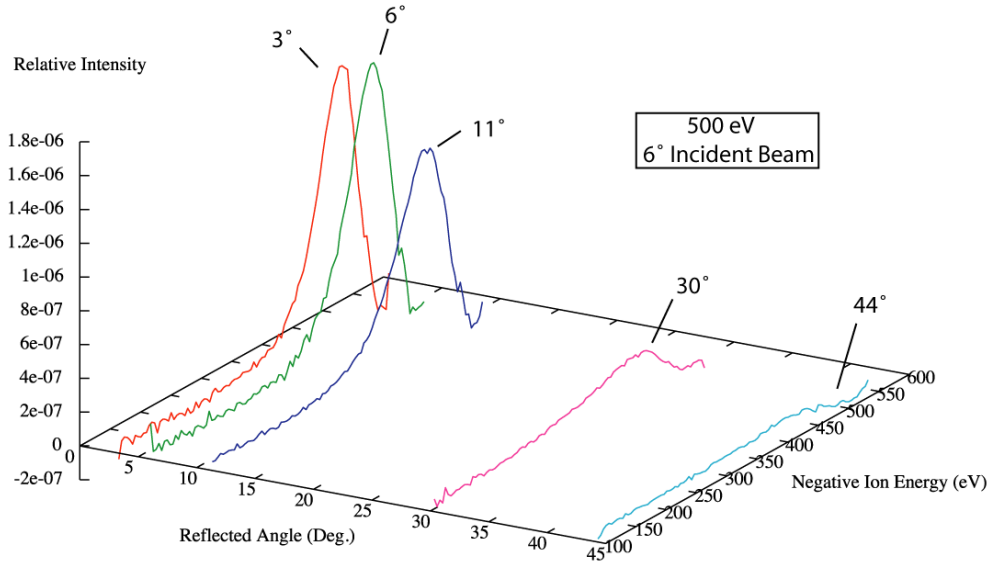

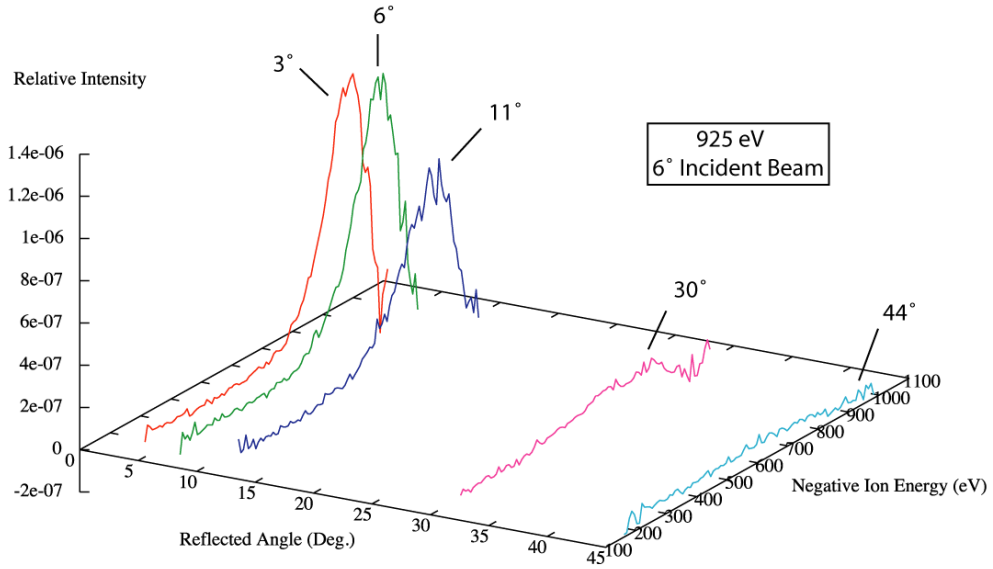

Figure 5.4: Energy distribution for 500 and 925 eV incident beams at 6° to the surface.

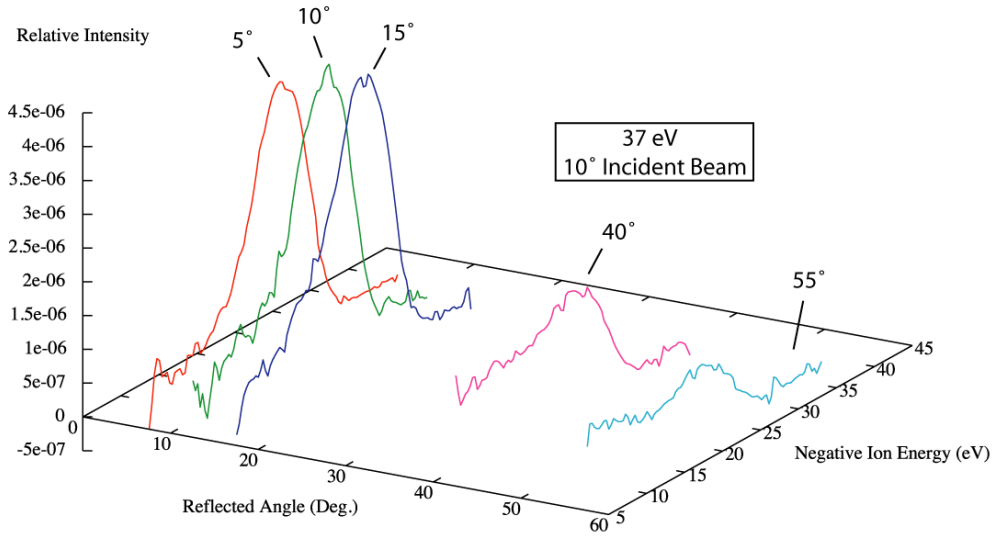

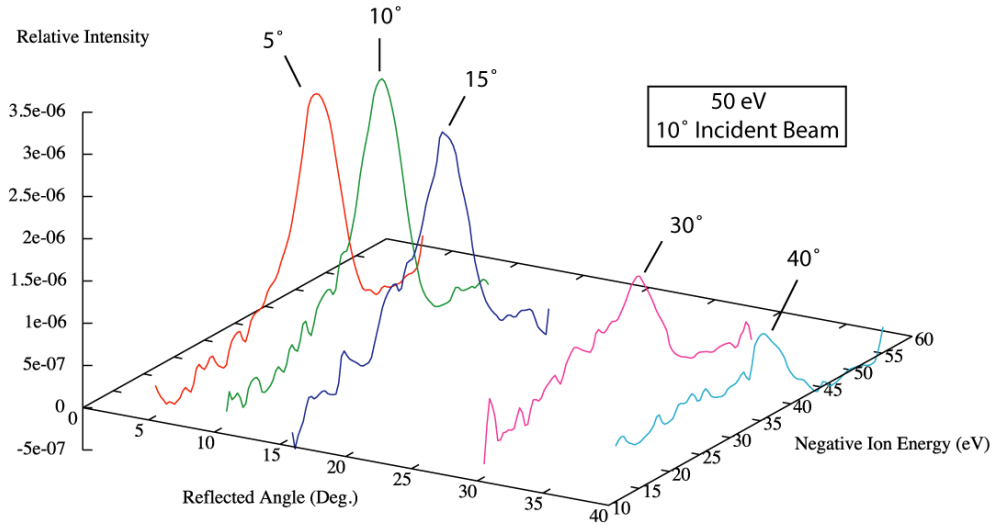

Figure 5.5: Energy distribution for 37 and 50 eV incident beams at 10° to the surface.

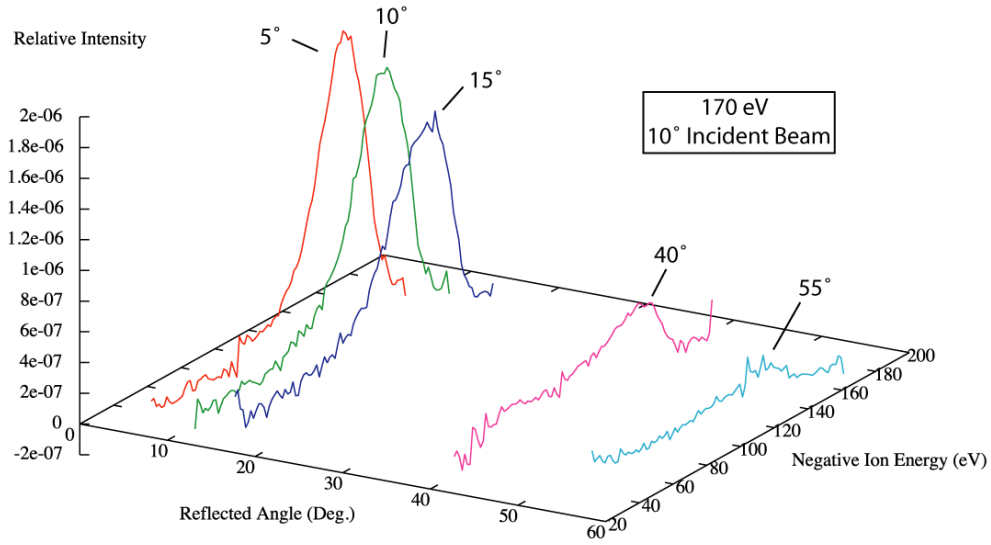

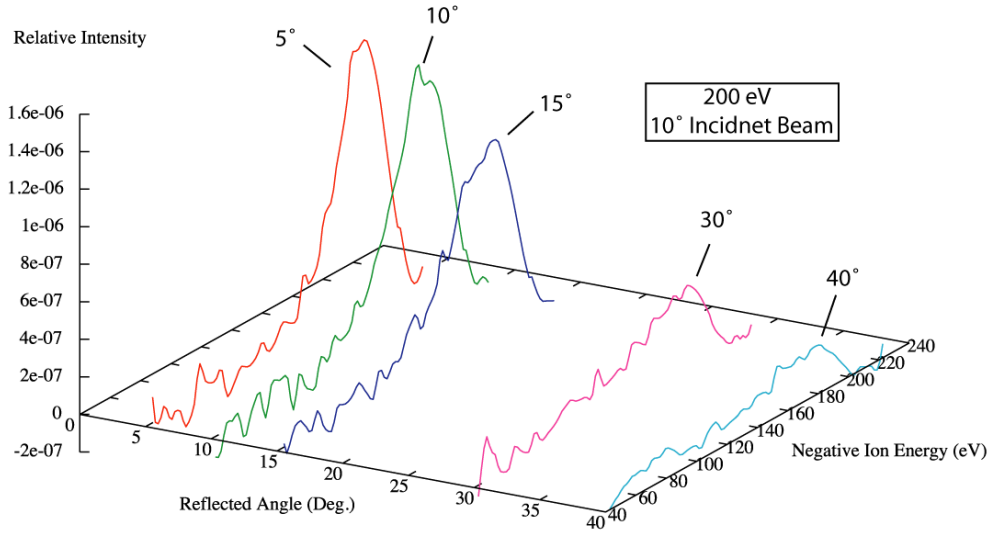

Figure 5.6: Energy distribution for 170 and 200 eV incident beams at 20° to the surface.

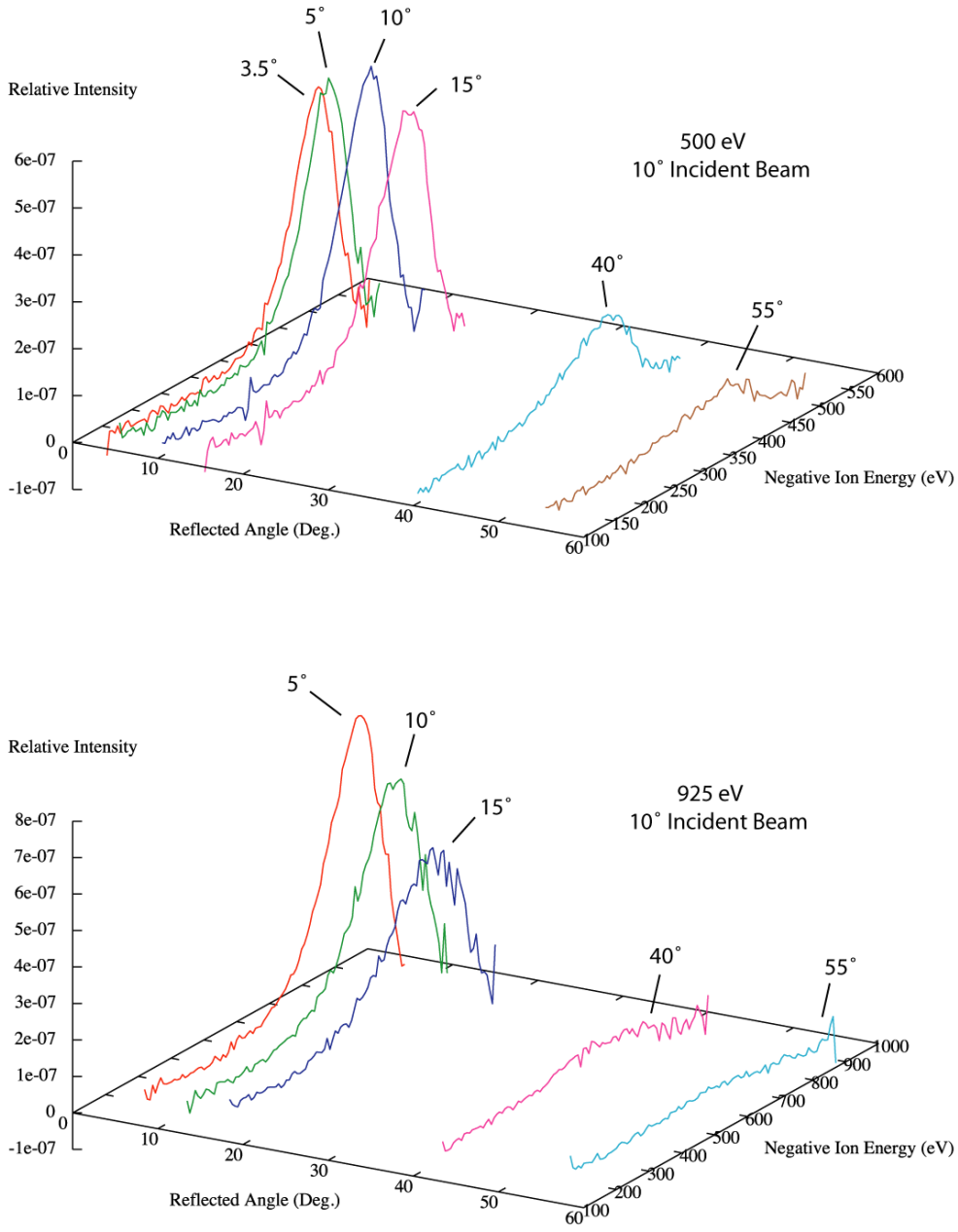

Figure 5.7: Energy distribution for 500 and 925 eV incident beams at 10° to the surface.

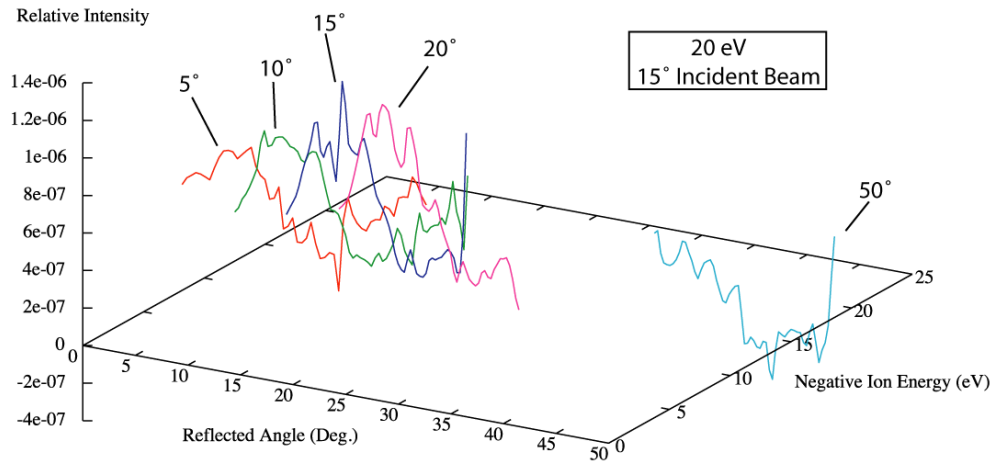

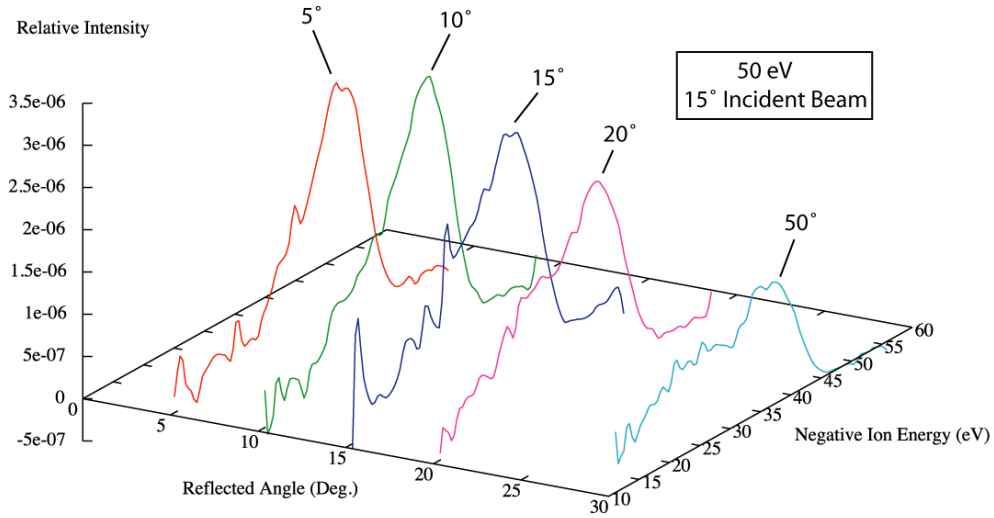

Figure 5.8: Energy distribution for 20 and 50 eV incident beams at 15° to the surface.

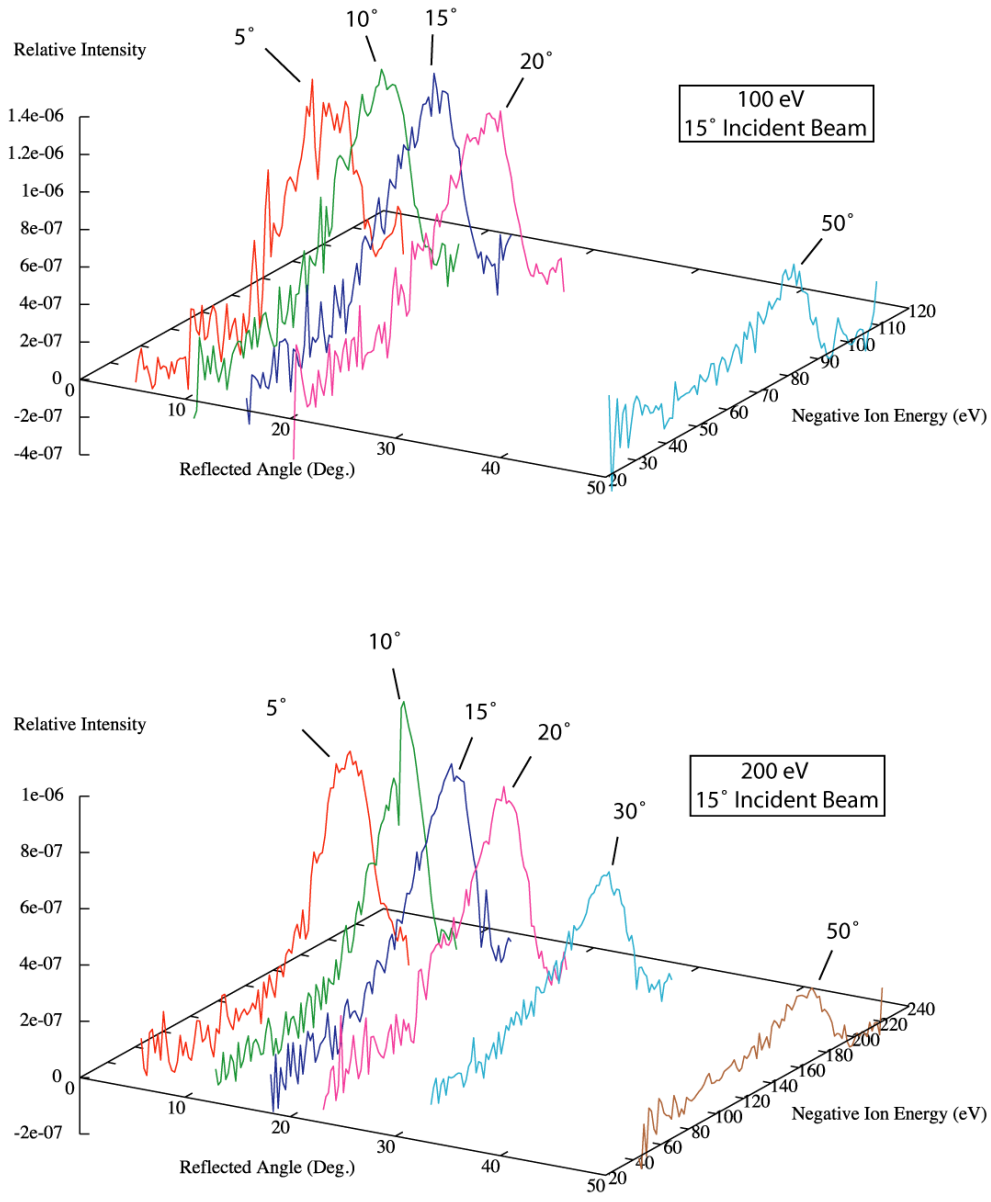

Figure 5.9: Energy distribution for 100 and 200 eV incident beams at 15° to the surface.

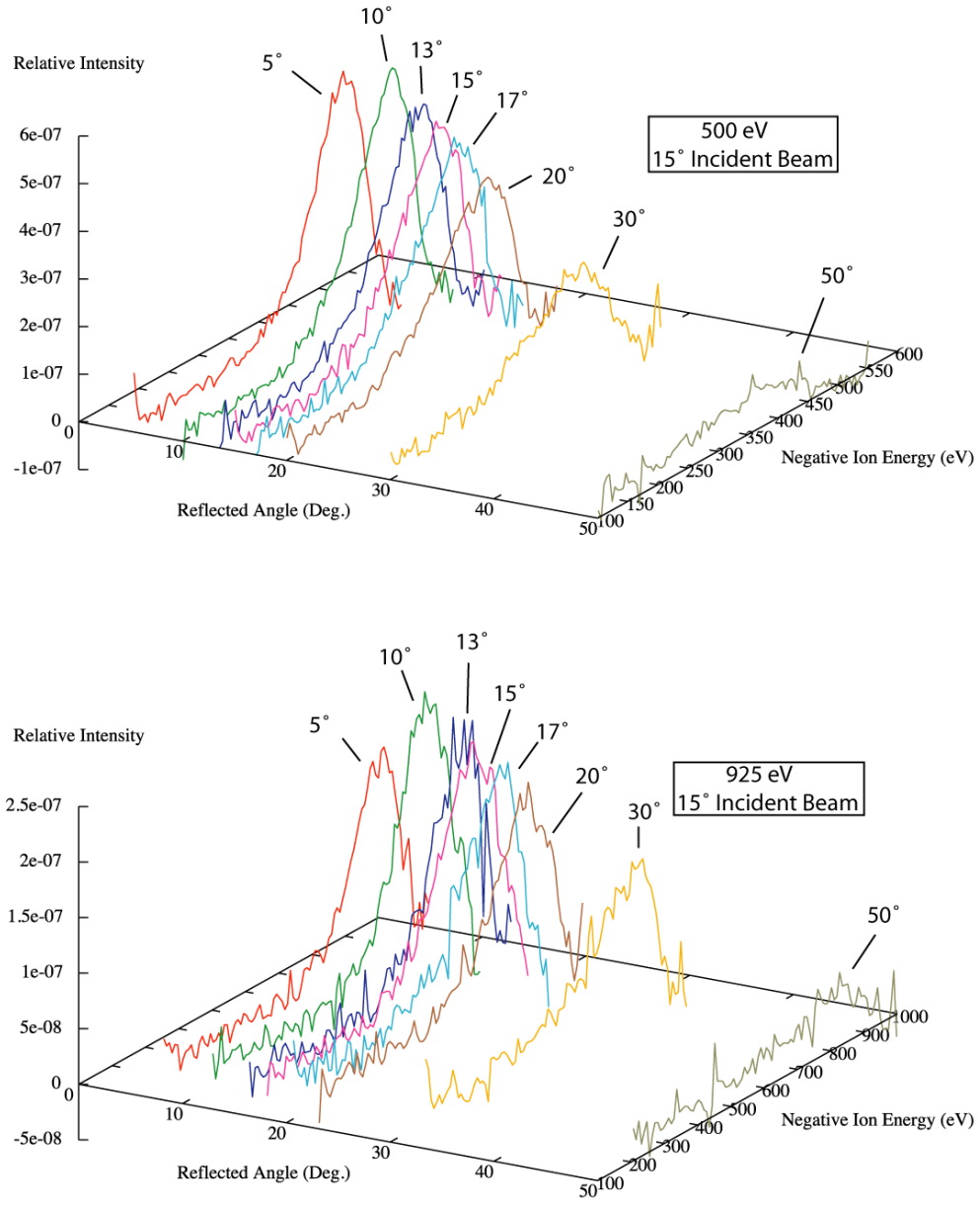

Figure 5.10: Energy distribution for 500 and 925 eV incident beams at 15° to the surface.

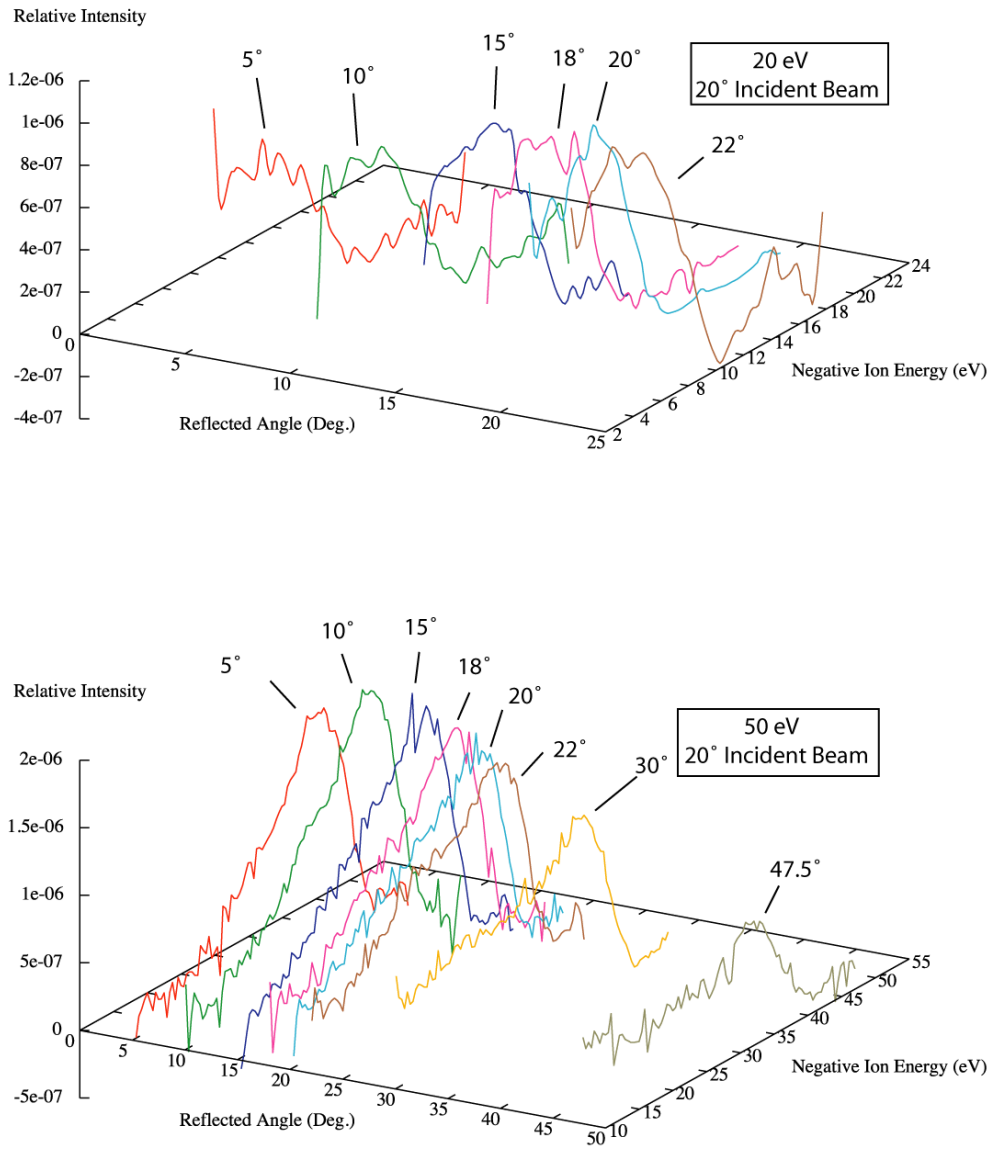

Figure 5.11: Energy distribution for 20 and 50 eV incident beams at 20° to the surface.

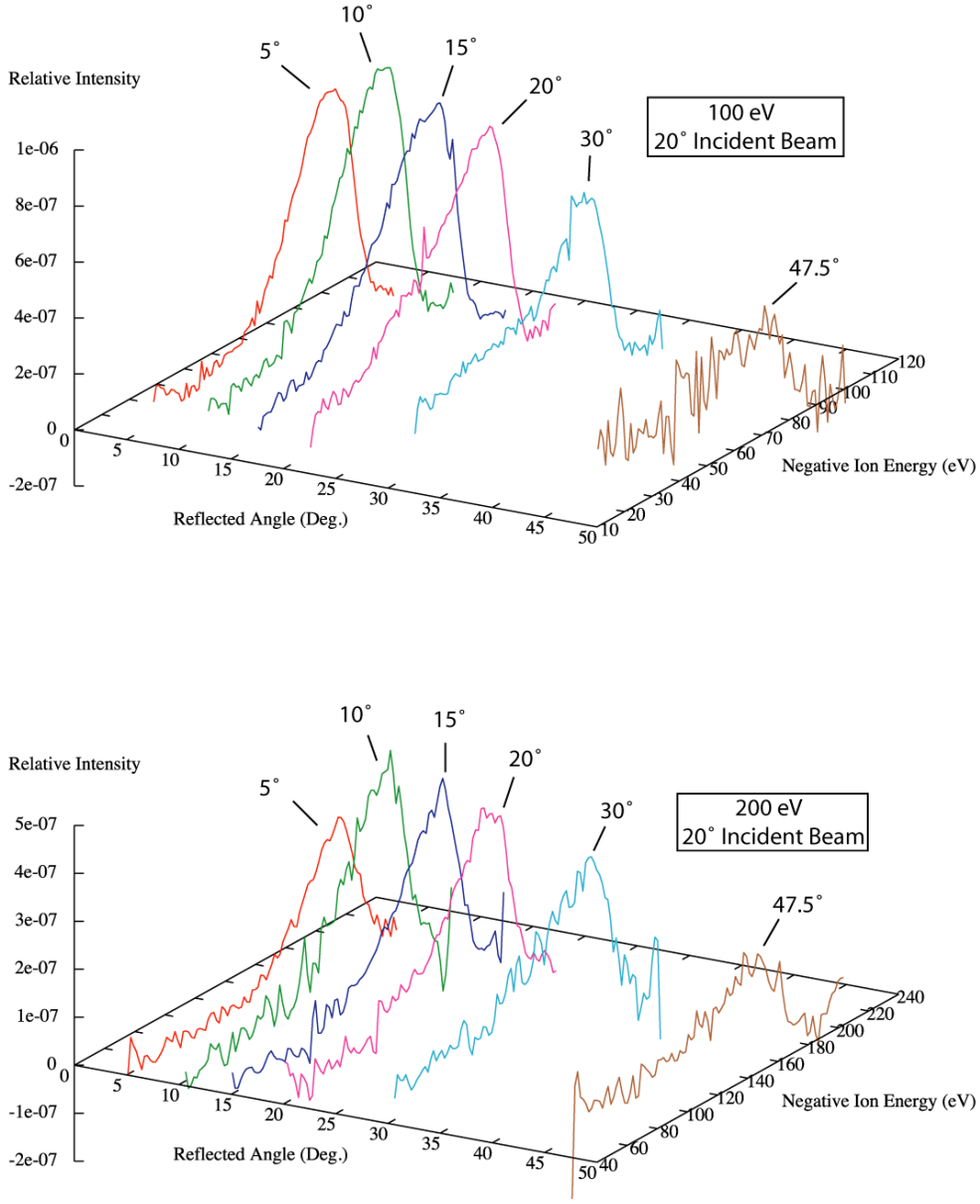

Figure 5.12: Energy distribution for 100 and 200 eV incident beams at 20° to the surface.

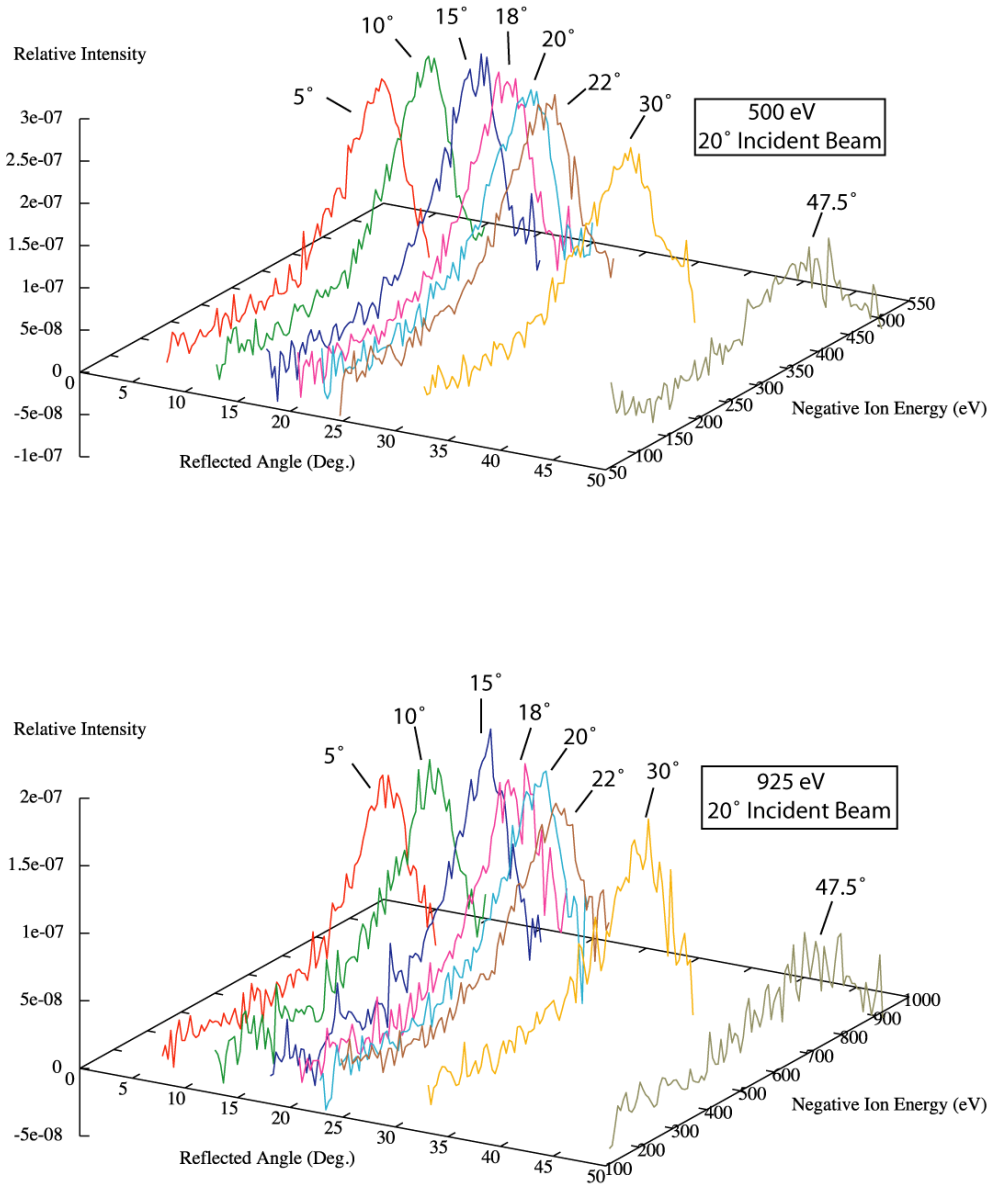

Figure 5.13: Energy distribution for 500 and 925 eV incident beams at 20° to the surface.

collisions with the surface have a higher chance of backscattering around specular reflection and lower angles. The minimum energy loss of the backscattered negative ions was measured from the integrated energy distributions by finding the negative ion cutoff voltage (Fig. 5.1). This avoids uncertainties introduced by the the peak broadening introduced by smoothing to get the energy distributions. The minimum energy loss calculated using low incident and reflection angles was found to be 8.6 $\pm$ 0.8 eV. The negative ion energy distributions peak around 90% of the incident beam kinetic energy minus the minimum energy loss value.

The lowest incident beam energy was 20 eV. The energy spectra for the reflected negative ions show a double peak at some of the reflected angles and do not form single peaks (Fig. 5.2 top, Fig. 5.8 top and Fig. 5.11). For the integral energy distribution data for 20 eV beams there is no clear separation between the slope for the secondary electrons emitted from the surface and the backscattered negative ions (Fig. 5.14). For all the higher energy beams there is a clear separation between the secondary electrons and the backscattered ions.

Angular distributions (Fig. 5.15, Fig. 5.16, Fig. 5.17, Fig. 5.18) of the reflected negative ions were measured for all incident beam energies. The results exclude reflected H^- with energies less than 20% of the incident beam energy. This was done to remove contributions from secondary electrons. Less than 10% of the total negative current yield was eliminated by this procedure. The highest current was within 5° of the specular angle for most of the tests. High incident angles lead to a broader angular distribution around the peak than low incident angles. The 20 eV beam at 6° and 15° to the surface have similar angular distributions. The secondary

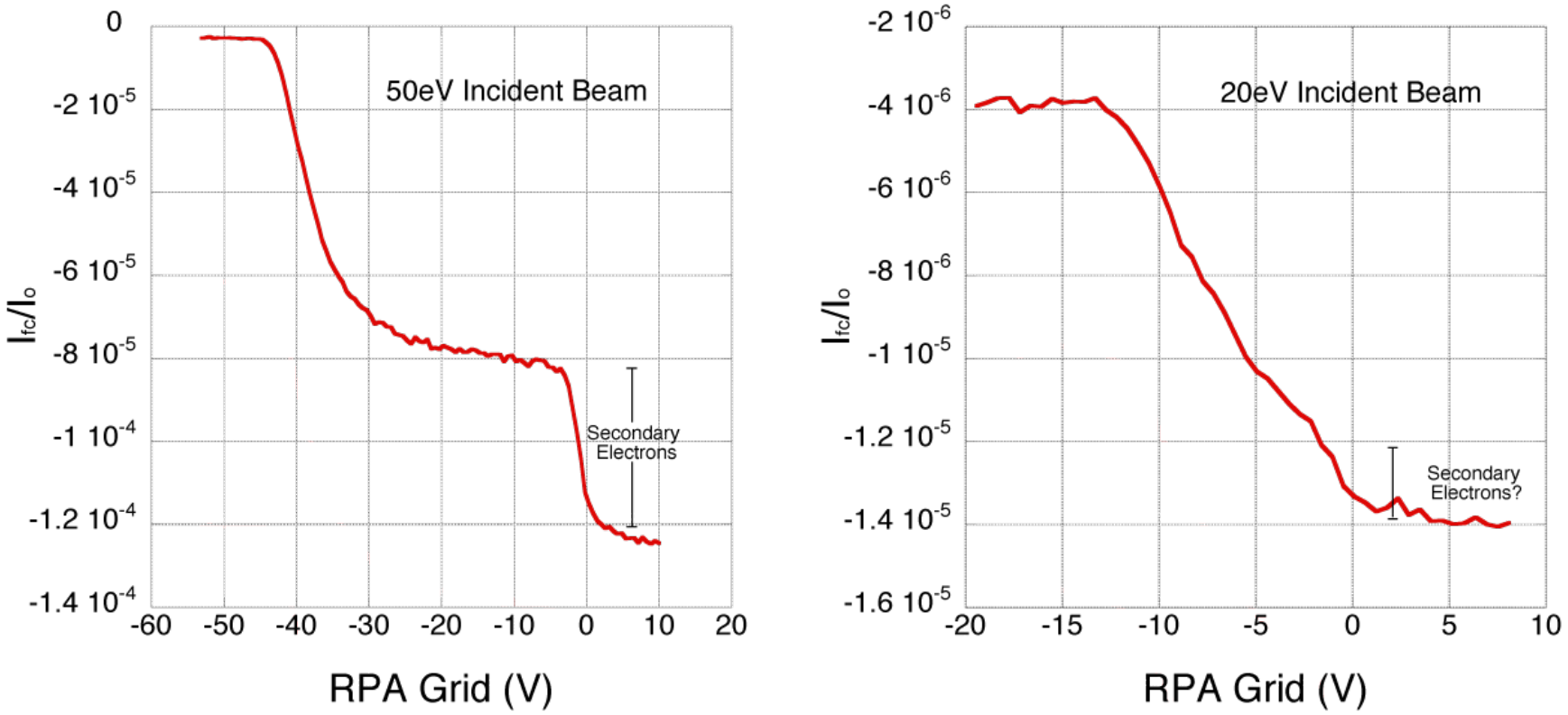

Figure 5.14: Integral energy distributions are shown for a 50 eV (left) and 20 eV (right) neutral hydrogen beam, specularly reflected at 6° from the tungsten surface. The low energy secondary electrons are clearly separated from the H^- ions for incident beams of 50 eV and higher. The separation is not complete for the 20 eV incident beam.

electrons leave the surface over a much wider angular range than the negative ions and would increase the measured peak width of the angular distribution.

The angular distributions only covered a small area in the plane perpendicular to the surface. Reflected ion angular distributions that are not within a few degrees of this plane cannot be measured with the RPA. To extend the angular distribution data, simulations were done using the Stopping and Range of Ions in Matter (SRIM) 2006 software of hydrogen atoms backscattering from a tungsten surface. To calculate the conversion efficiency, the full angular distribution of the reflected ions is needed, but cannot be measured by the RPA. The SRIM software can calculate the exit angles of all reflected particles from a surface. The electronic and nuclear stopping procedures are discussed by Ziegler, Biersack and Littmark [14]. The software is updated about every 5 years. SRIM 2006 allows the user to construct a layered object of different atoms or molecules and simulates the internal scattering of incident energetic particles. To model a laboratory surface, a 1 nm layer of liquid water (H 66.6%, O 33.3%, 1g/cm^3 density) was set on top of a 1 μm layer of tungsten. The water layer is a simple model of the adsorbates that would be present on the surface in the experiment. The software calculates the energy loss and scattering angles for each of the atoms in the incident beam. After the first collision the new direction and energy are used to find the where the next collision event takes place in the target. Collisions are calculated for an incident atom until either all the initial energy is lost or the direction from a scattering event leads the atom out of the surface. In the latter case, SRIM records the direction cosines of the exiting atom to a file. This data file contains the entire distribution

of atoms that backscatter from the surface. SRIM does not calculate any type of charge exchange between the atom and target but it is assumed that any charge exchange occurs during the outward trajectory of the atom and does not perturb the trajectory. The accuracy of the absolute conversion efficiencies depends on the accuracy of the SRIM simulation of the scattering distribution of the real surface away from the RPA field of view. Angular distributions were generated from the SRIM simulations by convoluting the full SRIM output with the RPA resolution to create data that can be compared with the instrument measurements. It is assumed that the SRIM data will be an accurate representation of the actual data outside of the range of the instrument if there was agreement over the range covered by the instrument.

The results of the calculations are compared with the experiment data in Fig 5.15 to Fig 5.18. The quantity of most interest in this work is the total conversion efficiency of the surface, γ^-, where

$$\gamma^- = \frac{N^-_{out}}{N^0_{in}}, \tag{5.1}$$

and N^0_{in} is the incident flux of neutral atoms and N^-_{out} is the total flux of negative converted ions leaving the surface. The quantity measured by the Denver apparatus is the total conversion efficiency into a small solid angle Ω above the surface,

$$Q_{Den} = \frac{N^\Omega_{out}}{N^0_{in}}, \tag{5.2}$$

here N^Ω_{out} is the number of atoms backscattered into the solid angle Ω of the RPA. The SRIM simulation gives the total number of backscattered atoms from the surface and their direction upon leaving the surface. The calculated angular distributions

are convoluted with the angular acceptance of the RPA by counting the backscattered atoms that have an exit trajectory in a solid angle of the same size as the Denver RPA and assuming the atoms are all negative ions,

$$Q_{SRIM} = \frac{N_{out}^{\Omega}}{N_{out}^{-}}. \tag{5.3}$$

If the SRIM distribution and the data for a particular angle and incident energy agree over the angles spanned by the RPA, it is reasonable to assume that the N_{out}^{Ω} of the simulation is a good representation of the data for angles beyond the range of the RPA. Scaling the SRIM distribution with the experimental distribution then allows an estimate of the total negative ion current reflected from the surface.

$$\gamma^{-} = \frac{Q_{Den}}{Q_{SRIM}} \tag{5.4}$$

The calculated SRIM distributions are usually more narrow around the maximum reflection angle for the three smaller incident angles than the experimental distributions. At 20° incident angle, the large angle backscatter compared to the measurements, makes total conversion efficiency estimations highly dubious. Of the simulated angular distributions, the closest matches are the 925 eV beam energy incident at 6° to the surface (Fig 5.15), the 200 eV and 500 eV beam energies incident at 10° to the surface (Fig 5.16), and the 200 eV energy incident at 15° to the surface (Fig 5.17). These simulations differed from the experimental data by less than 20% after scaling to the same peak height. The conversion efficiency estimates for these angular distributions are 1.9% ± 0.6.

The SRIM software relies on interatomic potentials to calculate the scattering events between the surface nuclei and the incident atom that are valid for energies

Figure	Beam Energy (eV)	Incident Angle (°)	Stage Heating
5.19	50	6	Baked at 300℃
5.20	500	20	100℃ then 300℃
5.21	50	20	Flashed to 800℃ and let cool
5.22	100	20	Flashed to 800℃ and let cool

Table 5.1: Summary of sample heating

above 1 keV but are less accurate in the energy range used in this experiment. The simulated surface and adsorbates are perfectly flat with no internal defects, unlike surfaces used in the experiment. For this reason only a small number of the simulated angular distributions agree with the measurements. Even with this limited overall agreement, the simulations are useful in estimating the conversion efficiency.

5.1.1.1 Sample Heating

Measurements were made on heated tungsten sample A. The temperature of the stage holding the sample is measured by a thermocouple, however direct measurements of the surface temperature were not possible in this system. Energy distributions at the specular reflection angle were measured for the heated surface. The stage was heated from below with a tungsten heating coil by radiation or radiation and electron bombardment. The stage temperature can be raised to 300℃

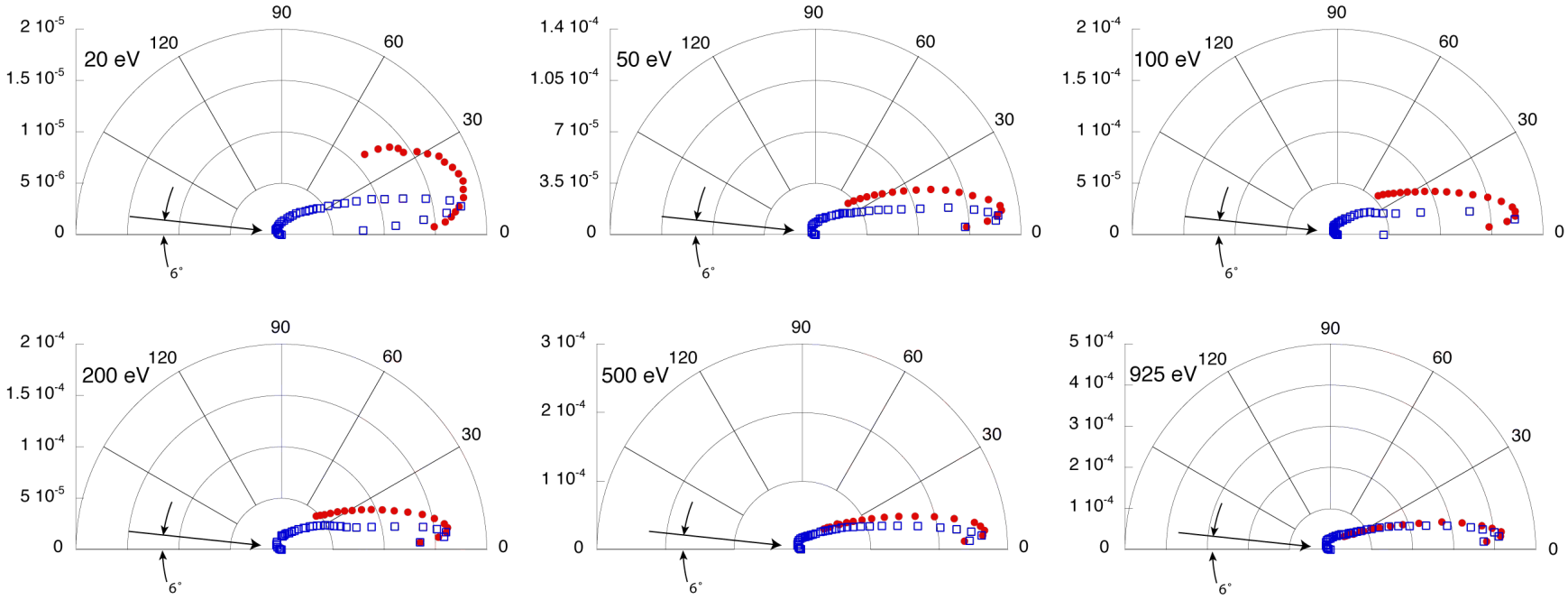

Figure 5.15: Angular distributions for the H beam incident at 6° to the tungsten surface. The experimental data (●) and the SRIM simulations scaled to the same peak height (□) are shown.

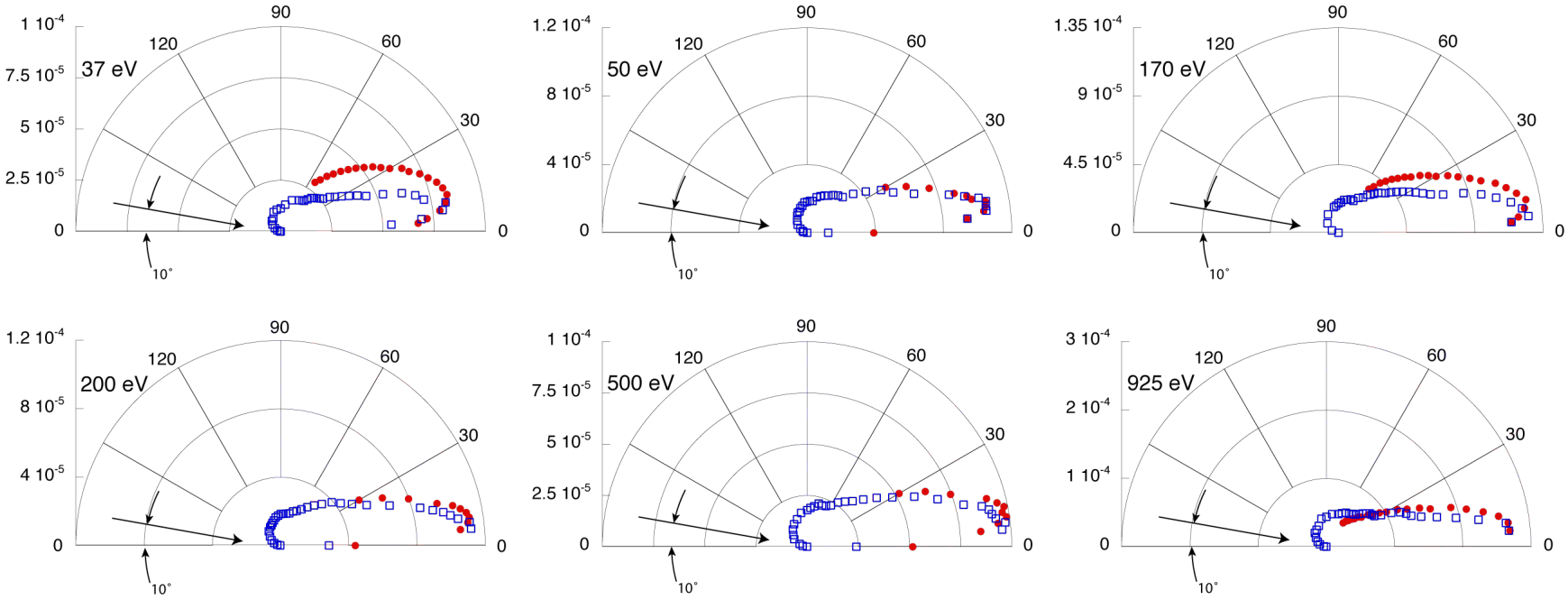

Figure 5.16: Angular distributions for the H beam incident at 10° to the tungsten surface. The experimental data (●) and the SRIM simulations scaled to the same peak height (□) are shown.

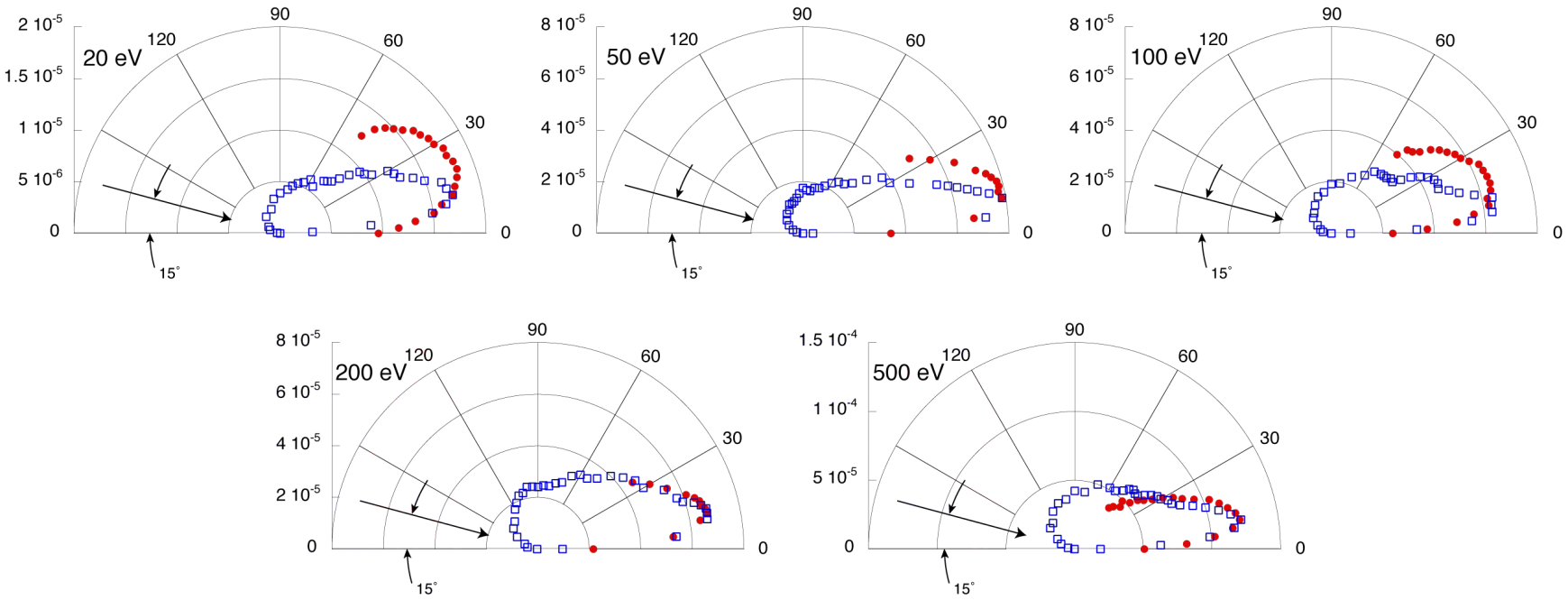

Figure 5.17: Angular distributions for the H beam incident at 15° to the tungsten surface. The experimental data (●) and the SRIM simulations scaled to the same peak height (□) are shown.

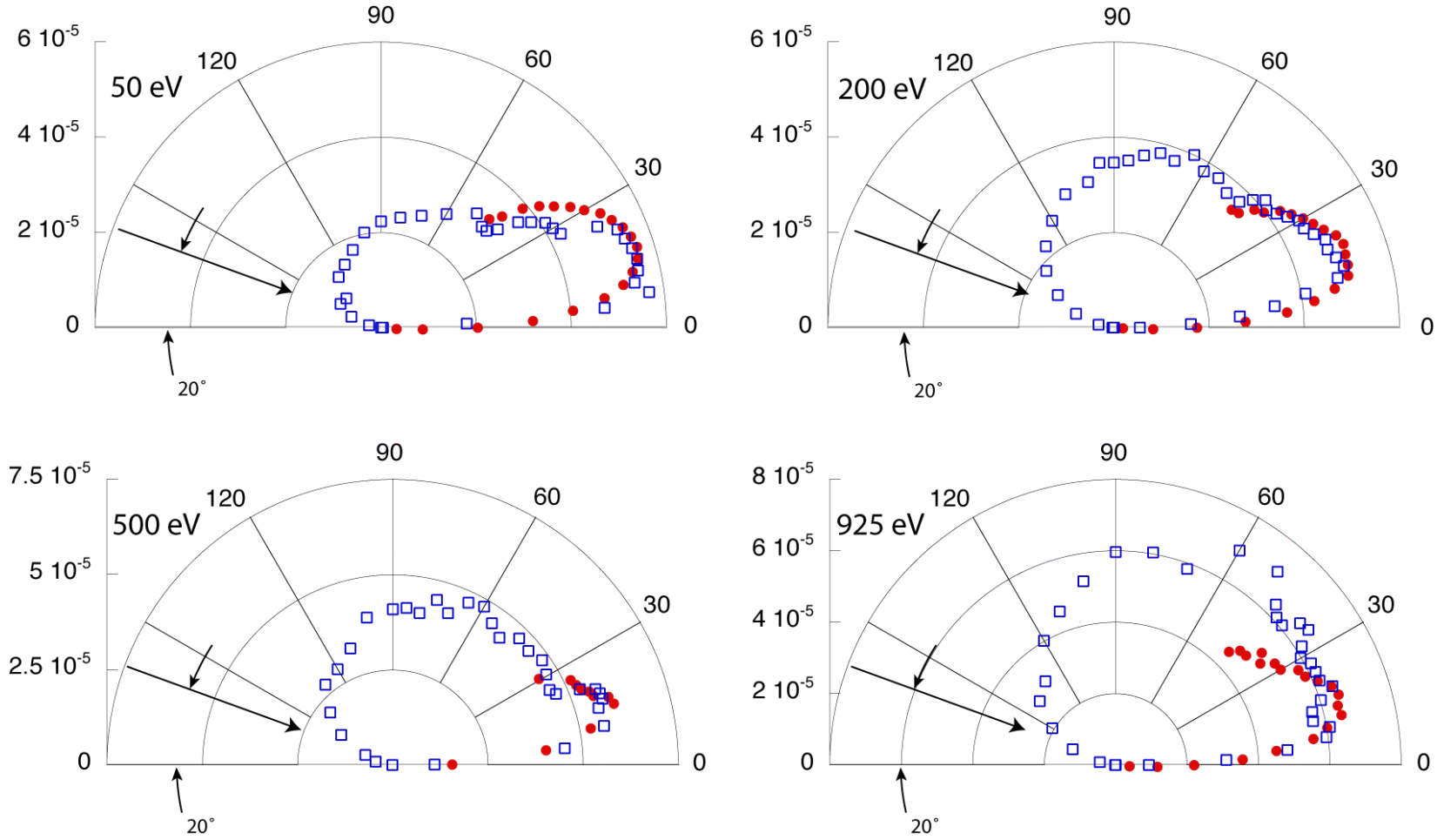

Figure 5.18: Angular distributions for the H beam incident at 20° to the tungsten surface. The experimental data (●) and the SRIM simulations scaled to the same peak height(□) are shown.

using radiation from the coil; with electron bombardment added the stage can reach 800℃. When heating by radiation alone, angular and energy distributions were taken while the stage was maintained at a fixed temperature. When heating by radiation and electron bombardment, the stage was rapidly heated to 800℃ then all heating was removed. Prolonged stage heating above 300℃ results in heating of the detectors which compromises the accuracy of the current measurements. When heating by radiation and electron bombardment the sample and stage are biased positive with respect to the heating coil. This positive bias affects the angular and energy distributions of the reflected negative ions. For this reason, the stage was heated to 800℃ and then the heating was turned off so that data could be taken. The rate at which the stage is heated allows it to reach 800℃ before the temperature of the other components in the chamber rises sufficiently to affect the measurement.

It was observed that heating caused a decrease in the recorded negative ion current from the surface to the RPA. Fig. 5.19 shows the effect of time of heating on negative ion energy distributions. The data are for a 50 eV beam of H-atoms incident on the tungsten surface at 6°. The stage was heated to 300℃ and energy distribution measurements made at fixed time intervals after the stage reached 300℃. With time, the surface temperature approached the stage temperature and the current of scattered negative ions decreased. Fig. 5.20 shows the effect of heating on negative ion yield of a 500 eV beam of H incident at 20° on the surface. The stage was heated first to 100℃ and then 300℃ for 5 minutes and there was a decrease in the negative ion current at the higher temperatures. Finally, the stage was rapidly heated to 800℃ and allowed to cool while energy distribution measurements were taken for an

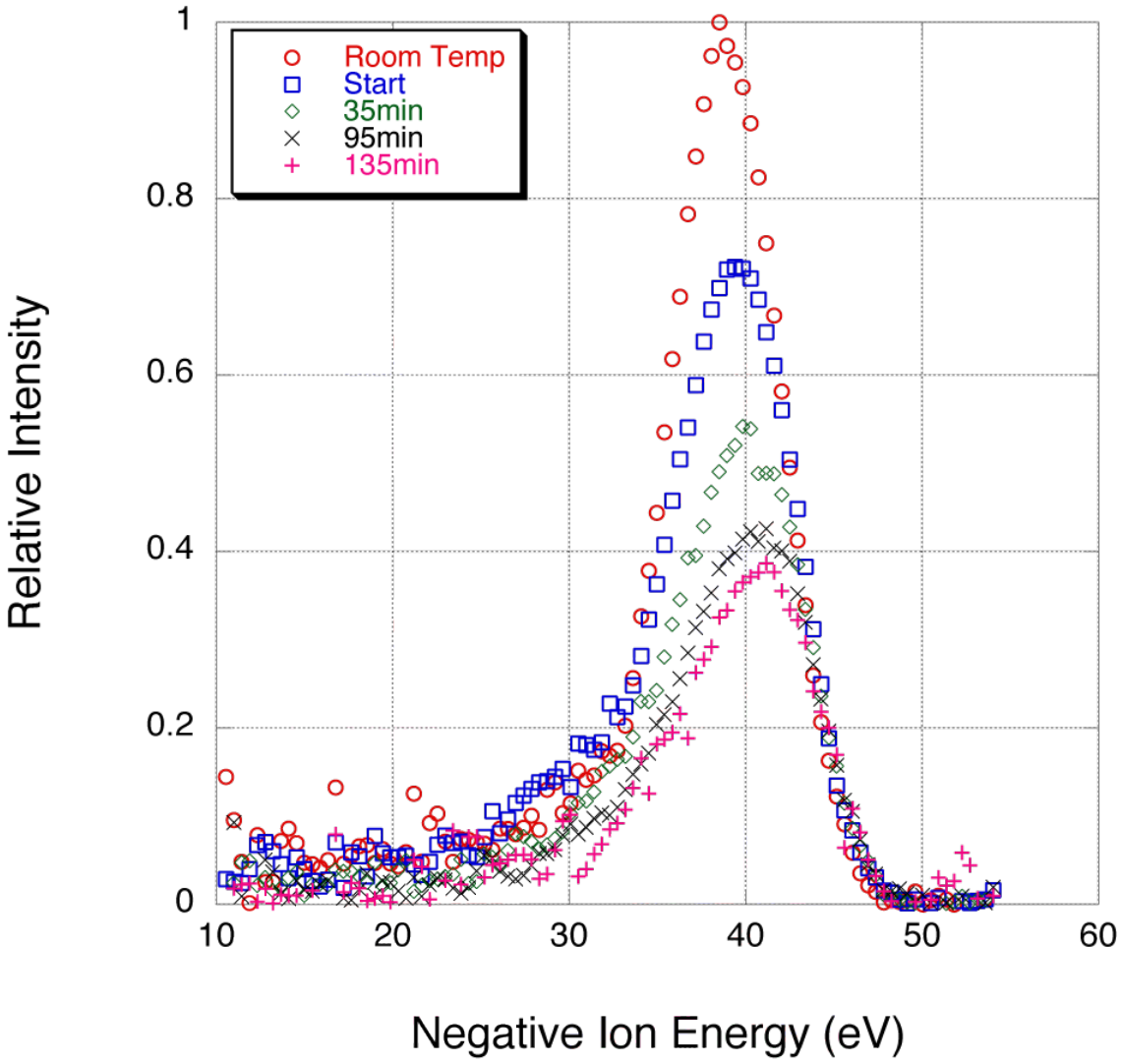

Figure 5.19: Energy distributions of negative ions from the tungsten surface A after the stage reached 300℃ at t = 0. Data were then taken at 35, 95 and 135 minutes after the stage reached 300℃. The incident energy of the beam is 50 eV at 6° to the surface and the observed reflection angle is 6° from the surface.

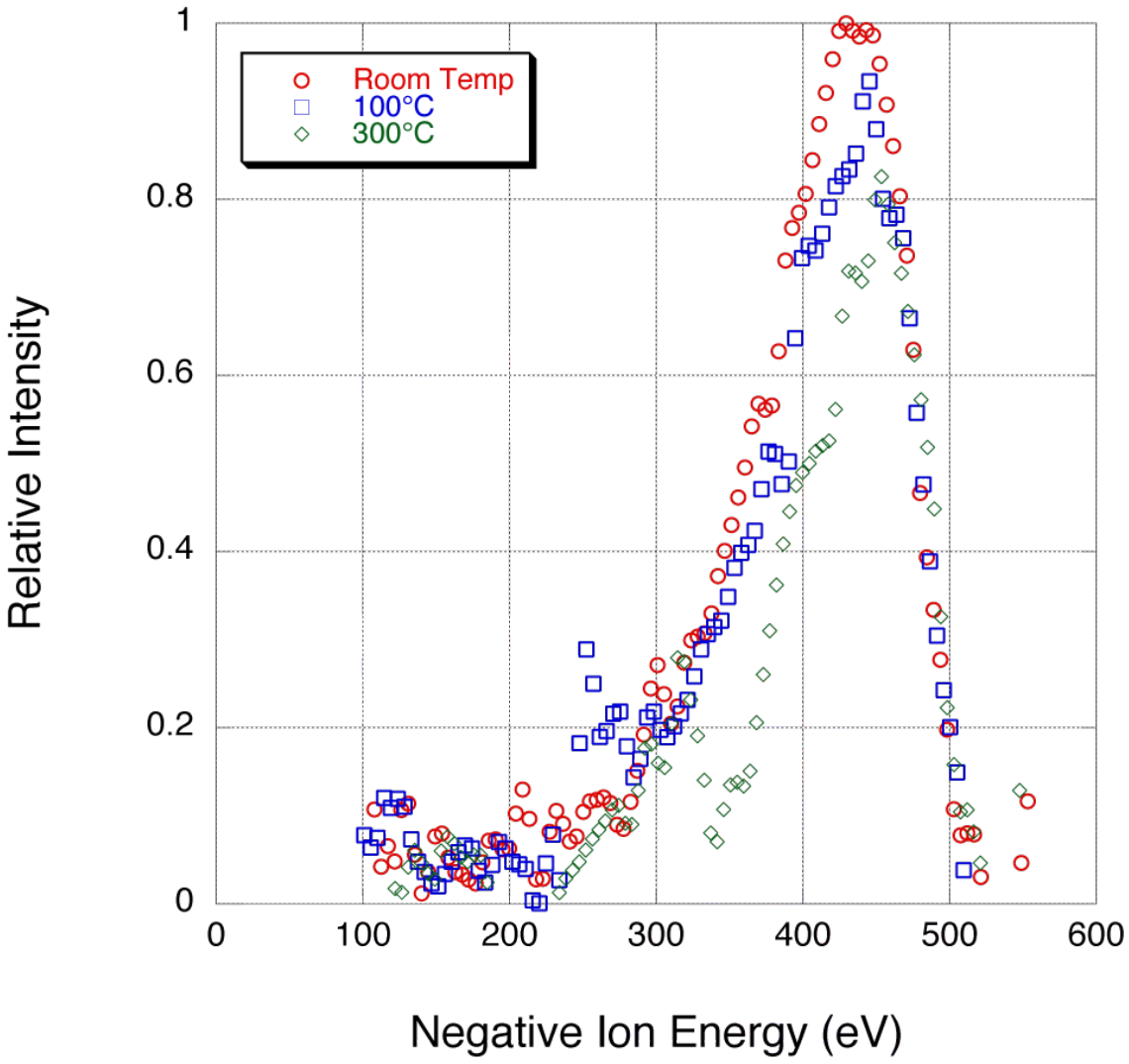

Figure 5.20: Energy distributions for the H^- ions from the tungsten surface after heating the stage for 40 minutes to reach 100℃ and after taking data heating for another 30 minutes to reach 300℃. The surface stage was allowed to be at the target temperatures for 5 minute before taking the measurement. The incident beam energy is 500 eV and the incident and reflected angles are both 20° from the surface.

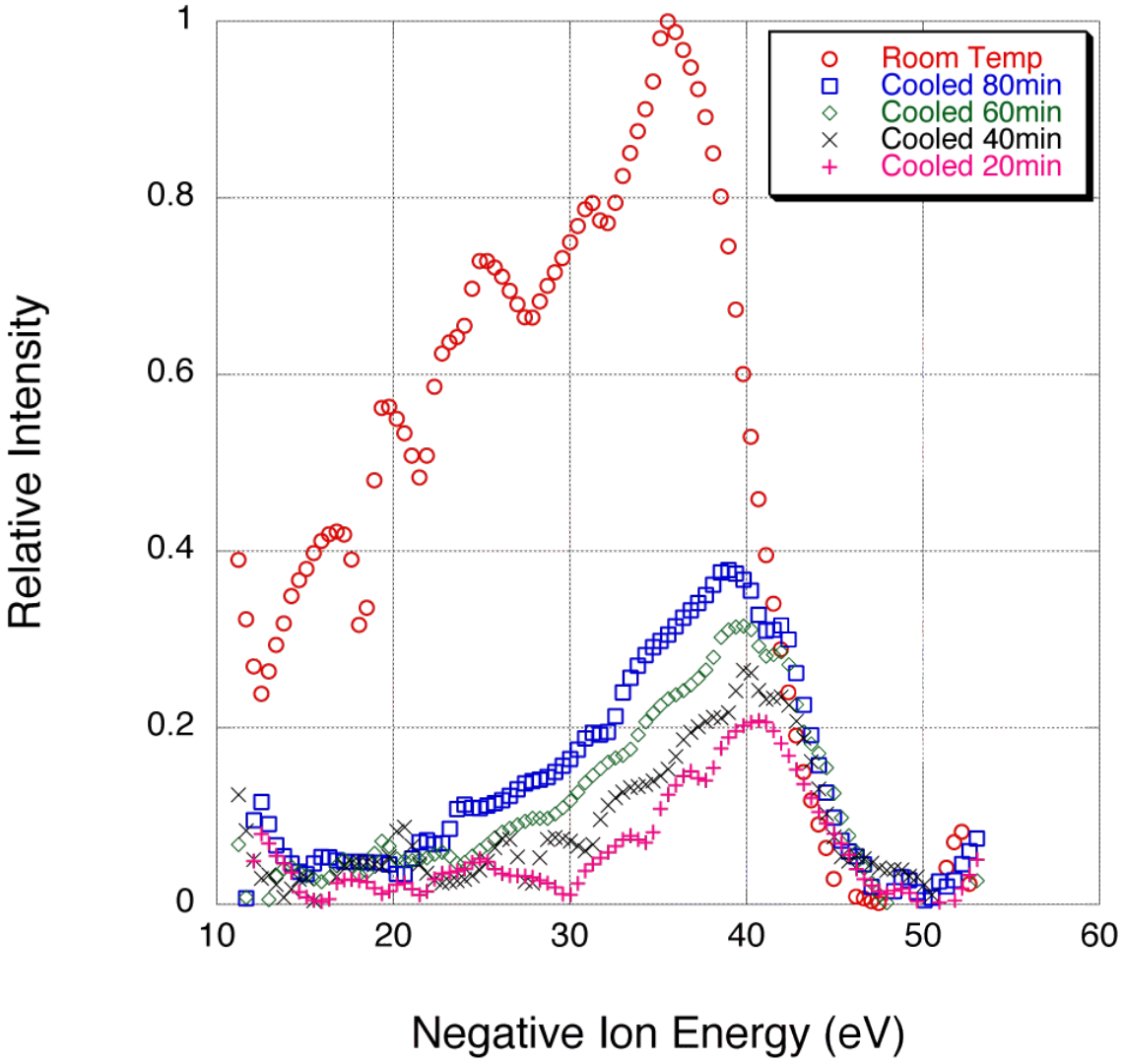

Figure 5.21: Energy distributions during the cooling of the stage supporting the tungsten surface from 800℃. The room temperature data were taken after the sample had been left overnight with no heating. The energy of the incident beam is 50 eV and the incident and reflected angles are both 20° to the surface.

incident beam of 50 eV (Fig. 5.21) and 100 eV (Fig. 5.22) H beams incident at 20° to the surface. The energy distribution for the 50 eV beam showed that as the surface cools the negative ion current increases. For the 100 eV beam, longer cooling times produce larger negative ion currents.

Angular distributions were measured for the surface heated to 63.8℃ and 300℃. For the 63.8℃ surface a 100 eV beam was incident at 6°. For the 300℃ surface a 50 eV beam was incident at 6° and 20° (Fig. 5.23). In the cases of 6° incident angles, the heated distributions show a peak intensity angle of reflection both at about 11.5° above the surface compared to about 7.5° for room temperature measurements, and a larger FWHM, 41° vs 27° for the 50 eV beam and 40° vs 28° for the 100 eV beam. The measurement at 20° has a peak that is shifted at least 10° beyond the room temperature reading and may even lie beyond that. The distribution was much wider than for the room temperature measurement and the measured angular range is not able to cover the full distribution. The estimated conversion efficiency for the heated surfaces vary from about 0.2% ± 0.06 for a 6° beam at 50 eV and 100 eV to 0.8% ± 0.24 for the 20° beam at 50 eV. The best agreement with SRIM calculations was for the 50 eV incident beam at 20°.

Heating caused a drop in conversion efficiency for the tungsten surface. The main change to the surface while heating is the removal of adsorbates. Water, and other molecules and atoms in the air, that collect on the surface seem to increase the number of negative ions scattered.

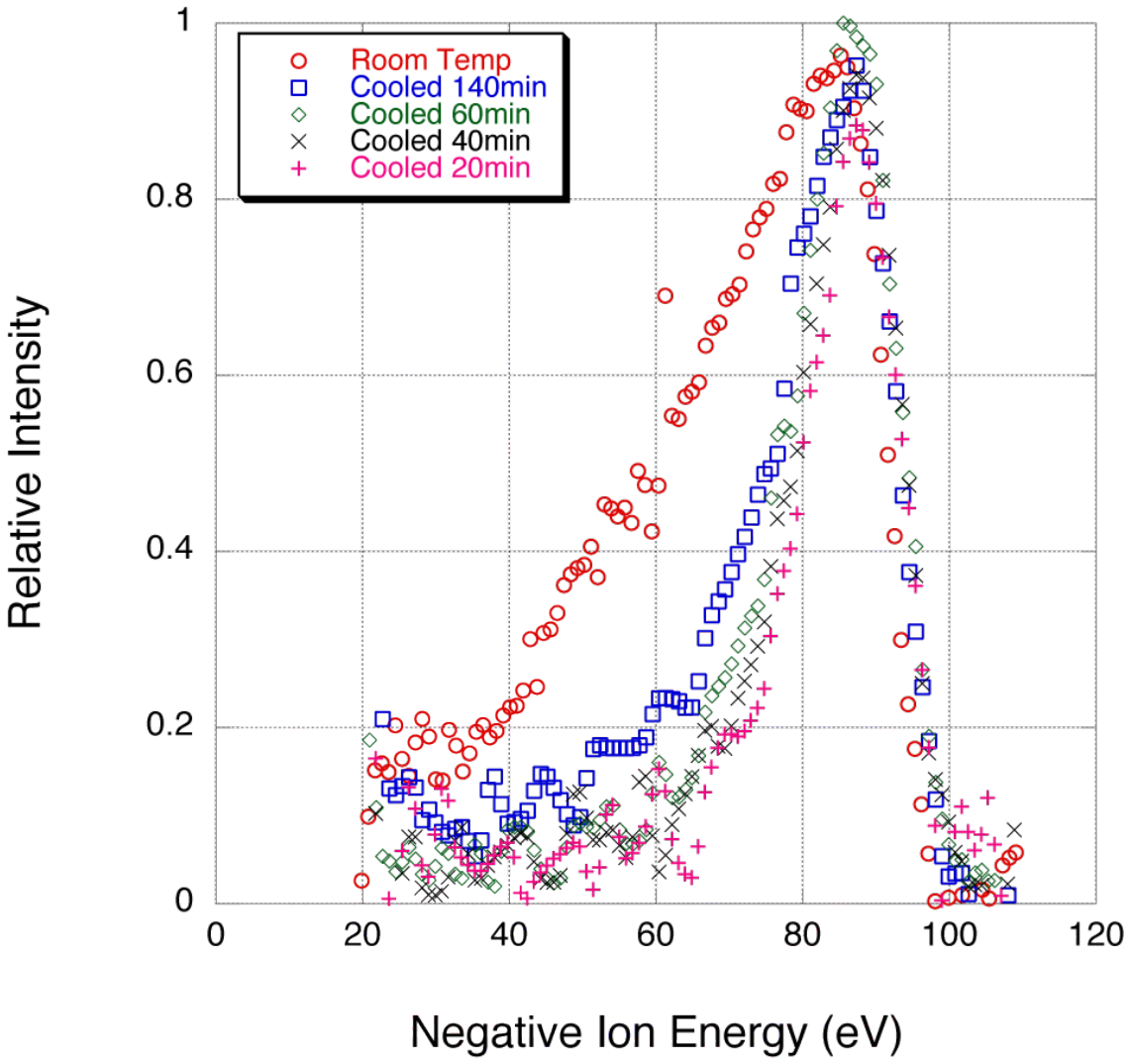

Figure 5.22: Energy distributions for different cooling times of the tungsten surface after being heated to 800℃ and allowed to cool. The incident beam energy is 100 eV and the incident and reflected angles are 20° to the surface. The room temperature measurement had a higher overall negative ion current but only small changes are seen over the time during which the stage was allowed to cool.

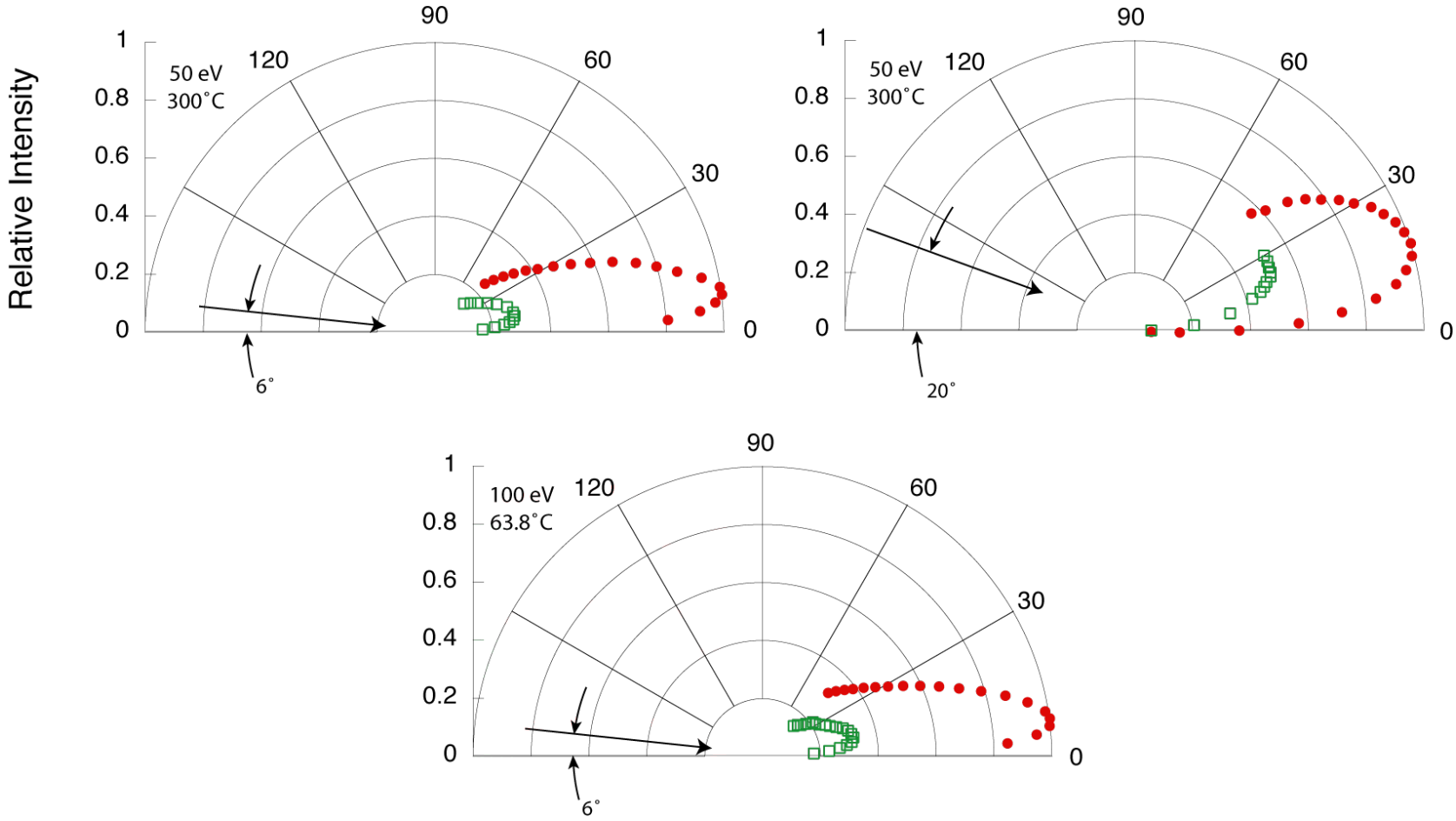

Figure 5.23: Angular distributions for the H beam incident on the tungsten surface on the heated stage (shown with □) at different incident beam angles and energies compared to the room temperature stage (shown with •).

5.1.2 Diamond-like Carbon Surface

There were only limited data for the DLC surface. The energy and angular distributions were for 195 eV and 390 eV incident energies and a 10° incident beam angle. The minimum energy loss for this surface was measured to be 4.6 ± 0.7 eV. The energy distributions look similar to those for tungsten. The highest intensities are generally in the specular direction and decrease at larger angles above the surface (Fig. 5.24).

Calculated distributions for a carbon surface 10000 Å thick covered by a 10 Å thick layer of water match well with the experimental results at both beam energies (Fig. 5.25). The scaled distributions give an estimated value for total conversion efficiency of 2.5% ± 0.5% and 1.8% ± 0.4% for the 195 and 390 eV incident beams respectively.

The stage was heated to 300℃ over a 40 minute time period after which it was held constant at that temperature while energy distributions were measured for the DLC surface at different times for a 65 eV incident beam (Fig. 5.26). Again it was observed that the negative ion flux from the surface decreased as the surface temperature increased. The conversion efficiency continued to decrease over the two hour period that the surface stage was held at 300℃.

Within experimental uncertainty, the diamond like carbon surface has the same conversion efficiency as the tungsten surface. Heating the surface caused a decrease in the negative ion current from the surface but the drop was not so dramatic as in the tungsten case. The angular and energy distributions for the two surfaces

are similar. These similarities were assumed to be characteristic for negative ion backscattering from surfaces made from different materials and this was used to design a negative ion lens for the general measurements described in the next section.

5.2 General Measurements

The general measurements were designed to assess the conversion efficiency of different surfaces without needing to take many separate measurements at different angles above the surface. Two separate measurements are made with the apparatus during an experiment, the incident neutral flux and the negative ion flux reflected from the surface. Separate CEMs are used for the two measurements and both share a common preamplifier, amplifier, pulse height analyzer and multichannel analyzer. No absolute calibration has been done for the two CEM detectors for incident particle energy, so that the results are relative to each other. These relative measurements between different surfaces are shown and they can be put on an absolute scale by reference to the tungsten surface that was calibrated absolutely in Denver. The lens is designed to focus the negative ions from the surface under test into the detector so that negative ions with a range of angles and energies leaving the surface are collected. When a negative ion is reflected from the surface at an angle and/or energy outside of the collection range, it will be accelerated into one of the lens plates and lost. The angular distributions measured at Denver for tungsten and DLC, show that a large fraction of the negative ions reflected from the surface are concentrated over a small angular range. The lens system does not

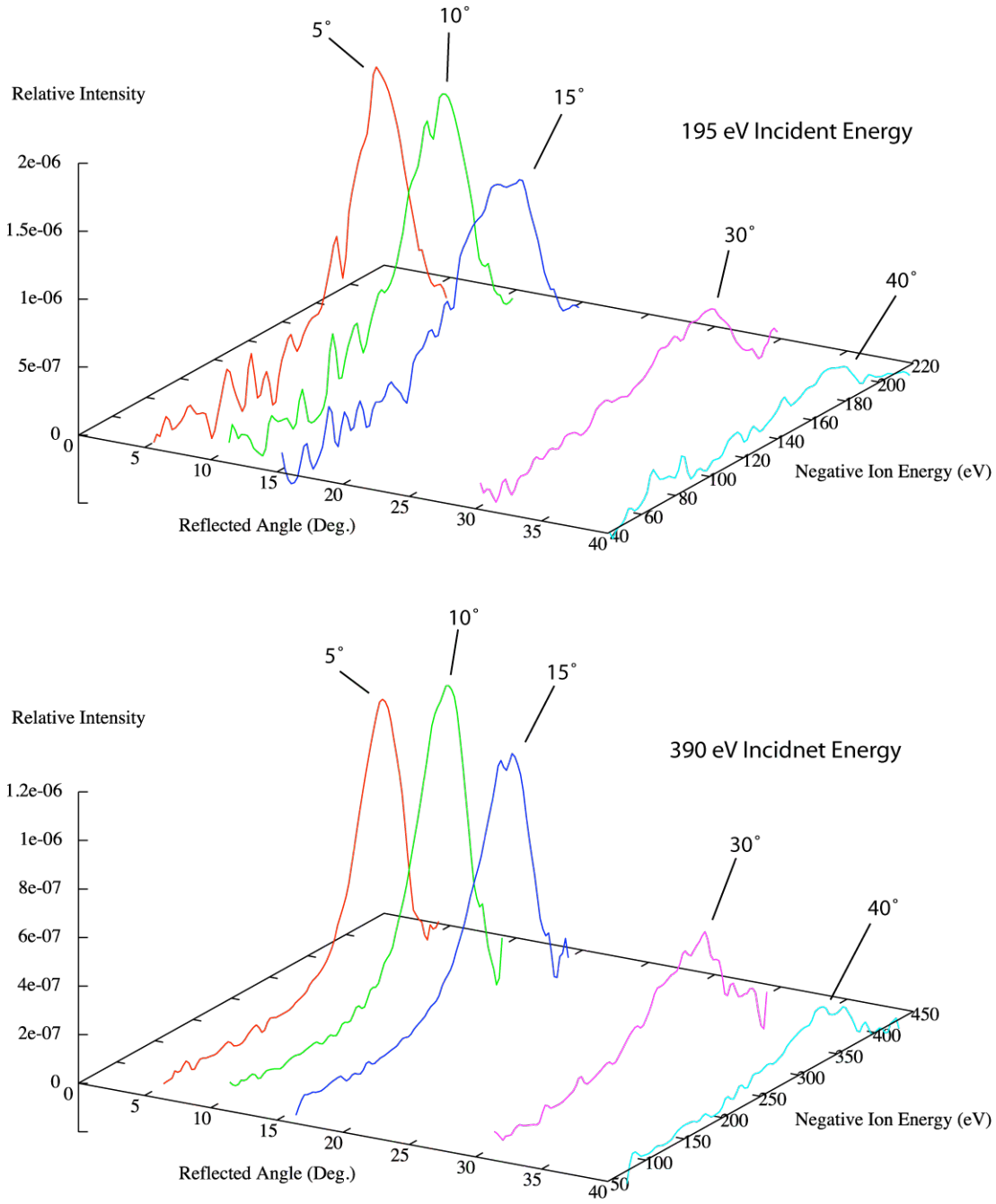

Figure 5.24: Negative ion energy distributions for the DLC surface taken at different angles of reflection with respect to the surface. The incident H beam is at 10° with respect to the surface

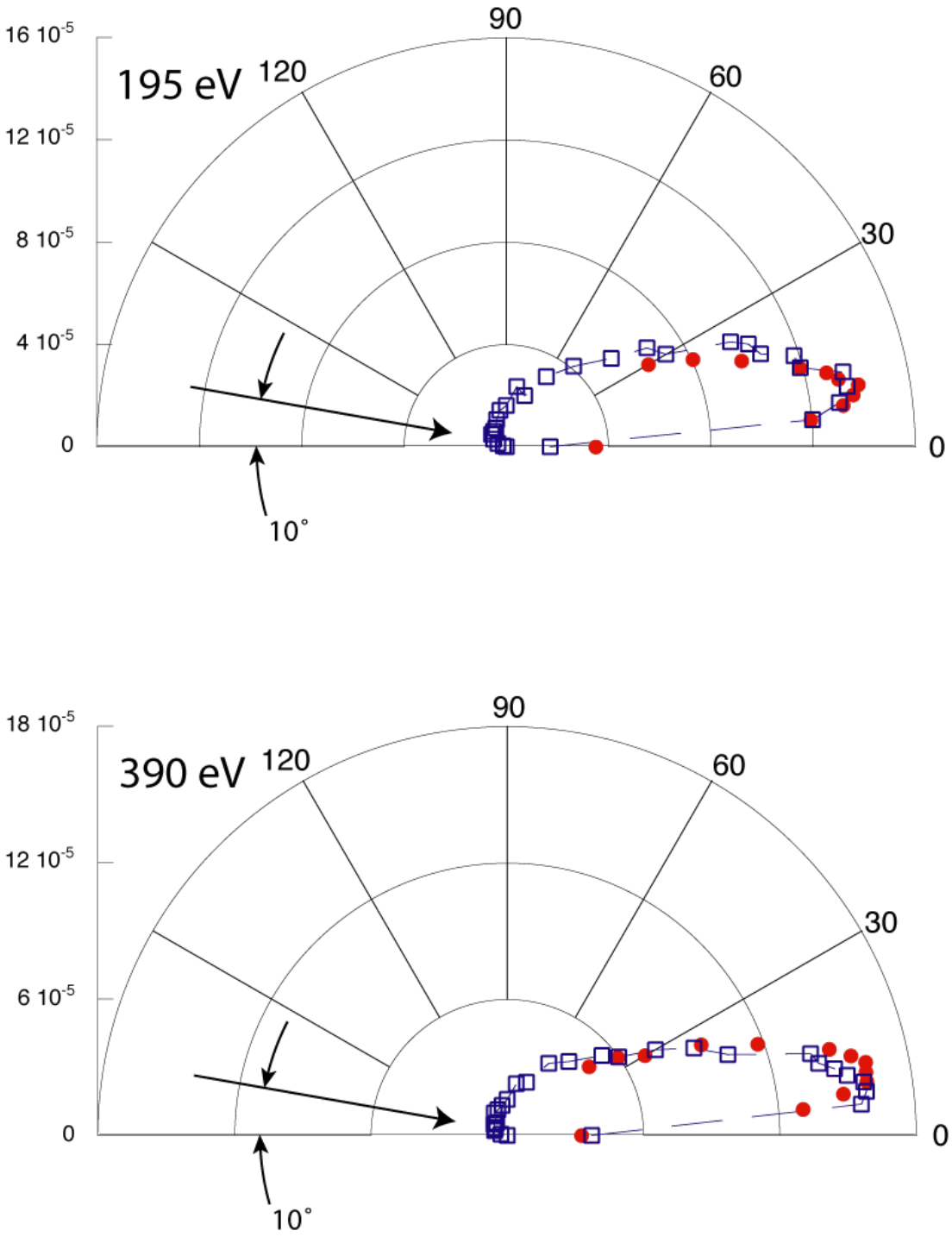

Figure 5.25: Angular distributions of H^- ions reflected from the DLC surface. The H beam is incident at 10° to the diamond like carbon surface. The measured data (•) and the scaled SRIM simulations (□) are shown.

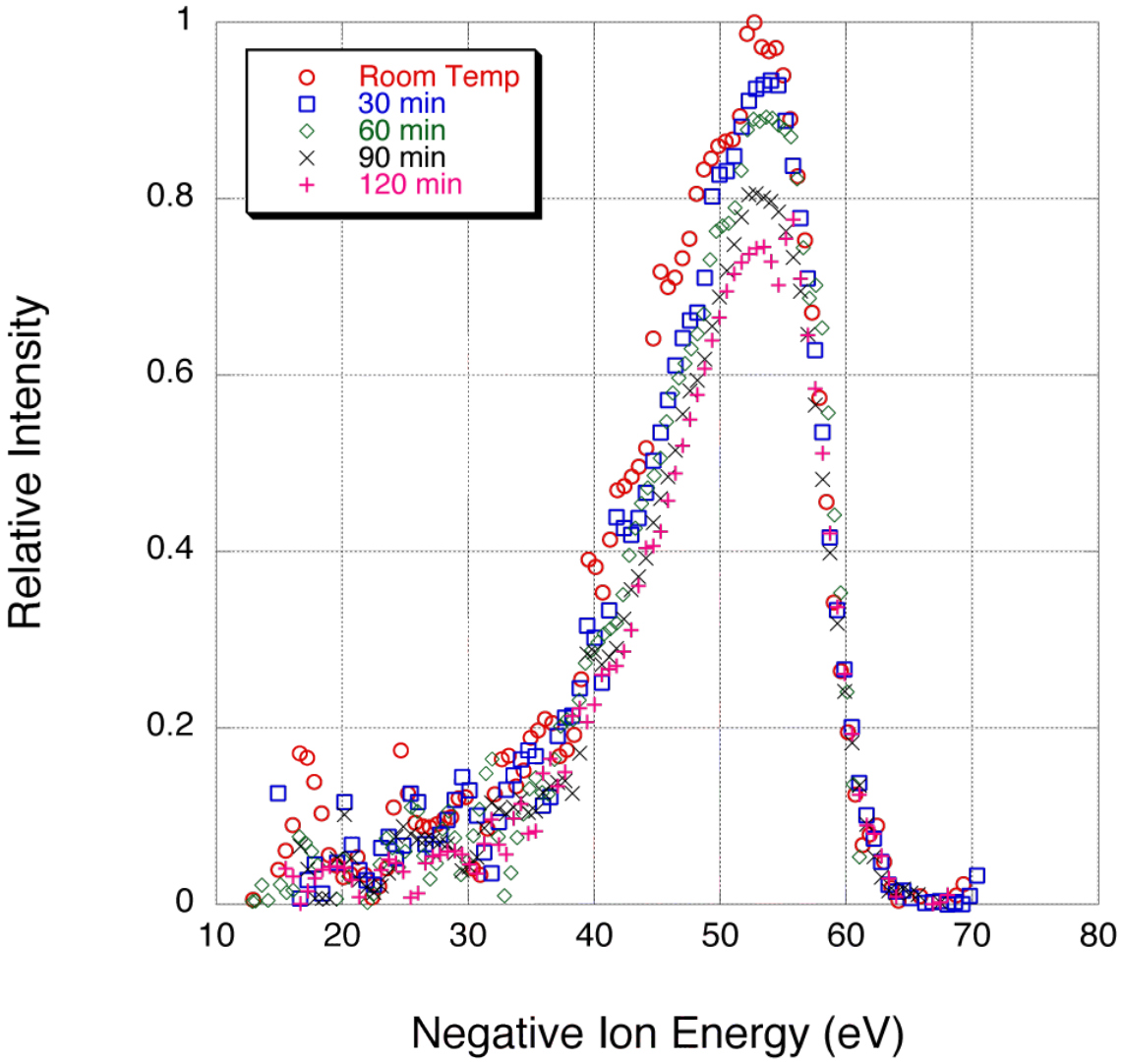

Figure 5.26: Energy distributions for the DLC surface at different temperatures. The stage attained a temperature of 300℃ at t = 0. Measurements were taken at time intervals of 30, 60, 90 and 120 minutes after t = 0. The incident H beam energy was 65 eV and the incident and reflected angles were 10° to the surface.

measure the different angles and energies of negative ions but allows for comparative measurements of conversion efficiency among surfaces for the same incident neutral energy and negative ion scattering angle with respect to the surface. Statistical uncertainties of the apparent conversion efficiency from the measurements of count rates are no more than 5% for the 400 and 500 eV incident beam energies. The major source of error in the lens measurements is due to mechanical instability shifting the lens elements while changing the samples. As previously stated (see page 51), the lens collects negative ions reflected from the surface over a limited angle and energy range when the power supply is set to the optimal voltage. Moving the different lens elements or the detector position will change the optimal voltage setting and acceptance range of the lens. The experimental errors were estimated by repeating measurements on the tungsten surface while testing the other surfaces. The conversion efficiencies measured on the tungsten surface for different tests are within ± 20%.

5.2.1 Lens Data

The first data on the UMCP system were taken at an incident neutral beam angle of 7.5° to the surface (Table 5.2) for tungsten, DLC, HOPG, the Si n-type and Optotechnik Sjuts. The beam energies were 100 eV, 250 eV and 500 eV. All of the surfaces with the exception of the Optotechnik Sjuts surface show a higher conversion efficiency than tungsten. The Sjuts surface at all energies, and HOPG under a 100 eV incident neutral beam, show conversion efficiencies equivalent to

tungsten to within the uncertainty of the measurement. The Si n-type was about twice as efficient as tungsten for all beam energies. For the 500 eV beam, HOPG had the highest conversion efficiency, almost three times that of tungsten. At 100 and 250 eV incident energies, silicon had the highest relative conversion efficiency.

A second set of data were taken with the incident beam at 11.25° to the surface. Table 5.3 (under the RmTp headings) shows the conversion efficiencies of the surfaces relative to tungsten for the 11.25° incident beam angle. The neutral beam energies used were 100 eV, 200 eV and 400 eV. All of the previously tested surfaces as well as CNS, CNT, platinum, gold, silver and the Si p-type were tested at this angle. The HOPG had the highest relative conversion efficiency for these tests. The efficiency was more than two times the tungsten efficiency for 200 eV and 400 eV neutral beam energy, and almost two times for the 100 eV beam. The Sjuts and DLC surface show very little difference in conversion efficiency compared to tungsten. The silver and gold were both about half as efficient as tungsten. The conversion efficiency of platinum varied from being less than tungsten for the 100 eV beam to approximately the same at 400 eV. The two silicon surfaces showed very little difference between them. CNS and CNT had the lowest conversion efficiencies observed of all the surfaces used.

The conversion efficiency of the heated surfaces was also measured for 11.25° incident neutrals. The heated surfaces were tested at incident energies of 100 eV and 200 eV. The samples were heated for 1.5 to 2 hours. This allowed the temperature of the surfaces to reach at least 138℃. Table 5.3 shows the conversion efficiencies for the surfaces relative to heated tungsten (under the Hot label). Table 5.4 shows the

	Ion Source Acceleration Voltage (V)		
Surface	**100**	**250**	**500**
Tungsten	100	100	100
DLC	130	170	190
HOPG	110	160	280
Si n-type	180	220	220
Sjuts	90	110	120

Table 5.2: Relative conversion efficiency of the sample surfaces compared to tungsten, given in percent. Values greater than 100 percent indicate an improvement over tungsten's conversion efficiency. The neutral beam is incident at 7.5° to the surface.

relative conversion efficiency of the heated and unheated surfaces. Most surfaces show a decrease in conversion efficiency when they are heated, except for silver, which showed a slight measured increase at both neutral beam energies and CNS for the 200 eV energy. To within the uncertainty of the measurements no surface had a major change in conversion efficiency. The surfaces were heated to lower temperatures in the UMCP system compared to those at Denver. The results from Denver show much larger changes in efficiency when the stage was heated to 300℃ and above.

Significant improvements over the conversion efficiency of tungsten were seen in the HOPG and silicon samples. The Optotechnik Sjuts lead glass surface efficiency is similar to the efficiency of the tungsten surface at both incident angles at all neutral

	Ion Source Acceleration Voltage (V)				
	100		**200**		**400**
Surface	**RmTp**	**Hot**	**RmTp**	**Hot**	**RmTp**
Tungsten	100	80	100	80	100
DLC	100	80	110	90	110
HOPG	190	140	220	130	220
CNS	0	0	0	0	10
CNT	0	0	0	0	0
Platinum	70	20	80	20	100
Gold	40	20	40	20	60
Silver	40	50	50	50	60
Si n-type	130	130	140	140	160
Si p-type	120	100	150	140	160
Sjuts	110	80	110	90	110

Table 5.3: Relative conversion efficiency of the sample surfaces compared to tungsten, given in percent. Numbers greater than 100 percent indicate greater conversion efficiency than tungsten. The incident neutral beam is at 11.25° to the surface and the data are for the surface at room temperature (RmTp) and heated to at least 138℃ (Hot). The measurements are relative to the room temperature tungsten surface.

	Ion Source Acceleration Voltage (V)	
Surface	**100**	**200**
Tungsten	80	80
DLC	80	90
HOPG	70	60
CNS	60	100
CNT	60	100
Platinum	30	30
Gold	70	70
Silver	100	110
Si disk	100	100
Si square	90	100

Table 5.4: Ratios of conversion efficiencies for heated and room temperature surfaces. The beam is incident at 11.25° to the surface. In general, conversion efficiency falls when the surface is heated, silver is an exception.

beam energies. The DLC surface showed a difference between the two angles of incidence. At 7.5° the efficiency is more than tungsten by 30% at 100 eV incident energy and 90% at 500 eV incident energy. At 11.25° the efficiencies for tungsten and DLC are similar. The Denver results give about the same absolute conversion efficiency for the two surfaces, favoring DLC only slightly, within the error margins. The differences may be attributed to the different incident angles. The 7.5° incident angle spreads the beam across the sample surface more than for higher incident angles. The largest samples were the 2 cm diameter disks of tungsten and Si-disk. The other surfaces had less area exposed to the beam so that the beam overfilled the target for the smaller samples.

5.3 Conclusions

The observed work function data for the surfaces do not suggest that the conversion efficiency is aided by a smaller work function, but the measured work functions of the surfaces span only a limited 1.1 eV range (Fig 5.27). The contribution to conversion efficiency cannot be isolated in the present measurements but it is clear that work function alone is not the single factor determining conversion efficiency. To only measure the work function contribution it would take a carefully planned set of surface materials, ones that keep other parameters at least close to constant while having significantly varying work functions. If control of the other surface parameters cannot be attained, a general trend may be measurable using surfaces with work functions that span a large range.

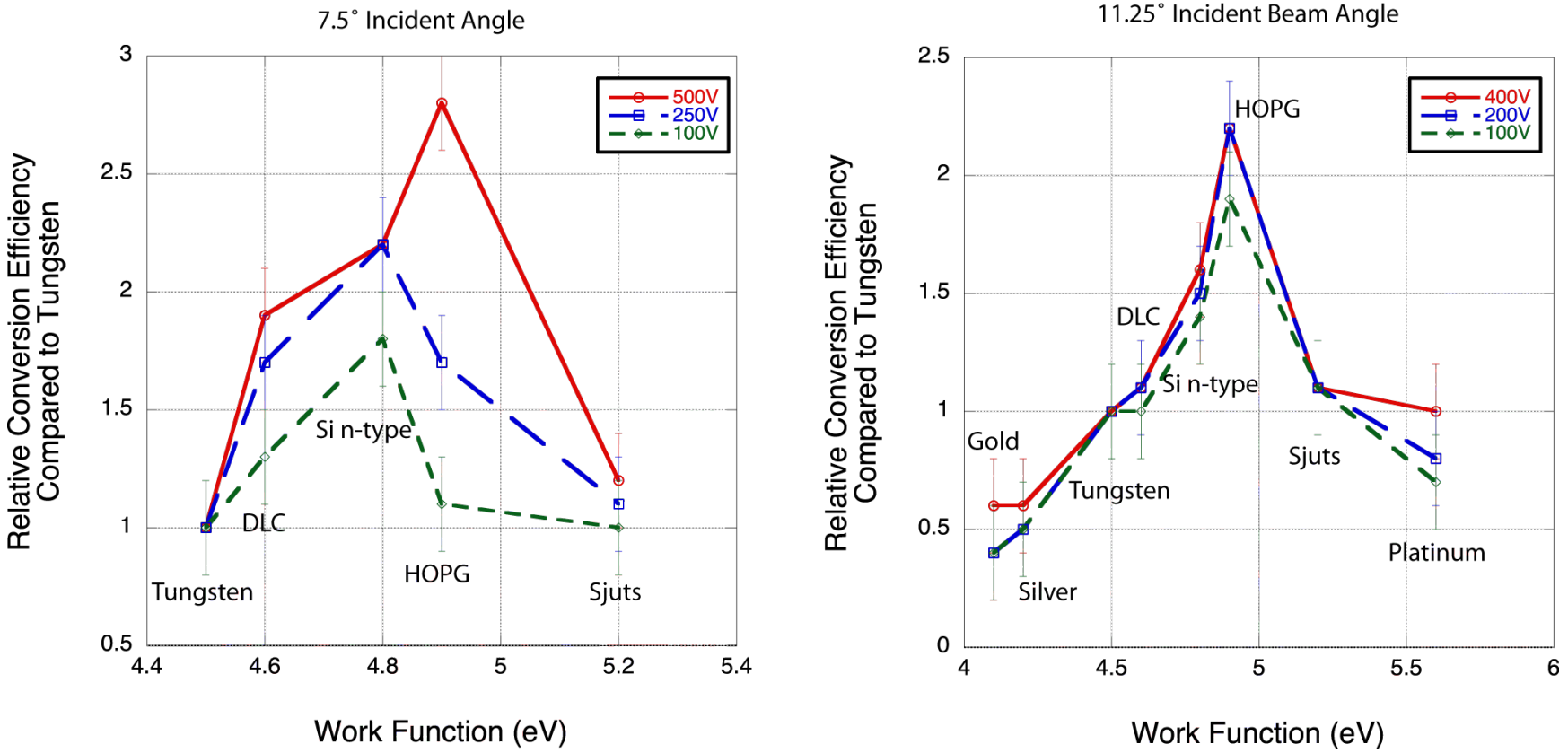

Figure 5.27: The relative conversion efficiencies for the surfaces plotted against the measured work function. The tungsten surface had a work function of 4.5 eV. Work function values a cover small range and changes in the conversion efficiency may be due to surface properties rather than work function differences.

The largest and smallest relative conversion efficiencies are for surfaces composed of carbon. The HOPG and the carbon nanosheet surfaces have very different efficiencies. The main difference between the two surfaces appears to be smoothness. The carbon nanosheet has a measurably rough surface compared to HOPG. Rough surfaces will increase the ranges of angles for the negative ions and energies from the target and decrease the number of backscattered atoms. The carbon nano-tube surface had the lowest conversion efficiency of all the surfaces tested. The high electric fields and electron emission from the protruding nanotubes that can supply electrons to the neutral particles do not appear to increase conversion efficiency. The tangled appearance of the CNT surface (Fig. 4.10) and the low conversion efficiency would suggest that most of the incident neutral beam enters the surface and does not backscatter out. The RMS smoothness of some of the surfaces was measured and compared to the relative conversion efficiency (Fig. 5.28). The HOPG surface was tested after being freshly cleaved for all data shown but some preliminary tests were done before cleaving the surface the first time. The conversion efficiency of the surface increased by 10% after cleaving. Cleaving in this case reduced the bumps and scratches introduced to the surface during shipment and other handling in the lab. For these surfaces, the relative smoothness appears to aid in the conversion efficiency.

Low energy neutral atom detectors can benefit from improved surface conversion orientation and efficiency. The angular distributions of the tungsten surfaces show a general decrease in full width at half maximum for smaller incident angles and higher energies. The intensity of the measured flux from the surface is also

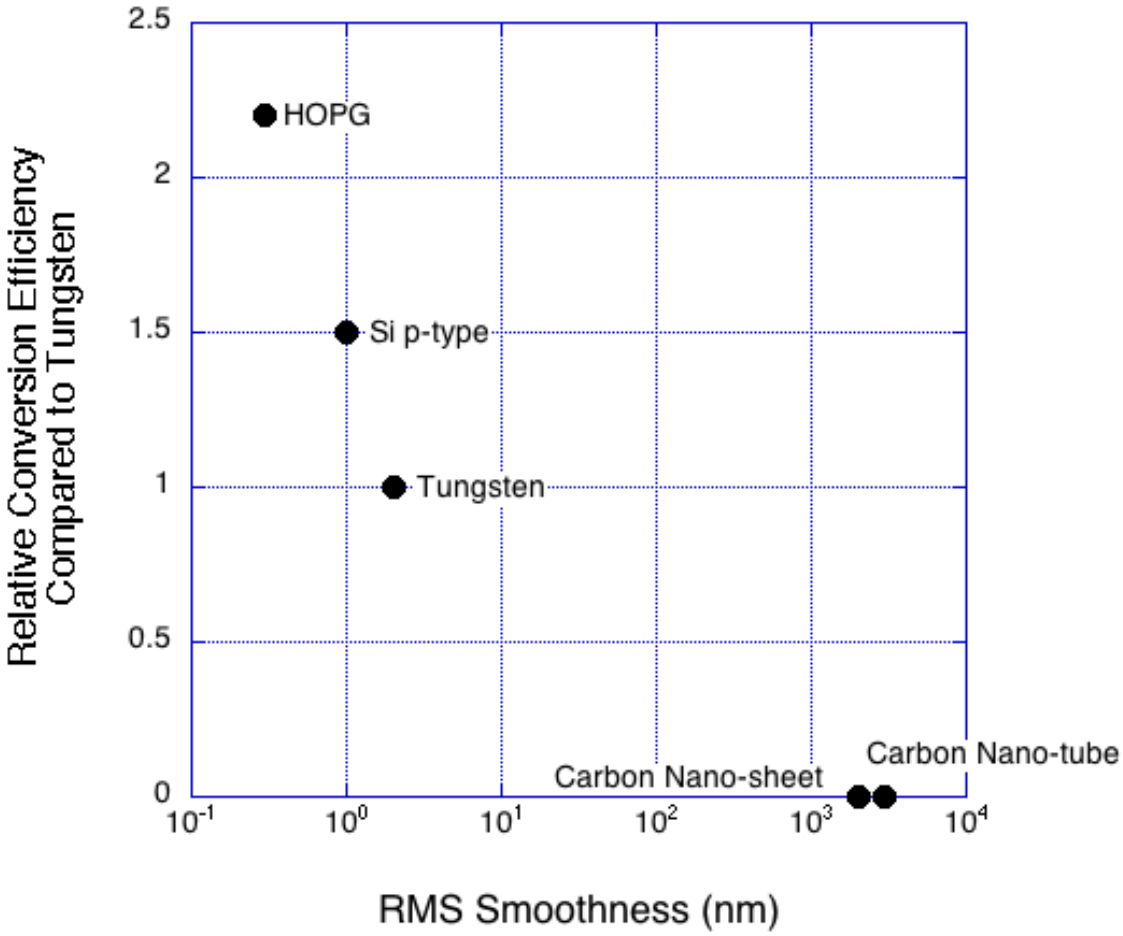

Figure 5.28: Relative surface conversion efficiencies as a function of measured smoothness. The tungsten, carbon nanotube and carbon nanosheet surface smoothness were deduced from SEM and AFM images of the surfaces. The silicon and HOPG surface smoothness was taken from the specifications of the respective manufacturers.

higher for grazing incident angles at 6° and 10°, meaning more negative ions were recorded coming from the surface than the 15° and 20° measurements. The instrument design will dictate what angles the conversion surface will be positioned with respect to incident neutrals but from the angular distribution measurements keeping the incident angle 10° or less will promote surface reflection. The tungsten surface started with an estimated absolute conversion efficiency between 1 to 2%. The HOPG and silicon surfaces displayed the highest conversion efficiencies of the surfaces tested. These increases over tungsten can be used to improve ENA imager resolution. Detector size can be reduced with higher efficiency conversion surfaces and an increase in conversion efficiency by 50 to 100%. Although the measurements in the ion lens were not absolute, comparing them with the tungsten base, assuming the angular distributions for the surfaces do not differ, the silicon surfaces have an overall conversion efficiency between 1.5 and 3% and the HOPG surface had an efficiency between 2 and 4%. Further investigations of surface properties through different materials and preparation are needed to fully evaluate negative ion conversion efficiency.

5.4 Future Work

5.4.1 Ion Lens

Modifications to the ion lens can increase the range of incident energies. Currently the lens cannot operate at a voltage higher than 5 kV due to electrical discharges. This is a result of the close positioning of the plates and the large potential

differences between them. At 5 kV the energy of backscattered negative ions that the lens can collect is limited to a maximum of 500 eV. Redesigning the lens with more space between the plates will allow the system to operate at a higher voltage with fewer discharges contributing to the background noise. By increasing the distance between the target and the detector, lengthening the trajectories of the negative ions the strength of the acceleration field needed to direct the ions into the detector will be decreased. SIMION™ simulations show that this will allow the lens to operate at a lower voltage for the same beam energy than is possible with the current design. Such modifications can be expected to increase the energy range of the lens for negative ions scattered from the test surface to 1000 eV or more.

5.4.2 Neutral Beam

The electron impact ion source used in the UMCP apparatus produces a beam of hydrogen molecular ions that are converted to neutral hydrogen molecules. A source of hydrogen atoms would allow a more direct assessment of the conversion efficiency of surfaces for neutral particle imaging in space. Arc discharge or duoplasmatron ion sources are able to produce atomic beams that can be neutralized and used for incident beams [79]. Combined with acceleration and focusing lenses and a suitable neutralization system such as the method used in the Denver apparatus, a high intensity neutral atom beam is possible. Changing the incident beam from molecules to atoms would be a major project for the system in its current form but would provide results more directly applicable to the intended study. The neutral

beam energy is also not well defined. Apertures could be placed along the beam path to remove low energy neutral particles while letting ions of the required energy pass to charge exchange afterward. This mono-energetic ion beam could then be allowed to charge exchange with the neutral background gas and pass though a charged particle filter before reaching the target chamber.

5.4.3 Particle Detector Calibration

The different detection efficiencies of the CEMs for the incident beam molecules and the scattered negative atoms make absolute conversion efficiency measurements of the surfaces difficult. The detection efficiencies stated previously have been inferred by efficiency experiments on other CEMs and related multichannel plate detectors but not specifically Sjuts Optotechnik CEMs [68, 69]. An absolute calibration of the CEM detectors for the charge state, energy and type of particle being detected can be used to measure conversion efficiency for a test surface without the need to compare it with a base surface. Measuring the efficiency of the beam detector would require a well calibrated low energy (100 to 500 eV) neutral beam and a higher energy negative ion beam (1 keV to 5 keV) and a method of determining the beam flux to compare to the detector measurements.

5.4.4 Conversion Surfaces

Additional surfaces can be tested in the existing lens system. The effects of smoothness on conversion efficiency can be tested using the same base surface with

different roughness. Increasing the characterization of the surfaces would allow the isolation of different surface properties to test the effects on neutral to negative ion conversion. Different surface preparation techniques may also affect the conversion efficiency. For example, the CNS can be created under varying conditions, some of which result in a smoother surface layer that may allow more backscattering of the incident beam.

5.4.5 Angles of Incidence

The connection between the lens assembly and the linear feedthrough is fixed. Incident angles were selected by rotating the 2 3/4 in. flange on the feedthrough and the 12 in. flange on the vacuum chamber to change the incident beam angle. The different rotations were used to produce the 7.5° and 11.25° incident angles used in this set of experiments. Creating a rotatable section in between the lens and feedthrough will increase the range of angles that the lens can be positioned relative to the beam direction. Finding the optimum angle of incidence will enable the instrument design to take full advantage of the conversion properties of the surface used.

Appendix A

Lens Construction

The ion lens used in the experiment was designed to collect negative ions from the target surface and direct them into the detector for counting. This was achieved using electrostatic potentials applied to specially shaped and positioned metal plates. The lens design is derived from the ion collection scheme of the LENA instrument on the IMAGE satellite [49]. This section includes technical design and operation of the ion lens in this experiment. All technical drawing dimensions are in inches unless otherwise noted.

A.1 Lens Plates

The lens consists of a series of eleven plates. The first part of the lens is made up of the back plate, mount plate and target plate which fit together to hold the surface being tested at a grazing angle in the neutral beam path. The next eight plates are a series of four single fin and two double fin plates and end with two detector shield plates. Fig. A.1 shows the SIMION™ view of the lens and an example of the negative ion paths from the conversion surface to the detector.

The lens voltages are supplied by one high voltage source and a voltage divider to give each plate the proper relative voltage. The resistors used in the voltage divider on the inside of the chamber are Ohmite precision thick film planar resistors

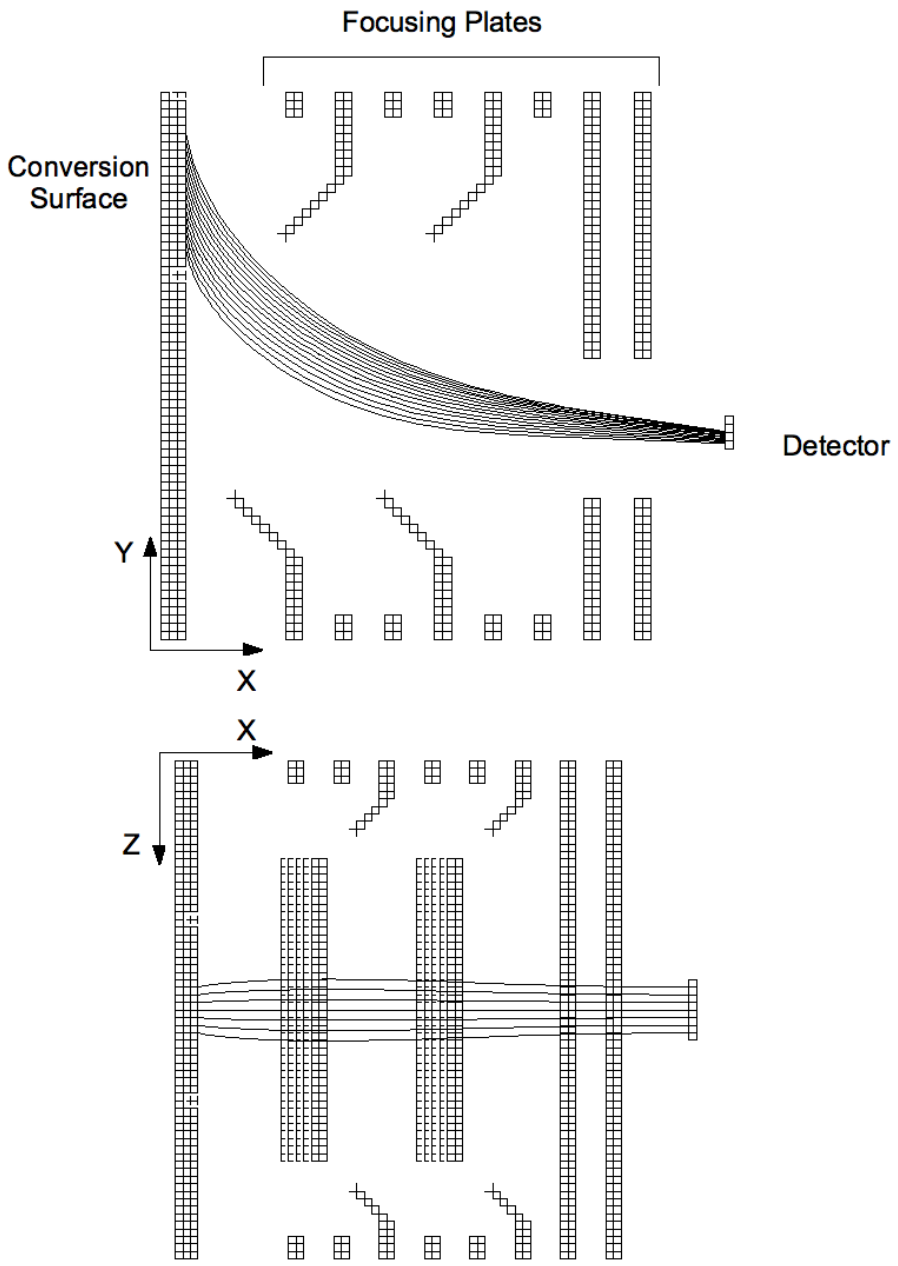

Figure A.1: Views of the lens in SIMION™. The top diagram shows the x-y plane cut where the single fin lens plates shape the electric field to focus the ions. The bottom diagram shows the x-z plane where the double fin lens plates shape the electric field. The curved lines are ion trajectories through the lens. Shown are trajectories of 120 eV ions leaving the conversion surface at an angle of 11.25°. The voltage on the conversion surface is -2 kV; the other lens plate voltages are listed in Fig. A.2.

of 1, 2, 5, 10 and 25 MΩ values. One 6.8 MΩ resistor is used on the outside of the chamber between the lens and the power source for protection in case of shorts or arcing between the connections in the chamber. The voltage divider and examples of the resulting lens plate voltages are listed in Fig. A.2.

Neutral particles enter the lens assembly at a grazing angle to the target surface. Converted negative ions reflected from the surface are collected by the lens. The lens plates guide the negative ions to the detector. The assembled lens is shown in Fig. A.3. Six separate plate designs are used in the ion lens. All were made from 0.036 inch thick 304 stainless steel sheet except for the mount plate and the target plate, they were 0.12 inch thick. The plates were made using wire electric-discharge machining (wire EDM). Fig. A.4 and Fig. A.5 show the mount plate, target plate and the back plate. The mount plate and back plate are set next to each other and are held at the same voltage. The target plate is held by the mount plate and back plate and when put together provide a flat surface. This surface is held at a high negative voltage so that negative ions produced at the surface will be accelerated to the detector. The three tabs on the end of the back plate are used for making electrical connections. The target plate fits into the mount plate and can be screwed into the back plate when the heater is not attached. The surfaces tested in the experiment had a variety of sizes and shapes; target plates were made with appropriate wells to accommodate them.

The next series of six plates in the ion lens are the fin plates. These plates are used to focus the negative ions coming from the target surface. There are single fin and double fin plates. The single fin plates, shown in Fig. A.6, shape the beam in the

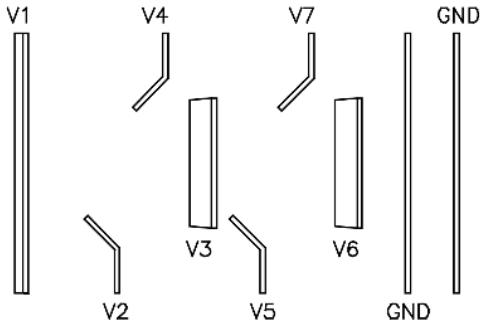

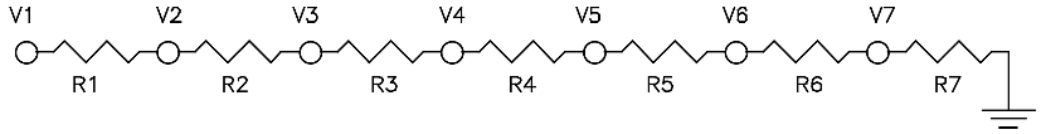

Resistor	Resistance (MΩ)
R1	1
R2	1
R3	2
R4	1
R5	15
R6	5
R7	25

Sample Voltage Settings

High Voltage (kV)	V1 (kV)	V2 (kV)	V3 (kV)	V4 (kV)	V5 (kV)	V6 (kV)	V7 (kV)
1	0.88	0.86	0.85	0.81	0.79	0.53	0.44
2	1.76	1.73	1.69	1.62	1.58	1.06	0.88
3	2.64	2.59	2.54	2.43	2.38	1.58	1.32

Figure A.2: The voltages on the plates of the ion lens are shown along with the resistor chain used to establish the voltages. Lens plate voltages for typical high voltage settings on the first plate are listed.

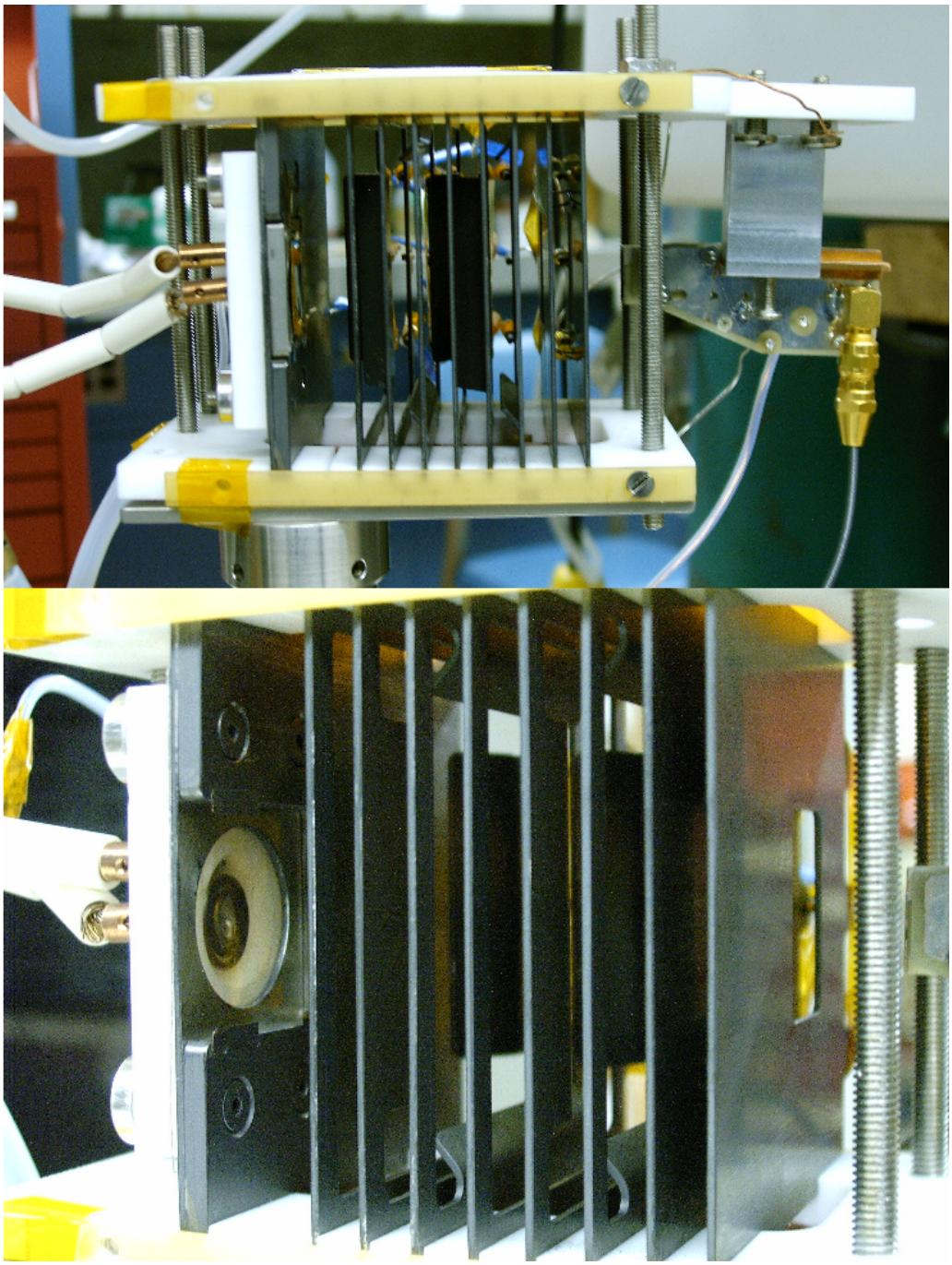

Figure A.3: Pictures of the lens while assembled. The lens usually hangs upside down in the vacuum chamber. Top: The x-z plane of the lens (Fig. A.1) shown with the target plate in place. The detector is located at the right side of the picture. Bottom: Lens with the target plate removed. The heater coil is visible on the left side.

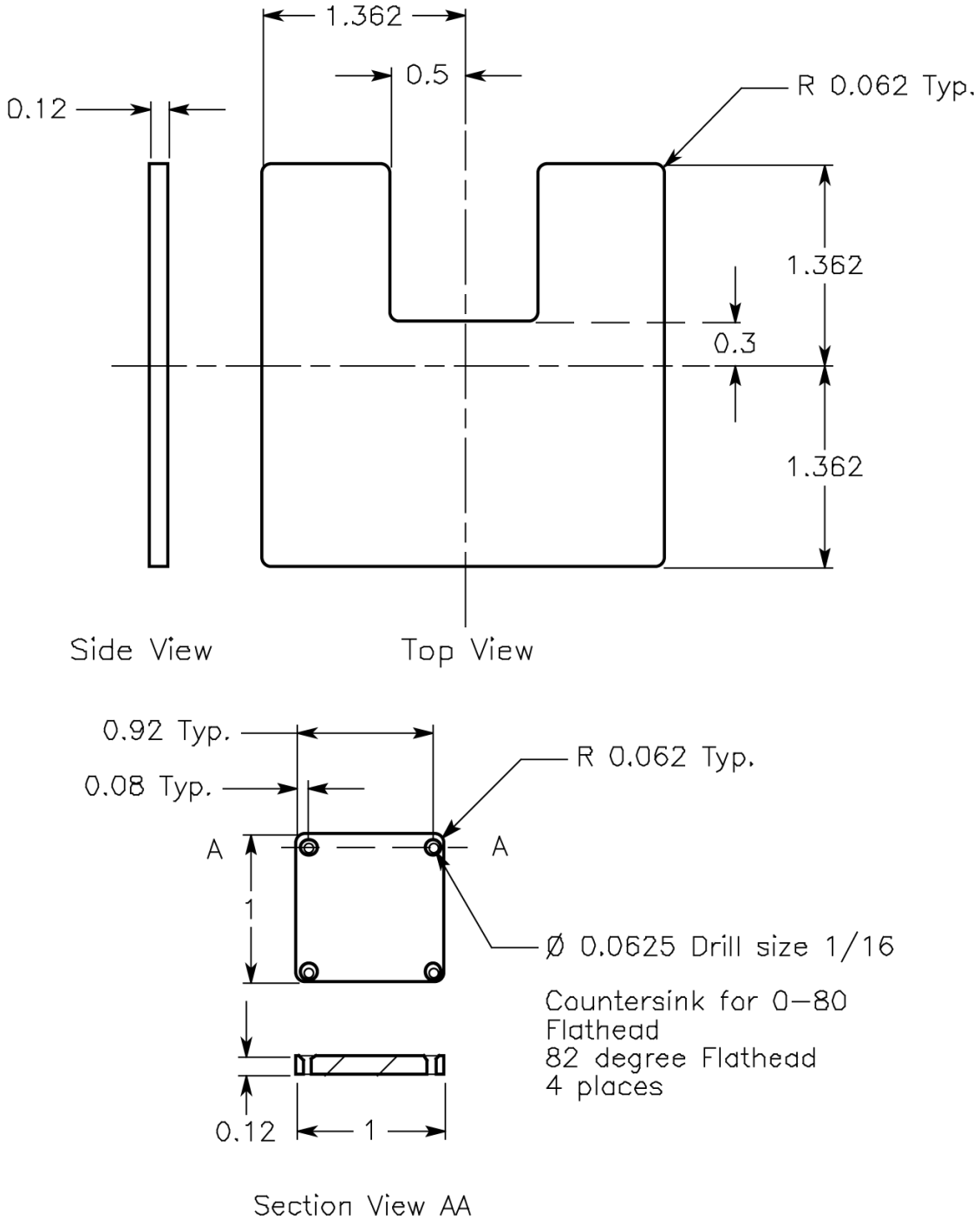

Figure A.4: Mount plate (top) and target plate (bottom) of the ion lens system. The target plate is shown as a blank but in practice had shapes cut into its surface to hold target surfaces of different size and shape.

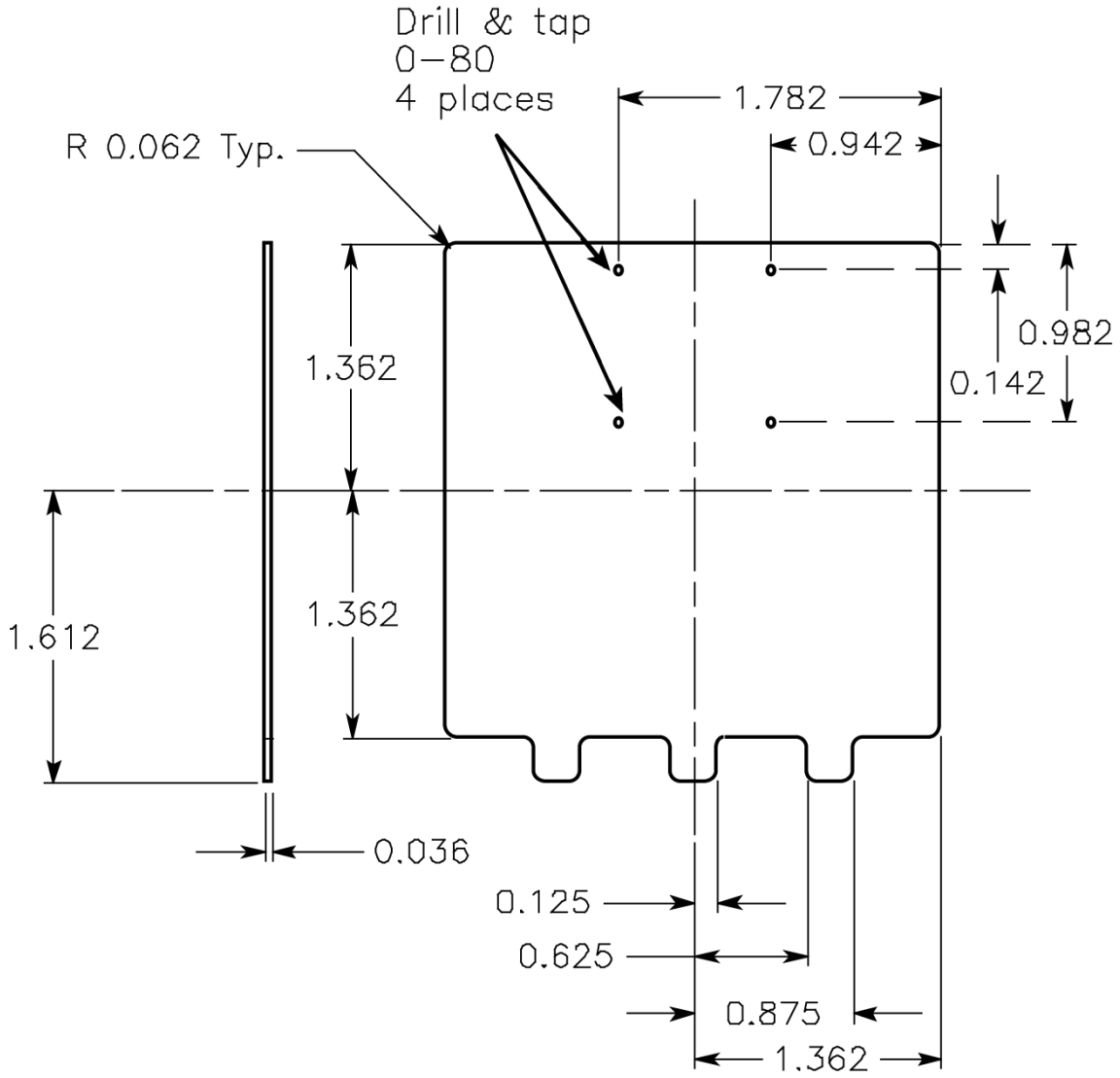

Figure A.5: Back plate. The tapped holes allow the back plate to be attached to the target plate with 0-80 screws.

x-y plane (Fig. A.1 top). The converted negative ions are directed to the detector while neutral particles from the surface are intercepted by the fins on the lens plates and cannot reach the detector. The only difference between the two single fin plates is the location of the electrical connection tabs. The double fin plates (Fig. A.7 top) are used in the x-z (Fig. A.1 bottom) plane to focus the negative ions into the detector. After the fin plates were cut, the fins were bent forward by 45° along the dashed line in the figures to shape the electric field. The final two plates in the lens are the detector shields (Fig. A.7 bottom). These plates are flat and only have a hole for the converted negative ions from the target to pass through to the detector.

A.2 Lens Assembly, Operation

The lens plates are held in place by two grooved Teflon™ plates at the top (Fig. A.8) and bottom (Fig. A.9) of the lens. The plates hold the lens plates 0.2 inches apart and parallel to each other. Side girders (Fig. A.10 top) retain the lens plates in the grooves. The bottom Teflon™ plate also holds the detector mount. The lens is held together with threaded rods through the four holes at the corners of the top and bottom Teflon™ plates. A metal hanger plate (Fig A.10 bottom) is attached to the top teflon board and provides for attachment to the mechanical linear feedthrough on the lid of the vacuum chamber. The feedthrough is used to raise and lower the lens.

Low energy secondary electrons can be emitted from the target surface as the neutral beam impinges upon it. These electrons would then be accelerated into

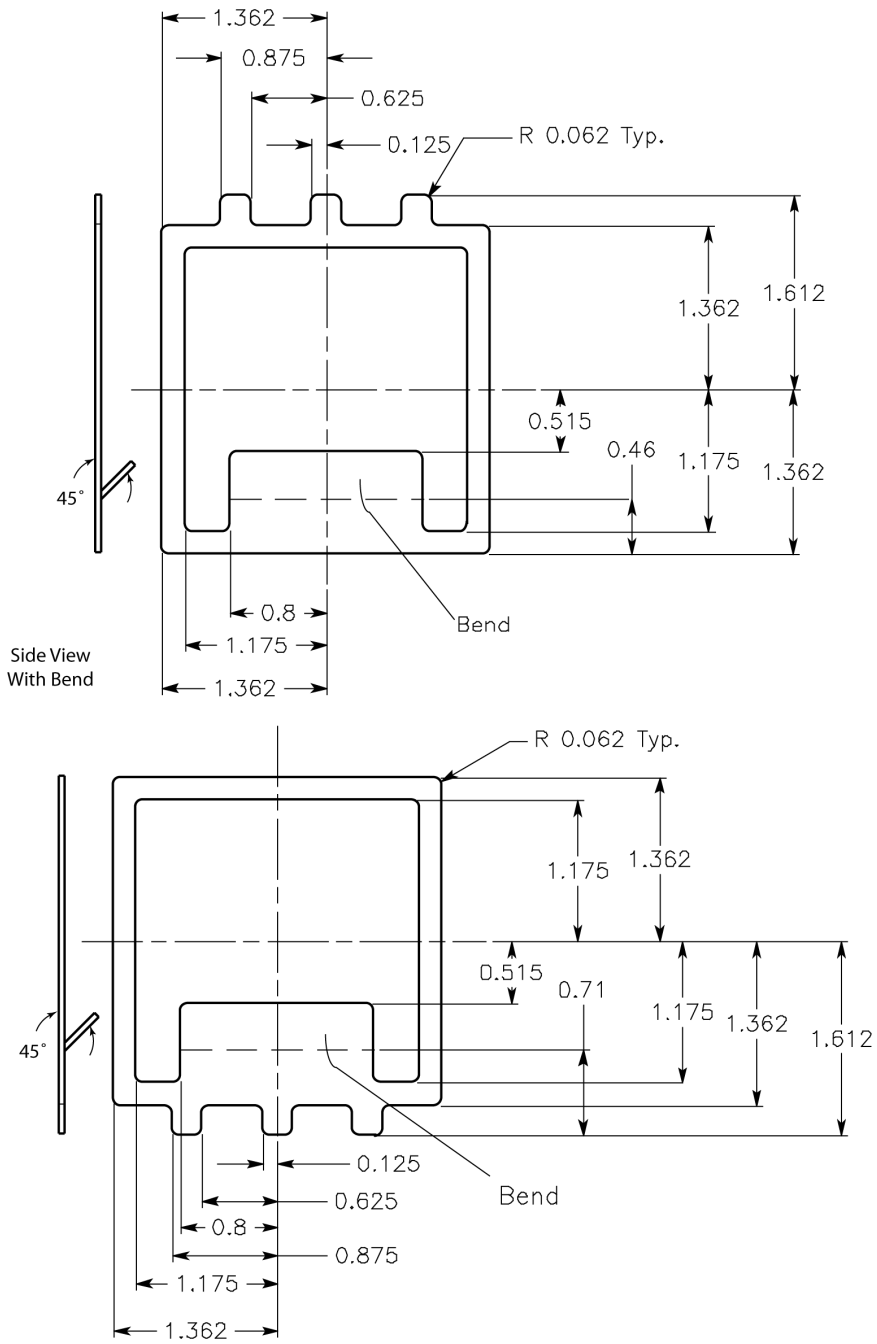

Figure A.6: Two variations of the single fin plate used in the ion lens. The bend line, indicated, is where the fin is bent forward at a 45° angle in order to properly shape the electric field and intercept neutral particles reflected from the surface.

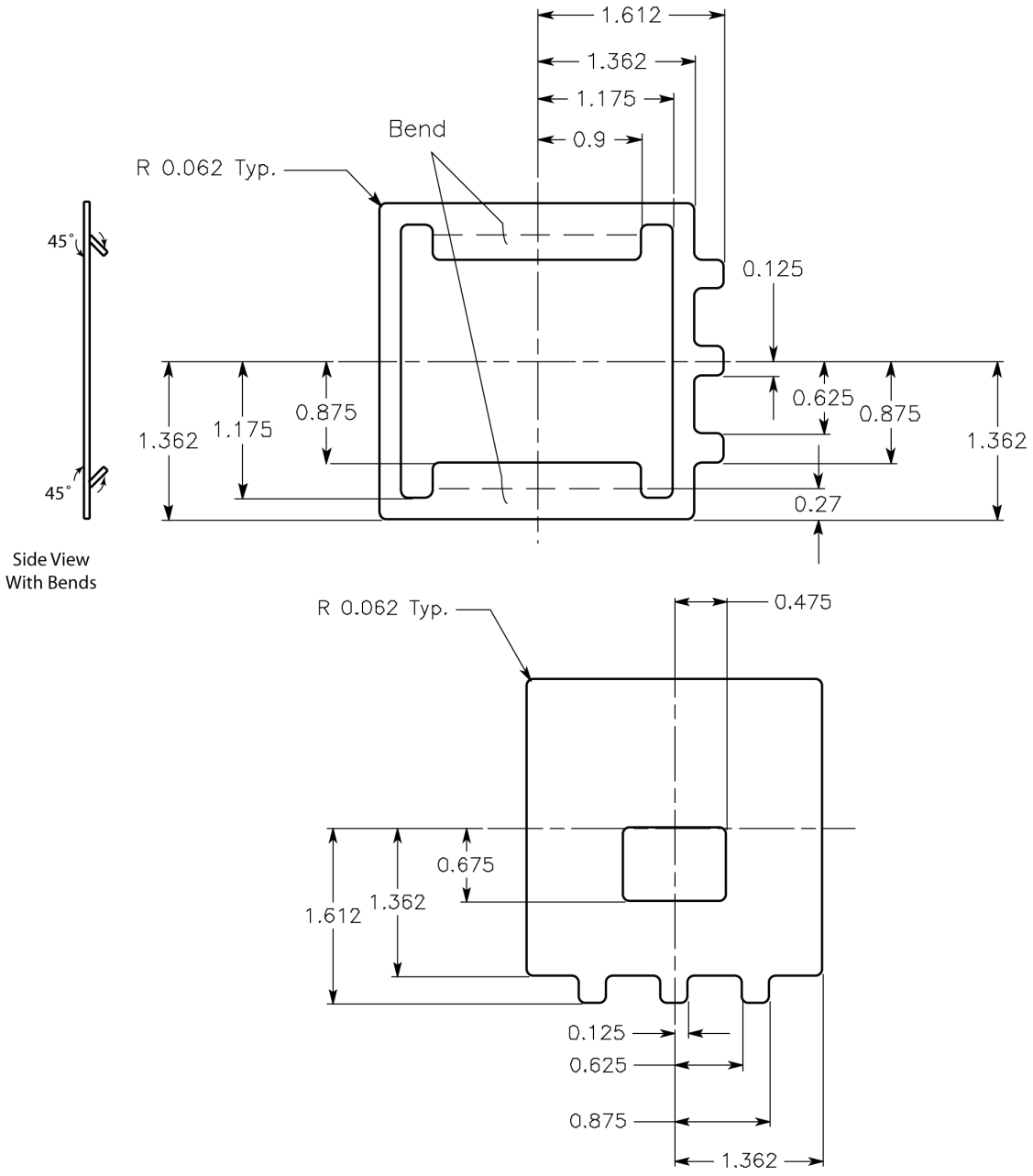

Figure A.7: The double fin ion lens plate (top) and the detector shield plate (bottom) of the ion lens. The double fin plate has both fins bent at a 45° angle.

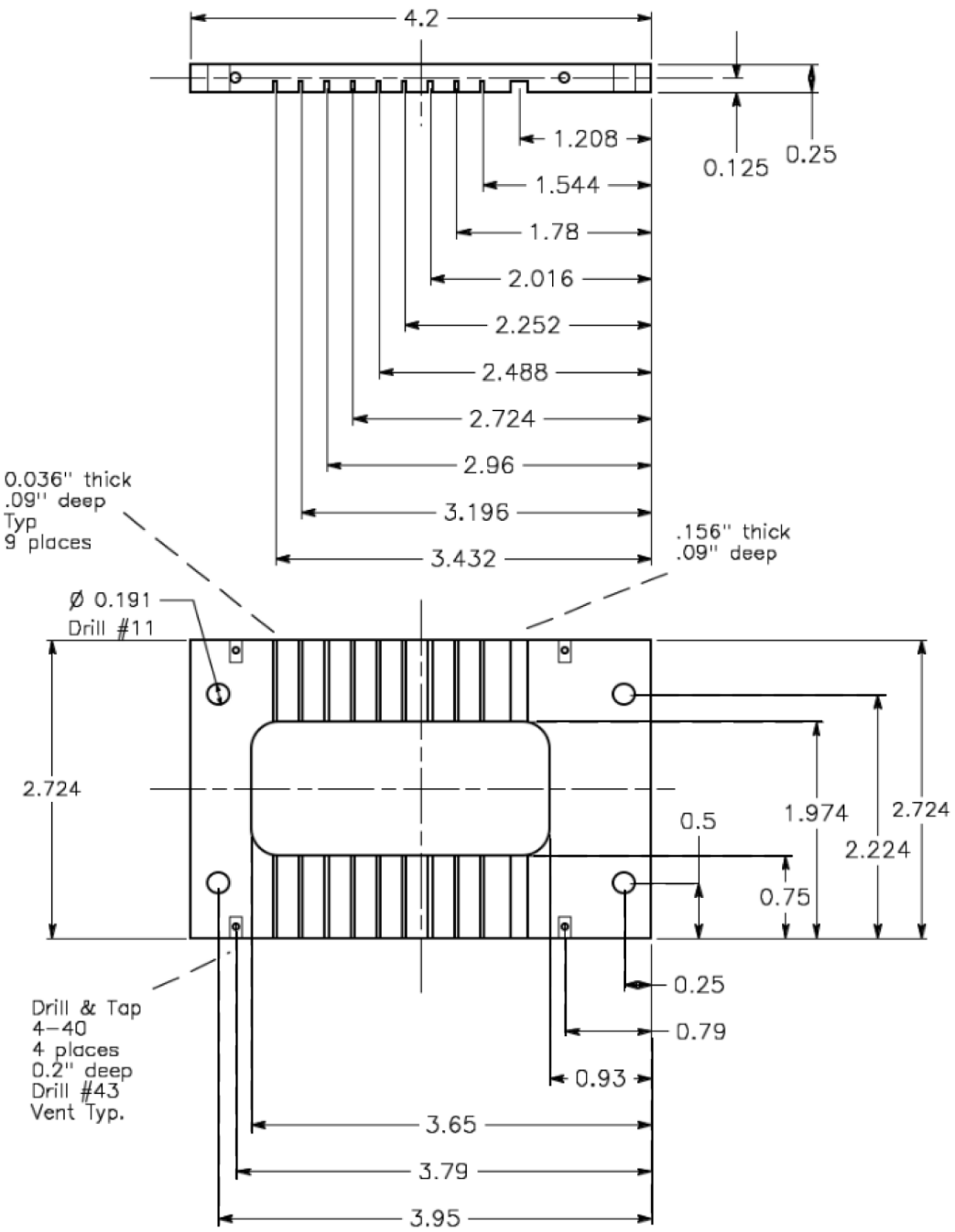

Figure A.8: The top plate of the lens assembly. The plate material is Teflon™. (A scale drawing of indeterminate scale.)

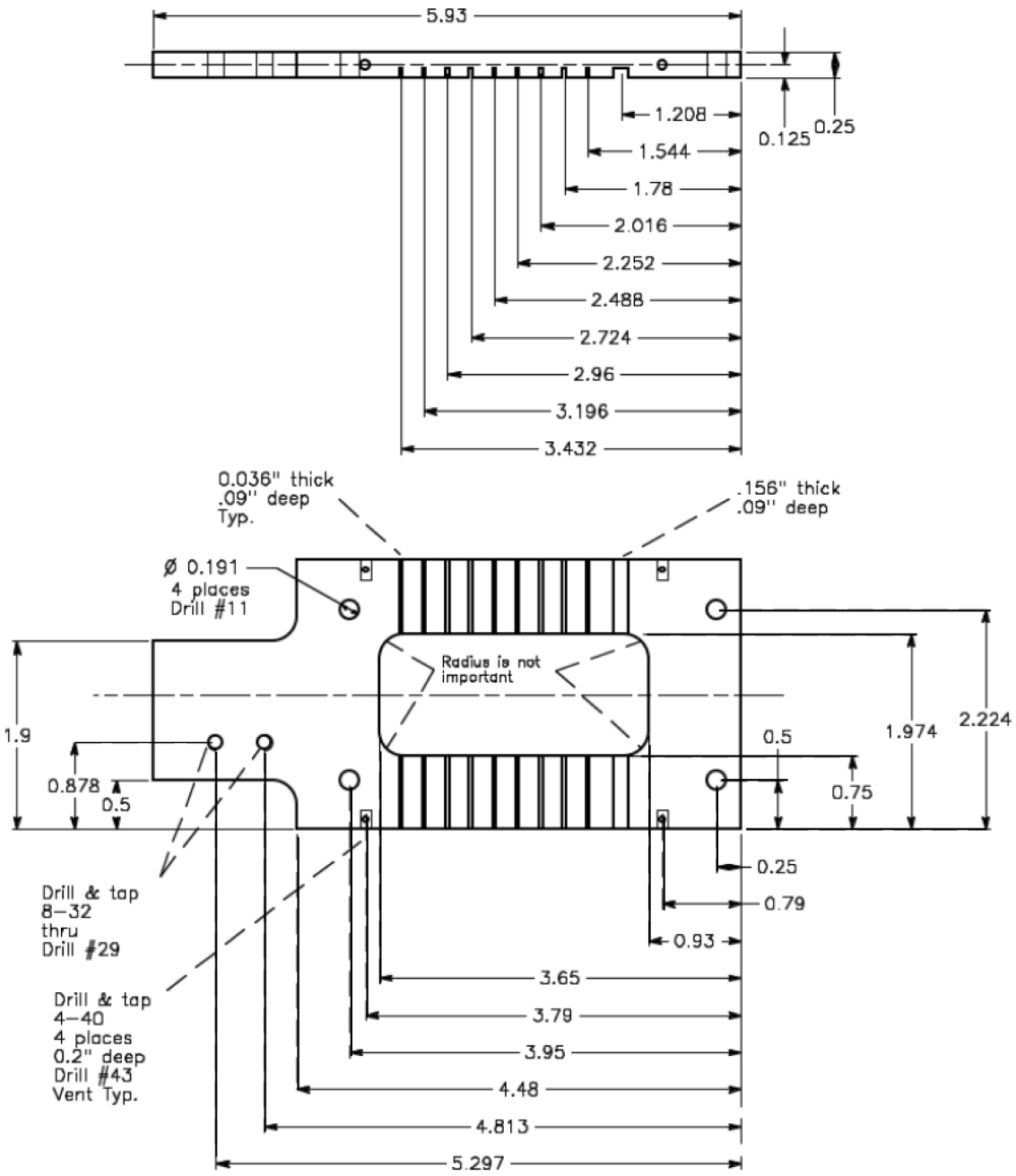

Figure A.9: The bottom plate of the lens assembly. The grooves hold the lens plates. The extension to the left is for mounting the detector. The plate material is Teflon™.

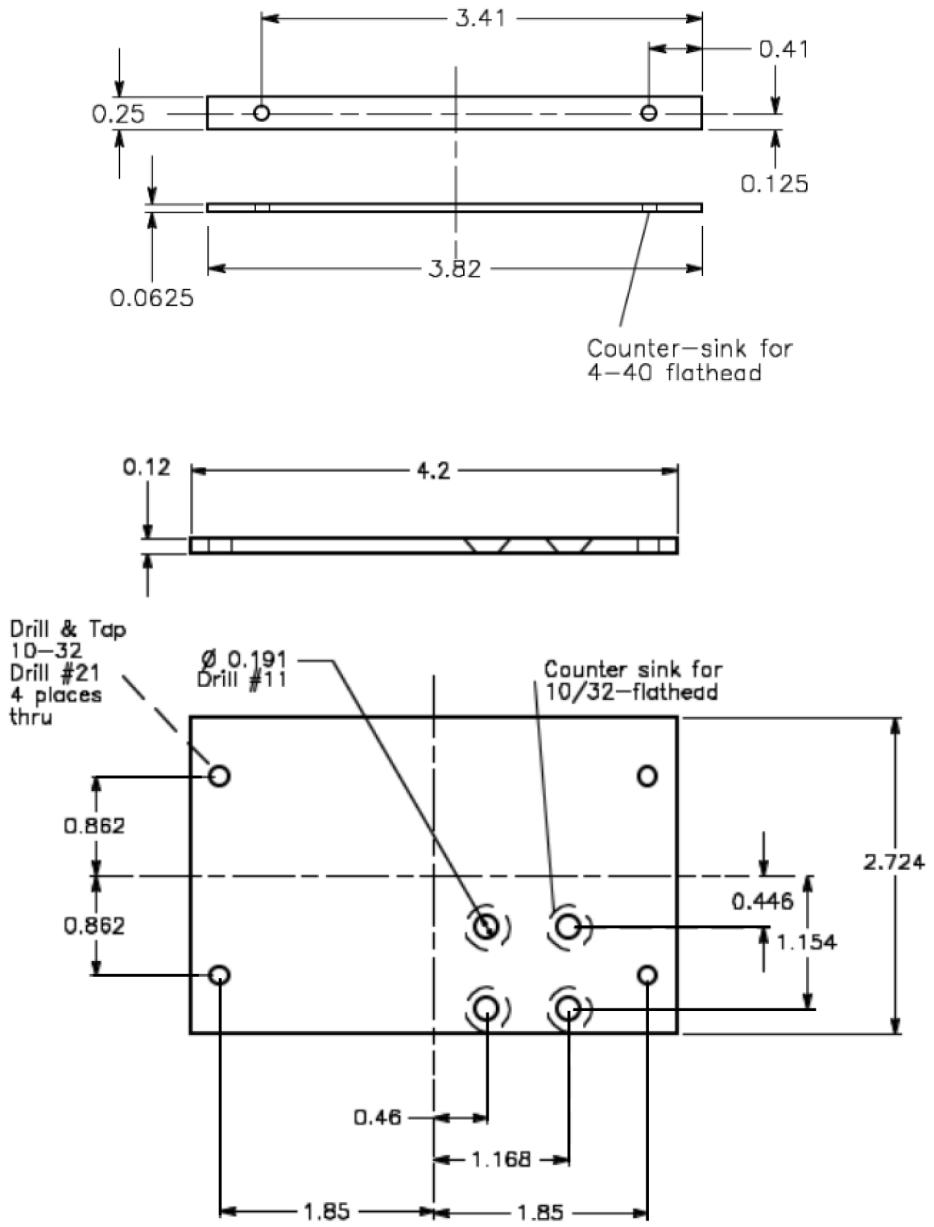

Figure A.10: The side girder (top) and the hanger plate (bottom) of the lens assembly. Four side girders made of Teflon™ are used on the top and bottom Teflon™ plates to contain the metal lens plates. The hanger plate connects the lens to the linear feedthrough and is made from 304 stainless steel.

the lens plates resulting in more secondary electrons that could reach the detector. This electron emission from the lens plates was reduced by coating the metal surfaces with colloidal graphite, a material with a low secondary electron emission coefficient. The voltages placed on the lens plates and the close proximity of the metal plates and resistor chain can cause arcing between the elements that can saturate the CEM detector with emitted electrons. Kapton™ tape and sheets were used to electrically isolate different resistor connections to eliminate arcing. A Kapton sheet is also placed between the Teflon™ top board and the hanger plate to eliminate arcing between the hanger and the lens plates through the hole in the top board. A ribbon of Kapton™ was threaded through the resistor wires on the lens. The addition of the Kapton™ allowed the lens to operate up to 6 kV. Electrons from the lens to the detector were further reduced by setting neodymium iron boride (NdFeB) magnets into the hollow sections of the lens boards on the top and bottom. The magnets measured 5.1 cm $\times$1.3 cm $\times$0.3 cm and were grade N38 from K&J Magnetics. The magnetic fields in the lens were measured with a gauss meter using a transverse probe. The field was 100 G at the central portion of the lens along where the trajectories of the negative ions and 150 G closer to the sides of the near the surfaces of the magnets. The electron trajectories in the lens with the magnets were modeled using SIMION and showed that electron trajectories could not reach the detector (Fig. A.11), while the trajectories of the negative ions were unaffected by the magnetic field.

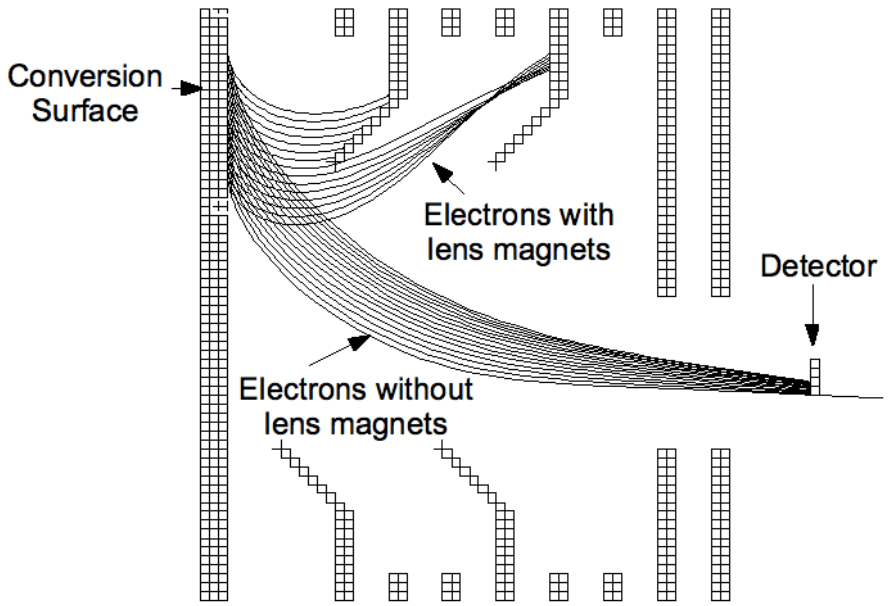

Figure A.11: Simulated electron trajectories for the lens with and without the magnets in place. The electrons are leaving the surface with 120 eV at 11.25°. The potential on the conversion surface is -2 kV. With no magnets the electrons are able to reach the detector. With the magnets, the electron trajectories curve upwards into the lens plates and cannot reach the detector.

A.3 Sample Heating

A tungsten heating coil was added to the back plate directly behind the target plate to heat the sample. The coil is a 2.5 turn spiral of 0.040" tungsten wire (Kurt J. Lesker Company part no. EVSME14040W). The coil is held in position by a machined block of glass-mica ceramic (Macor™) that is fixed to the mount and back plate of the lens (Fig. A.12 and A.13) behind the conversion surface. The heater coil is electrically isolated from the test surface and lens plates by a sheet of muscovite mica placed between the back plate and the heater holder. The coil is connected to a Hewlett Packard 6652A DC Power supply by 14 gauge wires and an electrical feedthrough on the vacuum chamber.

The heater was tested in vacuum using a blank target plate and color change temperature sensitive labels purchased from TIP TEMPerature Products (product number TLCSEN050). The labels consisted of 5 single use color change indicators set to change at 116℃, 121℃, 127℃, 132℃ and 138℃. The manufacturer stated accuracy is ±1%. The heater was tested using 17A and the blank target plate reached between 116℃ and 121℃ after 45 minutes of heating and 138℃ after 1 hour.

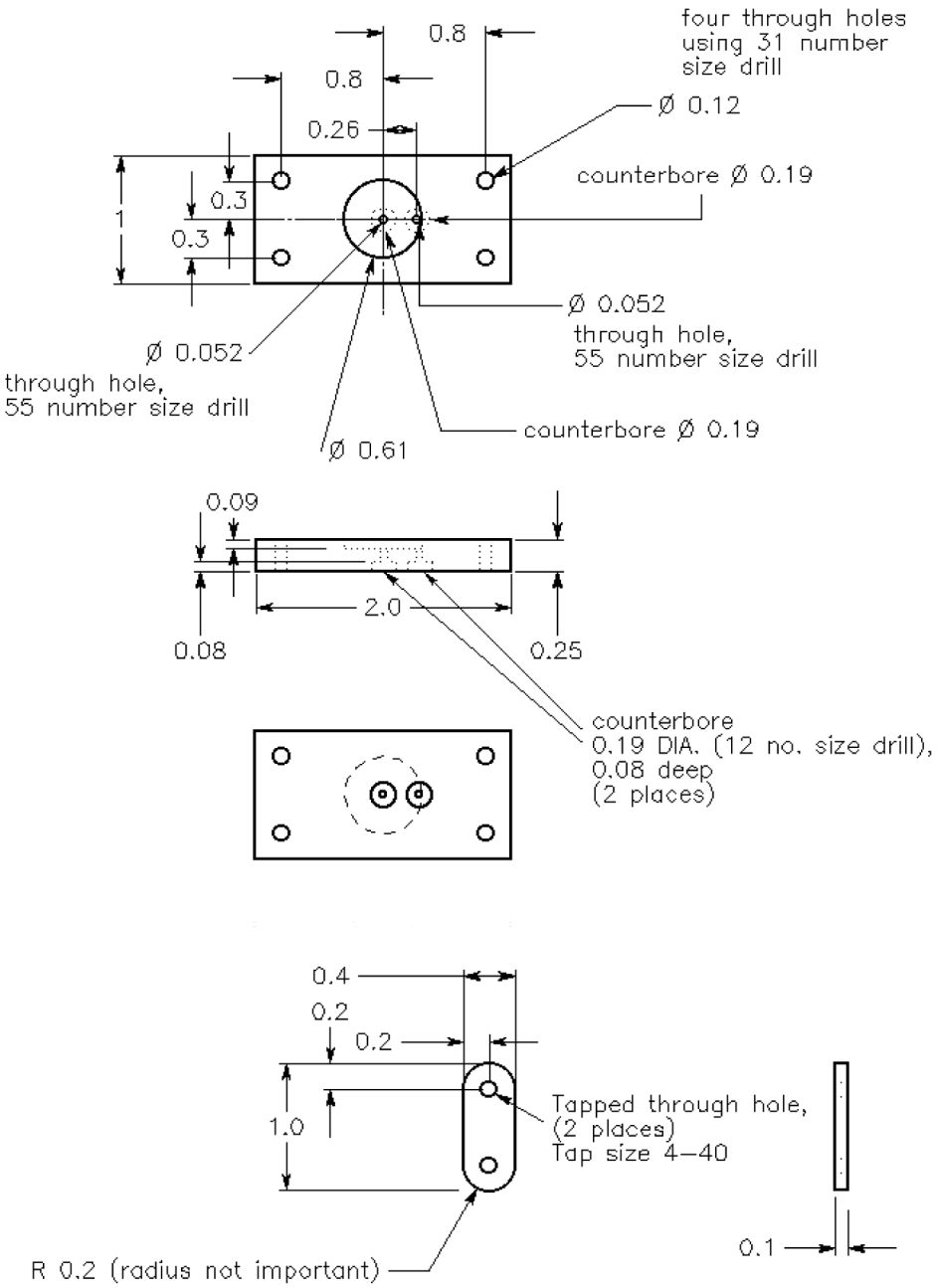

Figure A.12: The Macor™ heater holder (top). The heater coil is placed in the circular well cut into the heater holder and faces the back plate. The screw plates (bottom) secure the heater holder to the lens. The screw plate material is 304 stainless steel. All dimensions are in inches.

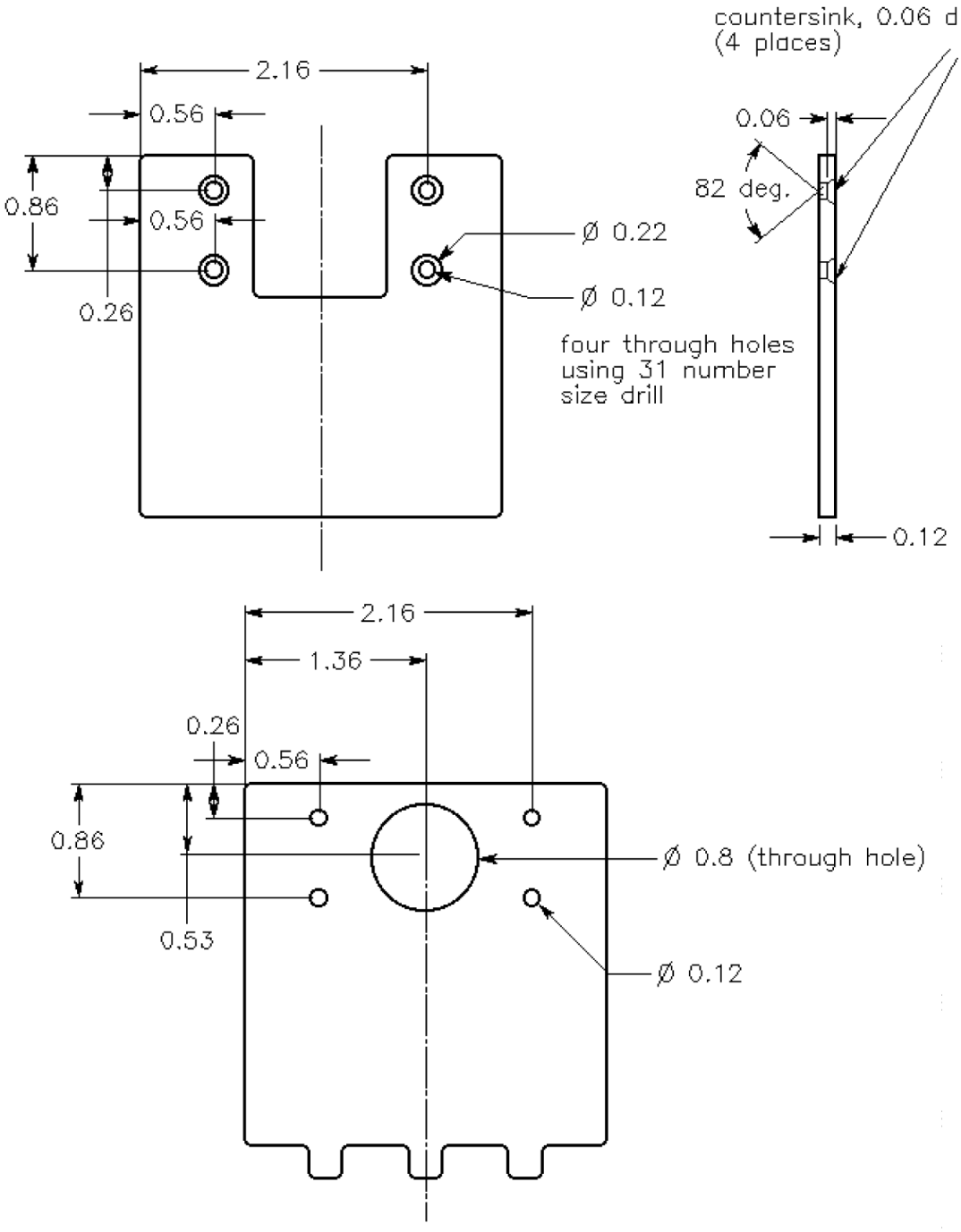

Figure A.13: The Mount (top) and Back plate (bottom) of the lens assembly modified to hold the heater. All dimensions are in inches.

Bibliography

[1] M. A. Gruntman. Energetic neutral atom imaging of space plasmas. *Rev. Sci. Instrum.*, **68**:3617, 1997.

[2] M. Kallenrode. *Space Physics*. Springer, New York, 3rd edition, 2004.

[3] F. Six. What is the magnetosphere. http://science.nasa.gov/ssl/pad/sppb/edu/magnetosphere/mag5.html, 1996. NASA Marshall Space Flight Center.

[4] B. Barbier and S. Mitchell. Cosmicopia. http://helios.gsfc.nasa.gov/heliosph.html, 2006. NASA Goddard Space Flight Center.

[5] D. J. Williams, E. C. Roelof, and D. G. Mitchell. Global magnetospheric imaging. *Rev. Geophys.*, **30**:183, 1992.

[6] D. G. Mitchell, S. E. Jaskulek, C. E. Schlemm, E. P. Keath, R. E. Thompson, B. E. Tossman, J. D. Boldt, J. R. Hayes, G. B. Andrews, N. Paschalidis, D. C. Hamilton, R. A. Lundgren, E. O. Tums, P. Wilson IV, H. D. Voss, D. Prentice, K. C. Hsieh, C. C. Curtis, and F. R. Powell. High energy neutral atom (HENA) imager for the IMAGE mission. *Space Sci. Rev.*, **91**:67, 2000.

[7] C. J. Pollock, K. Asamura, J. Baldonado, M. M. Balkey, P. Barker, J. L. Burch, E. J. Korpela, J. Cravens, G. Dirks, M. C. Fok, H. O. Funsten, M. Grande, M. Gruntman, J. Hanley, J. M. Jahn, M. Jenkins, M. Lampton, M. Marckwordt, D. J. McComas, T. Mukai, G. Penegor, S. Pope, S. Ritzau, M. L. Schattenburg, E. Scime, R. Skoug, W. Sprugeon, T. Stecklein, S. Storms, C. Urdiales, P. Valek, J. T. M. Van Beek, S. E. Weidner, M. West, M. K. Young, and C. Zinsmeyer. Medium energy neutral atom (MENA) imager for the IMAGE mission. *Space Sci. Rev.*, **91**:113, 2000.

[8] M. A. Gruntman. A new technique for in situ measurement of the composition of neutral gas in interplanetary space. *Planet. Space Sci.*, **41**:307, 1993.

[9] J. J. C. Geerlings, P. W. van Amersfoort, L. F. Tz. Kwakman, E. H. A. Granneman, J. Los, and J. P. Gauyacq. H^- formation in proton-metal collisions. *Surf. Sci.*, **157**:151, 1985.

[10] P. W. van Amersfoort, J. J. C. Geerlings, L. F. Tz. Kwakman, A. Hershcovitch, E. H. A. Granneman, and J. Los. Formation of negative hydrogen ions on a cesiated W(100) surface; the influence of hydrogen implantation. *J. Appl. Phys.*, **58**:3566, 1985.

[11] P. J. Schneider, K. H. Berkner, W. G. Graham, R. V. Pyle, and J. W. Stearns. H^- and D^- production by backscattering from alkali-metal targets. *Phys. Rev. B*, **23**:941, 1981.

[12] H. Khan, M. R. Collier, and T. E. Moore. Case study of solar wind pressure variations and neutral atom emissions observed by IMAGE/LENA. *J. Geophys. Res.*, **108**:1422, 2003.

[13] T. E. Moore, M. R. Collier, J. L. Burch, D. J. Cornay, S. A. Fuselier, A. G. Ghielmetti, B. L. Giles, D. C. Hamilton, F. A. Herrero, J. W. Keller, K. W. Ogilvie, B. L. Peko, J. M. Quinn, T. M. Strphen, G. R. Wilson, and P. Wurz. Low energy neutral atoms in the magnetosphere. *Geophys. Res. Lett.*, **28**:1143, 2001.

[14] J. F. Ziegler, J. P. Biersack, and U. Littmark. *The Stopping Range of Ions in Solids*. Permagon Press, New York, 1985.

[15] W. D. Wilson, L. G. Haggmark, and J. P. Biersack. Calculations of nuclear stopping, ranges, and straggling in the low-energy region. *Phys. Rev. B*, **15**:2458, 1977.

[16] J. F. Ziegler. Stopping of energetic light ions in elemental matter. *J. Appl. Phys.*, **85**:1249, 1999.

[17] E. Fermi and E. Teller. The capture of negative mesotrons in matter. *Phys. Rev.*, **72**:399, 1947.

[18] B. Rasser, J. N. M. van Wunnik, and J. Los. Theoretical models of the negative ionization of hydrogen on clean tungsten, cesiated tungsten and cesium surfaces at low energies. *Surf. Sci.*, **118**:697, 1982.

[19] N. D. Lang and W. Kohn. Theory of metal surfaces: Induced surface charge and image potential. *Phys. Rev. B*, **7**:3541, 1973.

[20] J. A. Appelbaum and D. R. Hamann. Variational calculation of the image potential near a metal surface. *Phys. Rev. B*, **6**:1122, 1972.

[21] D. Teillet-Billy and J. P. Gauyacq. Resonant electron capture in atom metal collisions: H-Al(111). *Surf. Sci.*, **269**:162, 1992.

[22] J. W. Gadzuk. Theory of atom-metal interactions. *Surf. Sci.*, **6**:133, 1967.

[23] J. Los and J. J. C. Geerlings. Charge exchange in atom-surface collisions. *Phys. Rep.*, **190**:133, 1990.

[24] M. Remy. Theory concerning the interaction of an alkali atom and a metallic surface. *J. Chem. Phys.*, **53**:2487, 1970.

[25] B. Rasser and M Remy. Long range and temperature-dependent interaction between an alkali atom and a metallic surface; applications to surface ionization. *Surf. Sci.*, **93**:223, 1980.

[26] T. H. Boyer. Penetration of the electric and magnetic velocity fields of a non-relativistic point charge into a conducting plane. *Phys. Rev. A*, **9**:68, 1974.

[27] J. N. M. van Wunnik, J. J. C. Geerlings, and J. Los. The velocity dependence of the negatively charged fraction of hydrogen scattered from cesiated tungsten srufaces. *Surf. Sci.*, **131**:1, 1983.

[28] R. Brako and D. M. Newns. Theory of electronic processes in atom scattering from surfaces. *Rep. Prog. Phys.*, **52**:655, 1989.

[29] J. M. N. van Wunnik and J. Los. Resonant charge transfer in atom-metal surface reactions. *Phys. Scr.*, **T6**:27, 1983.

[30] M. Maazouz, L. Guillemot, V. A. Esaulov, and D. J. O'Connor. Electron capture and loss in the scattering of hydrogen and oxygen ions on a Si surface. *Surf. Sci.*, **398**:49, 1998.

[31] M. Maazouz, R. Baragiola, A. Borisov, V. A. Esaulov, S. Lacombe, J. P. Gauyacq, L. Guillemot, and D. Teillet-Billy. H^- formation in the scattering of hydrogen ions on an Al surface. *Surf. Sci.*, **364**:L568, 1996.

[32] M. Maazouz, L. Guillemot, T. Schlatholter, S. Ustaze, and V. A. Esaulov. Electron capture and loss in the scattering of oxygen atoms and ions on Mg, Al and Ag surfaces. *Nucl. Instrum. Meth. Phys. Res. B*, **125**:283, 1997.

[33] R. Schletti P. Wurz and M. R. Aellig. Hydrogen and oxygen negative ion production by surface ionization using diamond surfaces. *Surface Science*, **373**:56, 1997.

[34] J. Scheer, K. Brüning, T. Fröhlich, P. Wurz, and W. Heiland. Scattering of small molecules from a diamond surface. *Nucl. Instrum. Meth. Phys. B*, **157**:208, 1999.

[35] H Verbeek, W. Eckstein, and R. S. Bhattacharya. Negative hydrogen ion formation by backscattering from solid surfaces. *Surf. Sci.*, **95**:380, 1980.

[36] A. G. Borisov and V. A. Esaulov. Negative ion formation in the scattering of atoms and ions from dielectric surfaces. *J. Phys.: Condens Matter*, **52**:R177, 2000.

[37] J. R. Morris, J. S. Martin, J. N. Greeley, and D. C. Jacobs. Surface site dependence to negative ion formation. *Surf, Sci,*, **330**:323, 1995.

[38] G. K. Wertheim, J. E. Rowe, D. N. E. Buchanan, and P. H. Citrin. Valence-band structure of alkali halides determined from photoemission data. *Phys. Rev. B*, **51**:13675, 1995.

[39] C. Auth, A. Mertens, H. Winter, A. G. Borisov, and V. Sidis. Formation of negative ions in grazing scattering from insulator surfaces. *Phys. Rev. A*, **57**:351, 1998.

[40] S. A. Deutscher, A. G. Borisov, and V. Sidis. Formation of negative ions from fluorine projectiles scattered off a MgO(100) surface: Theory. *Phys. Rev. A*, **59**:4446, 1999.

[41] Y. N. Demkov. Charge transfer at small resonant defects. *Sov. Phys.-JETP*, **18**:138, 1964.

[42] S. Ustaze, R. Verucchi, S. Lacombe, L. Guillemot, and V. A. Esaulov. Electron capture and loss processes in the interaction of hydrogen, oxygen, and fluorine atoms and negative ions with a MgO(100) surface. *Phys. Rev. Lett.*, **79**:3526, 1997.

[43] H. Winter, C. Auth, and A. G. Borisov. Formation of negative ions in grazing scattering from a LiF(100) surface. *Nucl. Instrum. Meth. Phys. Res. B*, **115**:133, 1996.

[44] V. V. Okorokov. Coherent excitation of optical spectra of atoms passing through a crystal. *JETP Lett.*, **2**:111, 1965.

[45] K. Kimura and M. Mannami. Resonant coherent excitation of surface channeled ions. *Phys. Rev. A*, **57**:1121, 1998.

[46] R. E. Taylor. Deep inelastic scattering: The early years. *Rev. Mod. Phys.*, **63**:573, 1991.

[47] H. Geiger and E. Mardsen. On a diffuse reflection of α-particles. *Proc. Roy. Soc.*, **82**:495, 1909.

[48] M. A. Gruntman, D. J. Judge, C. C. Curtis, K. C. Hsieh, D. Shenamsky, M. Seidl, A. Chutjian, and O. J. Orient. A new approach to an *In situ* study of neutral atomic fluxes in the solar system. *EOS Trans. AGU*, **44**:393, 1991.

[49] T. E. Moore, D. J. Chornay, M. R. Collier, F. A. Herrero, J. Johnson, M. A. Johnson, J. W. Weller, J. F. Laudadio, J. F. Lobell, K. W. Ogilvie, P. Rozmarynowski, S. A. Fuselier, A. G. Ghielmetti, E. Hertzberg, D. C. Hamilton, R. Lundgren, P. Wilson, P. Walpole, T. M. Stephen, B. L. Peko, B. van Zyl, P. Wurz, J. M. Quinn, and G. R. Wilson. The low energy neutral atom imager for IMAGE. *Space Sci. Rev.*, **91**:155, 2000.

[50] L. P. Levine and H. W. Berry. H_1^- production by hydrogen positive ion bombardment of a tungsten surface. *Phys. Rev.*, **118**:158, 1960.

[51] D. V. McCaughan, R. H. Sloane, and J. Geddes. Secondary ions from hydrogen ion bombardment of metal surfaces. *J. Appl. Phys.*, **51**:4426, 1980.

[52] E. G. Overbosch, B. Rasser, A. D. Tenner, and J. Los. The ionization of hyperthermal sodium atoms on W(110) as a function of temperature. *Surface Science*, **92**:310, 1980.

[53] J. N. M. van Wunnik, J. J. C. Geerlings, E. H. A. Granneman, and J. Los. The scattering of hydrogen from a cesiated tungsten surface. *Surf. Sci.*, **131**:17, 1983.

[54] P. J. M. van Bommel, J. J. C. Geerlings, J. N. M. van Wunnik, P. Massmann, E. H. A. Granneman, and J. Los. Formation of H^- by scattering H^+ on a cesiated polycrystalline tungsten surface. *J. Appl. Phys.*, **54**:5676, 1983.

[55] U. van Slooten, O. M. N. D. Teodoro, A. W. Kleyn, J. Los, D. Teillet-Billy, and J. P. Gauyacq. Negative ion formation in proton scattering from Ba/Ag(111). *Chem. Phys.*, **179**:227, 1994.

[56] U. van Slooten, W. R. Koppers, A. Bot, H. M. van Pinxteren, A. M. C. Moutinho, J. W. M. Frenken, and A. W. Kleyn. The adsorption of Ba on Ag(111). *J. Phys.: Condens. Matter*, **5**:5411, 1993.

[57] J. N. DeFazio. *Charge Exchange Collisions of Hydrogen Atoms and Ions with Laboratory Surfaces*. PhD thesis, University of Denver, March 2004.

[58] J. N. DeFazio and B. L. Peko. Origin of H^- in collisions of hydrogen atoms with an adsorbate-covered Cu(100) surface. *J. Vac. Sci. Technol. A*, **22**:2251, 2004.

[59] M. Wieser, P. Wurz, K. Brüning, and W. Heiland. Scattering of atoms and molecules off a magnesium oxide surface. *Nucl. Instrum. Meth. Phys. Res. B*, **192**:370, 2002.

[60] S. Jans, P. Wurz, R. Schletti, K. Brüning, K. Sekar, W. Heiland, J. Quinn, and R. E. Leuchtner. Scattering of atoms and molecules off a barium zirconate surface. *Nucl. Instrum. Meth. Phys. Res. B*, **173**:503, 2001.

[61] S. Jans, P.Wurz, R. Schletti, T. Fröhlich, E. Hertzberg, and S. Fuselier. Negative ion production by surface ionization at aluminum-nitride surfaces. *J. Appl. Phys.*, **87**:2587, 2000.

[62] B. van Zyl, N. G. Utterback, and R. C. Amme. Generation of a fast atomic hydrogen beam. *Rev. Sci. Instrum.*, **47**:814, 1976.

[63] R. W. Stinemin. A consistently well-behaved method of interpolation. *Creative Computing*, , 1980.

[64] D. W. Koopman. Measurement of charge-exchange cross sections for H^+, H_2^+, and He^+ ions. *Phys. Rev.*, **154**:79, 1967.

[65] J. H. Moore, C. C. Davis, and M. A. Coplan. *Building Scientific Apparatus*. Westview Press, Cambridge, 3rd edition, 2003.

[66] G. H. Dunn, R. Geballe, and D. Pretzer. Production of lyman alpha radiation in ion-atom collisions. *Phys. Rev.*, **128**:2200, 1962.

[67] D. R. Lide, editor. *CRC Handbook of Chemistry and Physics*. CRC Press, New York, 80th edition, 1999.

[68] B. L. Peko and T. M. Stephen. Absolute detection efficiencies of low energy H, H^-, H^+, H_2^+ and H_3^+ incident on a multichannel plate detector. *Nucl. Instrum. Meth. Phys. Res. B*, **171**:597, 2000.

[69] D. H. Crandall, J. A. Ray, and Carmen Cisneros. Channeltron efficiency for counting of H^+ and H^- at low energy. *Rev. Sci. Instrum.*, **46**:562, 1975.

[70] D.A. Dahl. *SIMION 3D Version 7.0 User's Manual, pub. # INEEL-95/0403*. Idaho National Engineering and Environmental Laboratory, Idaho Falls, ID 83415, 2000.

[71] J. R. Smith, R. Nemanich, E. Hertzberg, and A. Moore. Effect of hydrogen passivation on RMS roughness and electronic structure of diamond-like carbon films. MRS Fall Meeting Poster, 2006.

[72] K. G. Vandervoort, D. J. Butcher, C. T. Brittain, and B. B. Lewis. Scanning tunneling microscope images of graphite substrates used in graphite furnace atomic absorption spectrometry. *Appl. Spectros.*, **50**:928, 1996.

[73] K. B. K. Teo, M. Chhowalla, G. A. J. Amaratunga, W. I. Milne, G. Pirio, P. Legagneux, F. Wyczisk, D. Pribat, and D. G. Hasko. Field emission from dense, sparse, and patterned arrays of carbon nanofibers. *Appl. Phys. Lett.*, **80**:2011, 2002.

[74] L. Nilsson, O. Groening, C. Emmenegger, O. Kuettel, E. Schaller, L. Schlapbach, H. Kind, J-M. Bonard, and K. Kern. Scanning field emission from patterned carbon nanotube films. *Appl. Phys Lett.*, **76**:2071, 2000.

[75] D. J. Riley, M. Mann, D. A. MacLaren, P. C. Destoor, and W. Allison. Helium detection via field ionization from carbon nanotubes. *Nano Lett.*, **3**:1455, 2003.

[76] J. Wang, M. Zhu, R. A. Outlaw, X. Zhao, D. M. Manos, and B. C. Holloway. Synthesis of carbon nanosheets by inductively coupled radio-frequency plasma enhanced chemical vapor deposition. *Carbon*, **42**:2867, 2004.

[77] J. J. Wang, M. Y. Zhu, R. A. Outlaw, X. Zhao, D. M. Manos, B. C. Holloway, and V. P. Mammana. Free-standing subnanometer graphite sheets. *Appl. Phys. Lett.*, **85**:1265, 2004.

[78] D. R. Lide, editor. *CRC Handbook of Chemistry and Physics*. CRC Press, New York, 80th edition, 1999.

[79] E. C. Samano, W. E. Carr, M. Seidl, and B. S. Lee. An arc discharge hydrogen atom source. *Rev. Sci. Instrum.*, **64**:2746, 1993.